Modeling, Characterization, and Suppression of Temporary Overvoltages in Power Grids with High Share of Inverter-Based Resources

Final Project Report

T-66

Power Systems Engineering Research Center
Empowering Minds to Engineer
the Future Electric Energy System

Modeling, Characterization, and Suppression of Temporary Overvoltages in Power Grids with High Share of Inverter-Based Resources

Final Project Report

Project Team
Saeed Lotfifard, Project Leader
Washington State University

Sakis A. P. Meliopoulos
George J. Cokkinides
Georgia Institute of Technology

Graduate Students
Hassan Yazdani
Washington State University

Abdulaziz M. Qwbaiban
Georgia Institute of Technology

PSERC Publication 24-09

December 2024

For information about this project, contact:

Saeed Lotfifard
Washington State University
School of Electrical Engineering and Computer Science
Pullman, Washington 99164-2752
Phone: 509-335-0903
Email: s.lotfifard@wsu.edu

Power Systems Engineering Research Center

The Power Systems Engineering Research Center (PSERC) is a multi-university Center conducting research on challenges facing the electric power industry and educating the next generation of power engineers. More information about PSERC can be found at the Center's website: http://www.pserc.org.

For additional information, contact:

Power Systems Engineering Research Center
Arizona State University
527 Engineering Research Center
Tempe, Arizona 85287-5706
Phone: 480-965-1643
Fax: 480-727-2052

Notice Concerning Copyright Material

Acknowledgements

This is the final report for the Power Systems Engineering Research Center (PSERC) research project T-66 titled “Modeling, Characterization, and Suppression of Temporary Overvoltages in Power Grids with High Share of Inverter-Based Resources”. We also express our appreciation for the support provided by PSERC’s industrial members and the National Science Foundation’s Industry / University Cooperative Research Center program. We would like to recognize the following project advisors for their support to the project.

Aftab Alam (CAISO), Ran Xu (CAISO), Alan Engelmann (ComEd), Shikhar Pandey (ComEd), Mohit Singh (ComEd), Kurt Lafrance (CMS), Dennis R. Woycehoski (CMS), Ibukunoluwa Korede (dominionenergy), Zhongxia Zhang (dominionenergy), Gad Ilunga (dominionenergy), Evangelos Farantatos (EPRI), Aboutaleb Haddadi (EPRI), Alberto Del Rosso (EPRI), Deepak Ramasubramanian (EPRI), Kwok Cheung (GE), Deepak Konka (GE), Miaolei Shao (GE), Bishnu Sapkota (GE), Rijesh Akkanusery (GE), Panitarn Chongfuangprinya (Hitachi), Bo Yang (Hitachi), David Rieken (Hubbell), Mingguo Hong (ISO-NE), Xiaochuan Luo (ISO-NE), Yonghong Chen (MISO), Akshay Korad (MISO), Kun Zhu (MISO), David Till (NERC), Hongtao Ma (NERC), Fathalla Eldali (NRECA), Benjamin Kroposki (NREL), Kumaraguru Prabakar (NREL), Gab-Su Seo (NREL), Jianzhong Tong (PJM), Casey Cathey (SPP), Harvey Scribner (SPP), Bo Gong (SRP), Wisam Al Sudani (WAPA)

Executive Summary

This project focused on temporary overvoltage in IBR dominated power grids. The summary of the studies are as follows:

Part 1: Temporary overvoltage In IBRs Connected Power Systems

Part I of this project was focused on temporary overvoltages in IBRs connected power grids and the factors affecting the values of TOVs. The main results of the projects are as follows:

- The strength of the system is one of indicators that can be used to identify the possible vulnerable areas to TOVs. Accordingly, a variety of grid strength indicators were studied, and their advantages and limitations are discussed in this report.
- The impact of delays in the control loops and protection logics of IBRs on TOV were studies and time domain simulations were performed to demonstrate the impacts numerically.
- Impacts of different factors such as bandwidth of PLLs and changes in the grid strength were studies and the results are reported and discussed.
- Different factors affecting the TOV in IBR connected were studies using analytical methods such as state space analysis, Bode plots, and Generalized Nyquist Criterion.
- Time domain simulations were performed to demonstrate the impacts of the identified factors on the TOVs.
- The outcome of the studies can be used for tuning of the controllers and site location of IBRs to reduce the TOV impacts.

Part 2: Temporary overvoltage Analysis

- The Georgia Tech effort for this project has been focused on the following three parts of the study. (1) Proper representation of inverter-based resources in dynamic studies, (2) Conducting temporary overvoltage parametric studies, and (3) Studying the effects of temporary transients on the performance of the system.
- This report aims to understand the causes of overvoltage when Inverter-Based Resources (IBR) are suddenly connected or disconnected from the grid. It explores the extent to which overvoltage are expected to occur and examines the implications for existing legacy protection schemes using real-life test cases. The report begins by introducing the problem statement and providing examples of real-life incidents that occurred in Germany and Greece due to IBR triggered overvoltages and other transients. The report provides explanations why this work is crucial for determining the optimal design and positioning of new IBR projects to minimize overvoltages in the grid.
- In the second section, the report investigates the proper way to represent an IBR for the purpose of properly predicting overvoltages and other dynamic transients. It justifies the need for proper reorientation in moideling these systems and discusses previous work on modeling IBRs. It highlights the importance of establishing a model that is efficient in terms of hardware resources and time, providing real-time data for field operations. This is especially important when dealing with protection schemes that need to operate within a few cycles. A mathematical model for developing a high-fidelity representation of IBRs is presented.

- The third section introduces a real-life test system subject to the requirements outlined earlier. A detailed test case system is provided, covering all components from the generators and collector substation to the distribution network hosting the IBRs. The example test system includes several PV farms.
- In the fourth section, the report presents simulation results for selected events. It summarizes the percentage deviations of overvoltages for each of the three PV farms in the example test system and provides potential remedial actions to reduce overvoltage levels. The remedial actions help prevent physical damage to components and reduce the likelihood of false tripping in legacy protection schemes.
- Finally, the fifth section discusses the effects of temporary transients on system performance. A case study of an actual event on the Greek island of Rhodes is included. The sequence of events is modeled and simulated using a high-fidelity approach, incorporating mitigation and detection schemes, such as estimation-based protection, to avoid unnecessary generator tripping when IBR resources are suddenly generating transients that affect operation of IBRs and legacy power system components.

Project Publications:

[1] Hassan Yazdani, Saeed Lotfifard, "Temporary Overvoltages in IBR Connected Power grids" to be submitted, 2024.

Student Theses:

[1] Hassan Yazdani, Expected Ph.D thesis title "Grid Synchronization Stability Assessment and Enhancement of Inverter Based Resources", Washington State University.

Part I

Temporary Overvoltages in IBRs Connected Power Systems

Saeed Lotfifard
Hassan Yazdani, Graduate Student

Washington State University

For information about this project, contact

Saeed Lotfifard
Washington State University
School of Electrical Engineering and Computer Science
Pullman, Washington 99164-2752
Phone: 509-335-0903
Email: s.lotfifard@wsu.edu

Power Systems Engineering Research Center

The Power Systems Engineering Research Center (PSERC) is a multi-university Center conducting research on challenges facing the electric power industry and educating the next generation of power engineers. More information about PSERC can be found at the Center's website: http://www.pserc.org.

For additional information, contact:

Power Systems Engineering Research Center
Arizona State University
527 Engineering Research Center
Tempe, Arizona 85287-5706
Phone: 480-965-1643
Fax: 480-727-2052

Notice Concerning Copyright Material

Table of Contents

List of Figures

List of Tables

NOMENCLATURE

Acronym

CSCR	Composite short circuit ratio
ESCR	Equivalent short circuit ratio
GFL	Grid following
GNC	Generalized Nyquist criterion
GSIM	Grid strength impedance metric
HVdc	High-voltage direct current
IBR	Inverter-based resource
IILSCR	Short circuit ratio with interaction levels
LVRT	Low voltage ride through
MESCR	Multi-infeed effective short circuit ratio
MIIF	Multi-infeed interaction factor
MISCR	Multi-infeed short circuit ratio
POI	Point of interconnection
SCC	Short circuit capacity
SCR	Short circuit ratio
SDSCR	Site-dependent short circuit ratio
TOV	Temporary overvoltage
WSCR	Weighted short circuit ratio

Parameters

Z_g; Z_b	Grid's equivalent impedance and base impedance, respectively
I_d^{ref}; I_q^{ref}	Reference values of the IBR controller on each axis
I_G; I_R	Set of branch currents with conventional generators and IBRs, respectively
I_{max}; V_{max}	Maximum current and voltage of the IBR, respectively
I_N	Nominal current of the IBR
k_p^{PLL}; k_i^{PLL}	Proportional and integral coefficients of the PI PLL controller, respectively

$k_p;\ k_i$	Proportional and integral coefficients of the PI current controller, respectively
MV_{IBR}	Sum of nominal MW of existing IBRs
$P_{dc}; Q_{dc}$	Nominal active/reactive power of the HVdc plant
P_R	Rated MW of the IBR to be connected
Q_c	Shunt compensation of reactive power
$R_f; L_f; C_f$	Resistance, inductance, and capacitance of the IBR filter, respectively
$R_g;\ L_g$	Thevenin equivalent of the grid resistance and inductance
S_{SC}	SCC prior to IBR integration
U_i	Rated voltage at bus i
$V_G;\ V_R$	Set of bus voltages with conventional generators and IBRs, respectively
$Z_{BUS}; z_{i,j}$	Grid's impedance matrix and its ij-th element, respectively
$Z_{GG}; Z_{RR}$	Subsets of the grid's impedance matrix with conventional generators and IBRs, respectively
$Z_{GR};\ Z_{RG}$	Subsets of the grid's impedance matrix with both conventional generators and IBRs, respectively
Z_{IBR}	Equivalent impedance behavior of the IBR

Operators

$\mathbf{T}_{dq}$	dq transformation matrix
$J;\ J_R$	Jacobian and reduced Jacobian matrices, respectively
$\Phi;\ \Gamma;\ \Lambda$	Right eigenvectors, left eigenvectors, and eigenvalues of J_R, respectively

Variables

$P_N;\ Z_N$	Number of poles and zeros of the open loop transfer function inside the Nyquist contour
$i_i;\ i_c;\ i_o$	Input, capacitor, and output current of the IBR
N_N	Number of encirclements of the Nyquist plot around $-1 + j0$
P_{IBR}	Power injection of IBRs
$v_i;\ v_o;\ v_g$	IBR's input/output voltages, and grid's Thevenin equivalent voltage, respectively
IF_{ij}	Interaction factor of bus i and bus j
ΔV	Voltage deviation from its rated value
$\theta;\ \omega_s$	Angle and angular frequency of the grid

1. Temporary overvoltage In IBRs Connected Power Systems

1.1 TOV in power grids

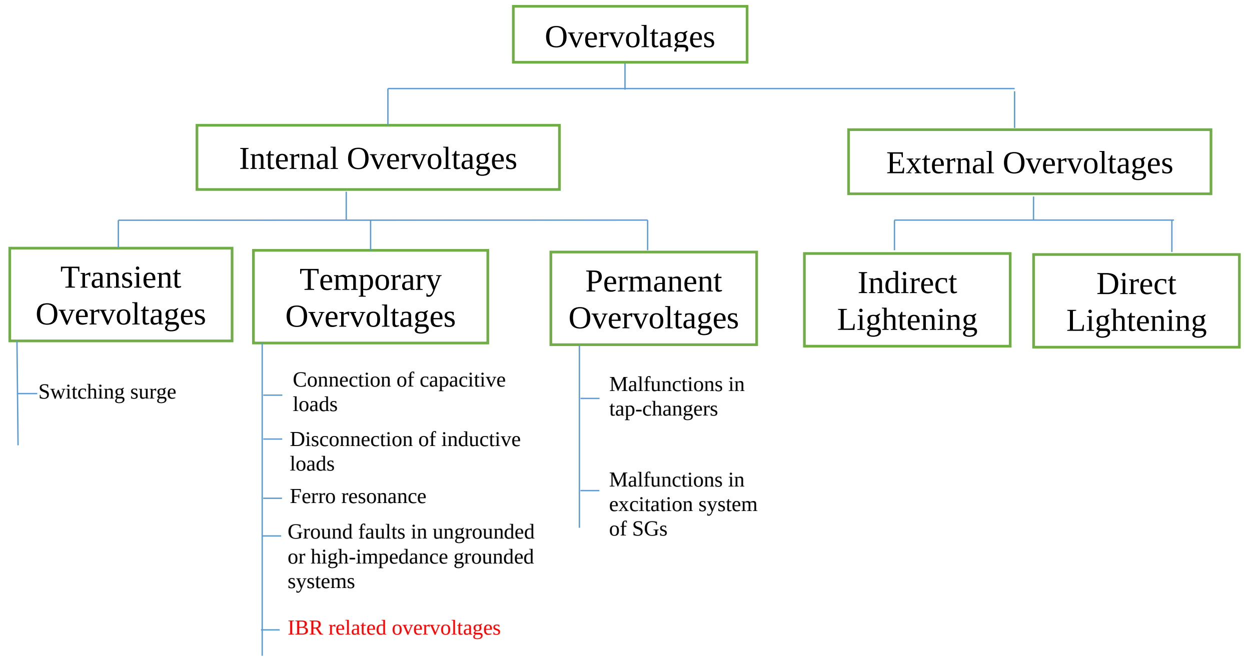

Figure 1-1 Overvoltages in power systems

In general, overvoltages in power systems fall into two main categories: 1) external overvoltages, 2) internal overvoltages. External overvoltages are mainly caused by lightning strikes, either directly or indirectly. Internal overvoltages, on the other hand, stem from numerous sources and fall into three main categories: 1) Transient overvoltages, 2) Temporary overvoltages (TOVs), and 3) Permanent overvoltages. For the case of transient overvoltages, reference [1] defines surges in low voltage grids that last about 50 micro seconds as a transient phenomenon, which are mostly caused by switching actions. On the other hand, TOVs last for much longer periods of time and can cause damage to the equipment. The sources for TOV can be connection of capacitor banks, disconnection of inductive loads, ferro resonance, and IBR related TOVs.

In this project, the focus is studying the TOV phenomenon which occurs immediately after clearing a fault in IBR dominated power grids. This occurs because of excessive reactive power which is built up during faults. For instance [2] evaluates the TOV during the recovery stage of LVRT, due to excessive provision of reactive current after a fault clearance. It is established that the TOV phenomenon is directly correlated with the grid's strength at the point of interconnection (POI). Hence, some efforts have been made to define strength related indices which will effectively highlight the associated risk of TOV.

In the subsequent sections of the report, grid strength indices will be studied, and their strengths and shortcomings will be discussed. Then factors that affect the TOV In IBRs connected systems will be investigated.

1.2 Grid strength indices

Strength in power grids is the ability to maintain stability in the face of abnormalities. A strong grid has adequate generation capacity and robust control mechanisms to maintain its voltage within the security limit. A strong grid can tolerate faults, detecting, isolating, and resolving them fast enough to prevent cascading failures and outages. On the other hand, a weak grid might go through voltage fluctuations, voltage collapse, and instability during major events, contingencies, and even demand fluctuations. Thus, a weak grid needs to be reinforced with adequate infrastructure and smart control techniques to enhance its response upon contingencies.
In an inverter-based resource (IBR) dominated power grid, the strength of the system should be studied in more detail. IBRs can positively (or negatively) affect the strength of the grid, or a weak grid can disrupt the robust operation of an IBR controller. For instance, when the voltage fluctuates in a weak grid, IBR controllers will not be able to inject sufficient reactive power or adjust the output quickly enough to follow grid's fluctuations, leading to deviations from the setpoint, which eventually leads to loss of synchronism. In addition, it is challenging to comply with grid codes to provide voltage/frequency support when the grid is weak. To provide a deeper understanding of the grid's strength, in the following section various strength indices have been reviewed in detail. Although in essence all the indices try to achieve the same goal, yet each use a different approach and tailored for specific studies.

1.2.1 Short circuit ratio (SCR)

A common criterion to measure the strength is short circuit ratio (SCR). This metric has traditionally been used to refer to the rigidness of the grid's voltage in an area. By calculating the SCR at the point of interconnection (POI) of IBRs, one can identify the weak buses of the system and place and operate the resources accordingly. To compute the SCR, first a three-phase short circuit analysis is conducted at the POI. Then, the ratio between the short-circuit capacity (SCC[1]) and the MW rating of the fault current source at the interconnection bus. In relation to this definition, SCR is as stated below:

$$\mathrm{SCR} = \frac{S_{SC}}{P_R} \tag{1.1}$$

In equation (1.1, S_{SC} is the SCC at the bus in the existing network before the connection of the new generation source, and P_R is the rated MW value of the new connected source [3]. In essence, SCR represents the distance to the voltage boundary limit. Consider equation (1.1. Imagine the goal is to calculate the SCR at bus i of the system. By further simplifying this equation:

$$\mathrm{SCR}_i = \frac{S_{SC_i}}{P_{R_i}} = \frac{1}{P_{R_i}} \times \frac{|V_i|^2}{|Z_i|} \tag{1.2}$$

[1] Short circuit capacity refers to the maximum current that can flow through a circuit when a short circuit occurs.

Where Z_i is the impedance of the grid at bus i. Based on (1.2, the further away the voltage is from the nominal value, the smaller the SCR, and vice versa.

Though SCR is intuitive, it neglects many aspects contributing to the system's strength. Proximity between plants can result in interactions and oscillations. SCR calculation using Equation (1.2 may yield an overly optimistic result in such scenarios. The high penetration of IBRs inevitably increases the equivalent AC grid impedance, weakening the AC grid and complicating interactions between IBRs and the AC grid. Consequently, the risk of oscillation issues becomes more pronounced in a weakened AC grid. In response to these challenges, many criteria have been introduced in the literature. Various approaches, such as GE's composite SCR (CSCR) and ERCOT's weighted SCR (WSCR) have been suggested to calculate the SCR in weak systems with high concentrations of IBRs. Yet, though many efforts have been made, as of now, there is no well-established standard that considers the IBR interactions in calculating the grid's strength. To get a more accurate estimation of the system strength index and to take interaction effects among producing resources into account, a more reliable indicator that can evaluate the potential risk with complex instabilities is required. In summary, some of the pros and cons of SCR as a measure of grid's strength are as follows:

Pros:

1. Easy and intuitive to obtain with an offline short circuit analysis of the grid.
2. It helps to locate and size various IBRs.

Cons:

1. Missing the dynamics of the system: The short circuit value is a static parameter and does not capture the dynamic behavior of the power system under varying loading conditions. Consequently, IBRs coming from various venders with different controllers have distinct dynamic behaviors during contingencies, which cannot be represented in the generic SCR metric.
2. Does not consider the operating point of the system.
3. Limited to AC Systems: SCR is primarily applicable to AC power systems and may not be directly applicable to DC systems or hybrid AC/DC grids. Therefore, its utility is limited in assessing the strength of emerging grid architectures incorporating DC technologies.

1.2.2 Composite SCR (CSCR)

This approach was first established by GE, with the purpose of evaluating strength while considering IBRs in close (electrical) proximity to the node under examination. CSCR computes the strength without accounting for the fault current contribution, assuming that all converters are connected to a single bus.

By generating a general medium bus voltage, this metric effectively estimates the equivalent system impedance represented by several IBRs.

$$\mathrm{CSCR} = \frac{S_{SC}}{MV_{IBR}} \tag{1.3}$$

In equation (1.3, S_{SC} is the fault level contribution excluding converters and MV_{IBR} is the sum of nominal power ratings of the connected converters. It is easy to identify that creating a median bus and assuming equal contribution from the resources is not accurate since the resources do not have identical behavior and impact on the strength. Although CSCR approximates the strength in presence of multiple IBRs, this approximation can be inaccurate since the interaction are completely ignored.

Pros and cons of this metric are similar to the conventional SCR. The only difference, as stated, is more accuracy in determining the sources connected to each area, which is captured by defining a median bus as an approximation. In addition, it can be challenging to define the median bus and results will vary with different choices.

1.2.3 Weighted SCR (WSCR)

As previously noted, the standard SCR ignores the interaction among IBRs, even though these units can interact and oscillate as a single unit. In this scenario, conventional SCR would provide a greatly optimistic estimate of the grid's strength.

In addition to CSCR, WSCR is another criterion that attempts to address this problem [4]. Unlike CSCR, WSCR analyzes critical points in the network with IBR linkages by evaluating numerous buses as defined below, where the strength of the complete system is approximated at once.

$$\mathrm{WSCR} = \frac{Weighted\ S_{SC}}{\sum_i^N P_{R,i}} = \frac{\sum_i^N S_{SC,i} \times P_{R,i}}{\left(\sum_i^N P_{R,i}\right)^2} \tag{1.4}$$

In (1.4, $S_{SC,i}$ is the SCC at bus i prior to the connection of the i-th IBR, and $P_{R,i}$ is the nominal power of the i-th IBR to be connected. i is the IBR index, and N is the total number of IBRs that fully interact with one another. WSCR has similar pros and cons which were discussed for SCR, with the following additions:

Pros:

1. Improved generator performance assessment: WSCR provides a more accurate and detailed assessment of a converter's impact on the power system during short circuits compared to the simple SCR. It considers the converter's capacity and impedance in a weighted manner.
2. More comprehensive than SCR: SCR only considers the IBR's apparent power without distinguishing between its active and reactive power contributions. WSCR, by using appropriate weighting factors, considers both real and reactive power components, providing a more comprehensive analysis.

Cons:

1. Although WSCR considers the interaction of IBRs, it does not consider the structure of the grid. In practice, the planners and operators are interested in knowing the strength not only at each IBR POI, but all the other buses as well, which WSCR is incapable of providing those.

1.2.4 Multi-infeed SCR (MISCR)

The CIGRE group [5] developed this metric in an attempt to apply the concept of grid strength to systems with several DC link interconnections. When several converters are connected to the same AC network, the MISCR at a specific bus act as an extension of the SCR and provides a standardized measurement of the strength of the system at that location, regardless of the number of converters connected.

$$\text{MISCR}_i = \frac{1}{\sum_{j=1}^{K} P_{dc_j} . z_{i,j}} \tag{1.5}$$

In equation (1.5, K represents the number of HVdc terminals, P_{dc_j} is the nominal power of the HVdc station j and $z_{i,j}$ is ij-th element in Z_{BUS} of the network. According to the definition of Z_{BUS}, the element in the i-th row and j-th column shows bus i's sensitivity to load fluctuations in bus j. A larger value for this term indicates that converter j has a greater impact on converter i.

Pros:

1. Considering the interaction between the sources.

Cons:

1. Ignoring the dynamics of the system.
2. Does not consider the operating point of the system.

1.2.5 Multi-infeed effective SCR (MESCR)

MESCR considers the interaction of DC rectifiers by defining a multi-infeed interaction factor (MIIF) as in (1.6,

$$\text{MIIF}_{ij} = \frac{U_i}{U_j} = \left|\frac{z_{ij}}{z_{jj}}\right| \tag{1.6}$$

where U_i and U_j represent the rated voltages of the i-th and j-th commutation buses. Z_{ij} represents the mutual impedance between the i-th and j-th buses, while z_{jj} is the impedance matrix denotes the self-impedance at the j-th bus. Once all the interaction factors are calculated, a matrix is formed where the diagonal elements, which represent the self-interaction, are equal to one. The rest of the elements vary between zero and one, where values closer to one indicate stronger interactions and those closer to zero indicate looser interactions. Based on (1.6, MIIF_{ij} and MIIF_{ji} are not necessarily equal and the resulting matrix can be non-symmetric.

To develop the concept of MESCR, first we discuss the derivation of Effective SCR (ESCR). The conventional definition of a single infeed inverter bus is as follows:

$$\text{ESCR}_i = \frac{S_{SC,i} - Q_{c,i}}{P_{dc,i}} \tag{1.7}$$

In (1.7, $S_{SC,i}$ is the three phase SCC of the AC system of the i-th DC commutation bus, $Q_{C,i}$ denotes the reactive power shunt compensation, and $P_{dc,i}$ and $Q_{dc,i}$ are the power of DC i and j, respectively. Then, by redefining the value of $P_{dc,i}$ to consider the effect of the interaction factors, MESCR is defined as follows:

$$\text{MESCR}_\text{i} = \frac{S_{SC,i} - Q_{c,i}}{P_{dc,i} + \sum_{j=1,j\neq i}^{k} MIIF_{ij} \times P_{dc,j}} \tag{1.8}$$

The pros and cons are similar to MISCR, the difference being that the rated conditions of the voltages contribute to the strength measure.

1.2.6 Inverter interaction level SCR (IILSCR)

IILSCR is a dynamic strength measure that takes into account the online real power contribution of the neighboring IBRs. To do so, a power flow tracing algorithm is required to decompose the share of each IBR injected to the bus i under study. This way, it is not necessary to determine the boundaries from which the IBRs within an area oscillate with one another. In equation (1.9 below:

$$\text{IILSCR}_i = \frac{S_{SC,i}}{P_{IBR,i} + \sum_{m=1,m\neq i}^{N} P_{IBR,(m-i)}} \tag{1.9}$$

$S_{SC,i}$ is the SCC of bus i, $P_{IBR,i}$ is the power rating of IBR installed on bus i, $P_{IBR,(m-i)}$ is power injection from neighboring IBRs. IILSCR relies heavily on power flow studies, which entails the following pros and cons:

Pros:

1. IILSCR leverages a comprehensive understanding of the flow of power within the system under various operating conditions, which results in measuring the interactions in a dynamic and accurate fashion.

Cons:

1. Complexity: Power flow analysis can be computationally demanding, particularly in large-scale power systems with several linked grids. Performing detailed analyses may require significant computational resources and time.
2. Modeling assumptions: power flow analysis relies on various modeling assumptions, such as the representation of system components, load characteristics, and generation dispatch, line limits, etc. Inaccurate or unrealistic assumptions can lead to unreliable results and misinterpretation of the system's strength.

1.2.7 Site dependent SCR (SDSCR)

The concept underlying SDSCR is to measure the impacts of several IBR interactions that are installed on distinct buses separately [6]. The physical distance between the IBRs is modelled by considering the impedance of the lines. To begin with, first the network model is partitioned into two parts: 1) buses including conventional generators, 2) buses including IBRs, as depicted in (1.10:

$$\begin{bmatrix} V_G \\ V_R \end{bmatrix} = \begin{bmatrix} Z_{GG} & Z_{GR} \\ Z_{RG} & Z_{RR} \end{bmatrix} \begin{bmatrix} I_G \\ I_R \end{bmatrix} \tag{1.10}$$

Where V_G and I_G are vectors of voltages and currents containing the synchronous generators, and V_R and I_R represent the buses containing the IBRs. Once these voltages are obtained, the SDSCR at each bus is calculated as follows:

$$\mathsf{SDSCR}_i = \frac{|V_{R,i}|^2}{\left(P_{R,i} + \sum_{j\in R, j\neq i}^{N} P_{R,j} w_{ij}\right)|Z_{RR,ii}|} \tag{1.11}$$

where each weight is calculated as follows:

$$w_{ij} = \frac{Z_{RR,ij}}{Z_{RR,ii}} (\frac{V_{R,i}}{V_{R,j}})^* \tag{1.12}$$

In equation (1.12, IBR interactions are taken into account considering the physical location of the neighboring IBRs. This means that to measure the strength at bus i, first the power injection $P_{R,i}$ from the respective IBR at that bus is considered. Next, this term is complemented with the contributions from the neighboring IBRs, $P_{R,j}$, each scaled by the voltages and impedances to the reflect not only the physical distance between the IBRs but also the distance to voltage boundary limit. In addition, all the term in the denominator is also scaled to the self-impedance of the bus i, $Z_{RR,ii}$. This way, if the IBRs on buses i and j are in close proximity, $Z_{RR,ii} \approx Z_{RR,ij}$, and the coupling impact of j on i will increase.

Comparing (1.11 with (1.2, it is evident that SDSCR is a more comprehensive version of the traditional SCR. When there is only one IBR on bus i and no IBR on neighboring buses, (1.11 will be the same as 1.2. this also indicates that both SCR and SDSCR measure the distance to the voltage boundary limit implicitly and explicitly, respectively. This also means that the same ranges that indicate a weak grid in SCR will roughly be applicable to SDSCR, indicating that a weak grid is essentially operating close to the volage stability boundary.

Pros:

1. the dynamics of voltages, power flow, as well as the grid structure are accounted for in measuring the strength of each node.

Cons:

1. computational burden of conducting the power flows, which are a function of the grid's operating conditions, making it challenging to calculate the worst case.

1.2.8 SCR with interaction factors (SCRIF)

To capture the effect of voltage deviations, the WSCR can be augmented with an interaction factor $\mathsf{IF}_{ij} = \frac{\Delta V_i}{\Delta V_j}$ as follows:

$$\mathsf{SCRIF}_i = \frac{S_{SC,i}}{P_{IBR,i} + \sum_{j=1, j\neq i}^{N} \mathsf{IF}_{ij} \times P_{IBR,j}} \tag{1.13}$$

Subscript j in this equation denotes all nearby buses that are electrically close to IBRs, or other buses. The coupling interaction of bus j on bus i is denoted by IF_{ij}. The voltage deviations at the

i-th and j-th bus, respectively, are represented by ΔV_i and ΔV_j. The nominal power rating and SCC contribution at bus i are denoted by $P_{IBR,i}$ and $S_{SC,i}$, respectively. Based on this derivation, when the voltage is stiffer, the interaction would be less, and the SCRIF would be a higher value.

1.2.9 Equivalent SCR (ESCR)

Equivalent circuit-based SCR (ESCR) was first proposed by CIGRE group in [7] to address the interactions of adjacent or electrically close wind power plants in measuring the system's strength. To begin with, assume a grid connected IBR. This system can be further simplified as depicted in Figure 1-2, where Z_g is the impedance in which R_g and L_g represent the impedance of the grid, and L_f, R_f, and C_f are the impedance of the IBR filter.

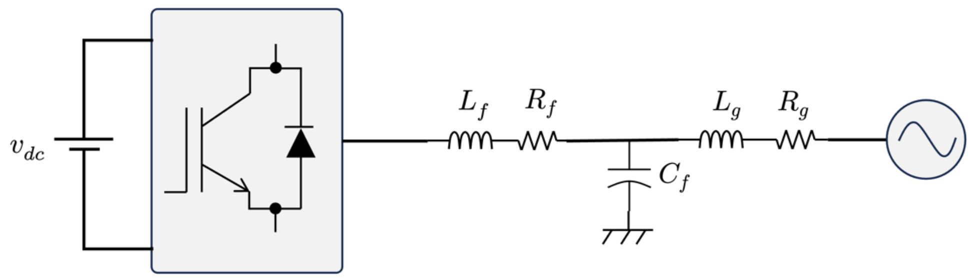

Figure 1-2 Schematic of a generic grid connected IBR

As discussed before, at the POI, the SCR of the system can be defined as in equation (1.14. Assuming that the base value of the system is P_{IBR}, this equation is further simplified in the p.u. system as follows:

$$S_{SC,PU} = \frac{v^2_{POI,PU}}{Z_{sys,PU}} = \frac{1}{Z_{sys,PU}} \quad (1.14)$$

Where $Z_{sys,PU}$ is the network impedance at the POI, and $v_{POI,PU}$ is the voltage, all in the per unit system. Substituting (1.14 in (1.16 gives:

$$\mathrm{ESCR}_{POI} = \frac{1}{Z_{sys,PU}} \quad (1.15)$$

Based on this simplification, SCR at POI is the inverse of the impedance observed at POI. This is consistent with the definition of SCR, as higher impedance indicates a weak grid and vice versa. To generalize this concept to multi-infeed systems, similar approaches as SCRIF has been utilized. Once again consider the interaction factor is defined as $\mathrm{IF}_{ij} = \frac{\Delta V_i}{\Delta V_j}$, where ΔV_i is a small voltage deviation on bus i resulting from a small voltage change on bus j. The closer IBR j is to IBR i, the bigger the interaction factor will be. For IBRs that are far away from each other, IF_{ij} will be negligible and if both i and j are on the same bus, this coefficient will be unity. To understand the coupling effect of multi-infeed power systems, when several IBRs are electrically close to each other, they share the SCC of the grid. Consequently, the SCR calculated from the perspective of the IBR will be higher than the actual value. With this generalization, the following equation is utilized to calculate the ESCR in multi-infeed systems:

$$\mathrm{ESCR}_i = \frac{S_{SC,i}}{P_{R,i} + \sum_j \mathrm{IF}_{ji} \times P_{R,j}} \tag{1.16}$$

Similar to the single infeed definition, ESCR can be further simplified in per unit system to be applicable to any network configuration as follows. Consider equation (1.17 which depicts the relationship between the node voltages and branch currents in a given network.

$$\begin{pmatrix} V_1 \\ V_2 \\ \vdots \\ V_n \end{pmatrix} = Z_{bus} \begin{pmatrix} I_1 \\ I_2 \\ \vdots \\ I_m \end{pmatrix} \tag{1.17}$$

Assuming a small change in the current at i-th node, the respective voltage changes on nodes i and j will be calculated as follows:

$$\begin{aligned} \Delta V_j &= z_{ji} \Delta I_i \\ \Delta V_i &= z_{ii} \Delta I_i \end{aligned} \tag{1.18}$$

Given this simplification, the impact factor is further simplified as:

$$IF_{ji} = \frac{\Delta V_j}{\Delta V_i} = \frac{z_{ji}}{z_{ii}} \tag{1.19}$$

Also, assuming the power of the IBR to be connected is the base value of the system:

$$SCR_i = \frac{S_{SC,i}}{P_{R,i}} = \frac{1}{Z_{ii}} \tag{1.20}$$

With this assumption, the formula in (1.15 is further simplified as:

$$\begin{aligned} ESCR_i = \frac{S_{SC,i}}{P_{R,i} + \sum_j IF_{ji} \times P_{R,j}} &= \frac{P_{R,i}/z_{ii}}{P_{R,i} + \sum_{j=1,m,j\neq i} \frac{z_{ji}}{z_{ii}} \times P_{R,j}} \\ &= \frac{1}{\sum_{j=1,m} z_{ji} \times P_{R,j,PU}} \end{aligned} \tag{1.21}$$

The metric provides an upper limit on the network impedance that the converter can function with. Note that this model does not account for how the output impedance is affected by the IBR controller system.

1.2.10 Grid strength impedance metric (GSIM)

In all of the previous methods, the interaction factors disregarded the control system of the IBR, assuming identical control behavior. In reality, IBRs coming from various vendors behave differently from one another. To address this issue, a method devised in [8] considers the MIMO impedance behavior of the IBR to estimate the strength of the entire system. By using this method, it is possible to model every component of the IBR in extensive detail, and as a result, this criterion assesses the strength across any given frequency spectrum. Consider the small-signal output admittance, represented in the synchronous reference frame of either the grid-forming or grid-following IBR as shown in equation (1.22:

$$Y_{vsc} = \frac{\Delta i}{\Delta v} = \begin{bmatrix} Y_{qq,c} & Y_{qd,c} \\ Y_{dq,c} & Y_{dd,c} \end{bmatrix} \tag{1.22}$$

Then, the base impedance of the grid is calculated as in equation (1.23:

$$Z_b = \begin{bmatrix} R_b + sL_b & \omega_b L_b \\ -\omega_b L_b & R_b + sL_b \end{bmatrix} \tag{1.23}$$

In which $R_b = Z_b \frac{R}{X}$ and $L_b = \frac{Z_b}{\omega_b}$, where Z_b is the base impedance of the system, ω_b is the fundamental frequency, and $\frac{R}{X}$ is the desired ratio of resistance to reactance of the network. This approach has the advantage that the impedances can be obtained by sweeping over the frequency spectrum in system identification techniques, negating the need for extensive modeling. In the following, $Y_{sys}(s)$ is the admittance of the system under study, and Z_b is the base value for the impedance.

$$Y_{sys}(s) = \begin{bmatrix} Y_{qq}(s) & Y_{qd}(s) \\ Y_{dq}(s) & Y_{dd}(s) \end{bmatrix} \tag{1.24}$$

$$Z_b = \begin{bmatrix} Z_{qq}(s) & Z_{qd}(s) \\ Z_{dq}(s) & Z_{dd}(s) \end{bmatrix} \tag{1.25}$$

Each of the 2×2 matrices then produce two eigenloci denoted q and d. by elementwise multiplication of the eigenvalues, the GSIM metric is developed as follows:

$$\begin{bmatrix} \mathrm{GSIM}_d(s) \\ \mathrm{GSIM}_q(s) \end{bmatrix} = \lambda(Y_{sys}(s)) \odot \lambda(Z_b(s)) \tag{1.26}$$

Combining the two components together to take into account the interaction between the two axes yields the following result:

$$\mathrm{GSIM}(s) = \sqrt{\frac{\mathrm{GSIM}_d^2(s) + \mathrm{GSIM}_q^2(s)}{2}} \tag{1.27}$$

This measure effectively estimates the strength in a wide range of frequency for which the linearized impedance is valid. The catch is that modelling each IBR controller based on various control techniques can a challenging task. With just a few numbers of IBRs, the model can easily become intractable.

1.2.11 QV modal analysis

This method relies on the Jacobian matrix of the system to develop a strength measure. The Jacobian has the following format [9]:

$$\begin{bmatrix} \Delta P \\ \Delta Q \end{bmatrix} = \begin{bmatrix} J_{11} & J_{12} \\ J_{21} & J_{22} \end{bmatrix} \begin{bmatrix} \Delta \theta \\ \Delta V \end{bmatrix} \tag{1.28}$$

In this equation, ΔP and ΔQ represent active power and reactive power mismatches, respectively, and ΔV represents unknown voltage magnitude, and $\Delta \theta$ indicates angle correction. In power grids, ΔP and ΔQ are weakly coupled in most operating scenarios. Assuming $\Delta P = 0$, the above equation can be further simplified as follows:

$$\Delta Q = J_R \Delta V \tag{1.29}$$

$$\Delta V = J_R^{-1} \Delta Q \tag{1.30}$$

Where J_R is the reduced Jacobian:

$$J_R = [J_{22} - J_{21} J_{11}^{-1} J_{12}] \tag{1.31}$$

The eigenvector of the reduced Jacobian can reveal the weak nodes in the power system under study, while the size of the Jacobian matrix’s eigenvalues can predict the static voltage boundary margin of a particular bus. Using eigenvalues and eigenvectors, the reduced Jacobian can be broken down as follows:

$$J_R = \Phi \Lambda^{-1} \Gamma \tag{1.32}$$

Where Φ is the right eigenvector of J_R, Γ is the diagonal eigenvalue matrix, and Λ is the left eigenvalue matrix of J_R. By inputting this decomposition into the reduced QV equation:

$$\Delta V = \sum_{i=1}^{n} \frac{\Phi_i \Gamma_i}{\lambda_i} \Delta Q \tag{1.33}$$

Equation (1.33 contains the information regarding the weakest nodes in the grid. In this equation, λ_i is the eigenvalue of J_R, Φ_i is its right eigenvalue, and Γ_i is the mode. This is a dynamic model that can track the system strength based on various conditions. Although a simplified average model of IBR is required to calculate the power flow results, hence the controller dynamics are ignored.

1.2.12 Generalized SCR (gSCR)

The SCR metric was developed to estimate the strength of single-infeed integration of IBRs. Next, various metrics were discussed that tried to deal with the multi-infeed systems. Among these techniques, those which develop a strength measure using linearized power flow equations with reduced Jacobian matrix fall in a category called generalized SCR (gSCR). This concept is close to that off SDSCR, where it begins by further simplifying the SCR definition as shown in (1.2 to demonstrate how the definition of SCR is implicitly tied to the distance to the static voltage boundary limits, and then trying to extend that to a network with multiple IBRs. For instance, the gSCR metric developed in [10] utilizes eigenvalue decomposition from a voltage stability perspective, through the linearization of AC power flow equations. The minimal eigenvalue of the system's extended admittance matrix is referred to as gSCR. For instance, in a multi-infeed DC transmission system:

$$\mathrm{gSCR} = \min \lambda(J_B) \tag{1.34}$$

In which J_B is the extended admittance matrix of the multi-infeed network, defined as:

$$J_B = \begin{pmatrix} P_1 & \cdots & 0 \\ \vdots & \ddots & \vdots \\ 0 & \cdots & P_n \end{pmatrix}^{-1} \begin{pmatrix} B_{11} & \cdots & B_{1n} \\ \vdots & \ddots & \vdots \\ B_{n1} & \cdots & B_{nn} \end{pmatrix} \tag{1.35}$$

In this equation, P_i is the admittance matrix of the i-th DC interconnection, and B_{ii} and B_{ij} are the imaginary parts of the elements in the AC system equivalent admittance matrix at the DC infeed buses. Based on the case studies demonstrated in [10], when the gSCR is less than two at an DC infeed bus, it indicates that this interconnection is weak and is susceptible to voltage oscillations. But for gSCR values greater than 3, the AC system is robust enough to host the HVdc system, ensuring that the limit operating condition of the HVdc system is guaranteed in normal operating conditions.

1.2.13 Summary and comparison of strength indices

In this report, methods that can be utilized to measure the strength of the power grid were briefly explained. It starts with the SCR, which is well established for analyzing grid’s strength. SCR does not consider the network’s structure, coupling among the resources, which causes interactions and oscillations, and dynamics of the IBR controllers. To resolve these shortcomings, various approaches were reviewed which tried to incorporate the grid’s structure, by assigning weights to adjacent contributing IBRs, and the voltage boundary limits. SCR only assumes the units connected to the node under study, CSCR assumes a single bus where all IBRs are connected to, and contribute equally, WSCR is similar to CSCR, but assumes multiple points in the system, and SCRIF captures voltage deviations among the bus under study and the adjacent contributing buses. Most of these methods ignore the dynamics of IBRs, and only consider the strength in fundamental frequency. Another shortcoming of these methods is that the fault behavior of IBRs is not identical to the behavior of conventional generators, based on which most of these methods are developed. To address these challenges, an impedance-based category of criteria has been introduced that do not necessarily consider quasi-steady state operation of IBRs, such as GSIM. Another advantage of this technique is that the two different control techniques of IBRs, namely grid following and grid forming, could be applied to assess which of them would increase the system’s strength at each POI.

1.3 Factors affecting the temporary overvoltages in IBRs connected systems

In this project we investigated different factors that may affect the temporary overvoltages. The case study results showed that the reduction in the strength of the system that may lead to grid synchronization Instability and delays in the protection logics of IBRs (i.e. fault ride through logic) are influential factors. In the subsequent sections the impacts of above factors are studied analytically based on the state space and impedance-based methods and numerically based on time domain simulations.

1.4 State space model

Assume there is a grid-tied inverter as depicted in Figure 1-3. The inverter is interfaced with the AC grid through an LC filter. A phase locked loop (PLL) is implemented to measure the voltage angle and the frequency of the grid.

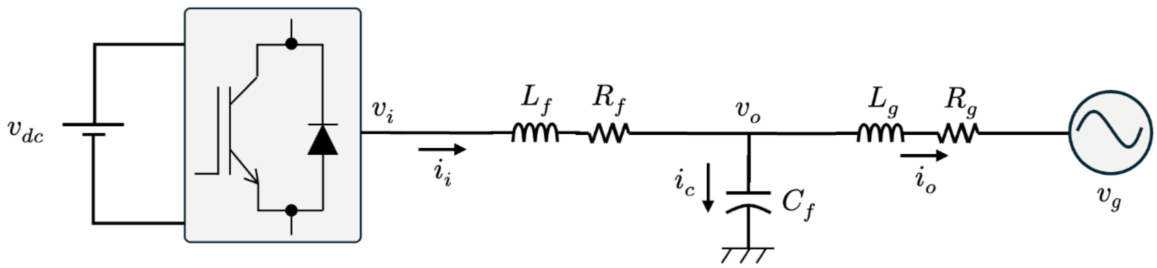

Figure 1-3 Grid-tied IBR system

To begin with, by writing the KVL at the filter, the following equation is obtained:

$$\begin{bmatrix} v_{ia} \\ v_{ib} \\ v_{ic} \end{bmatrix} - \begin{bmatrix} v_{oa} \\ v_{ob} \\ v_{oc} \end{bmatrix} = R_f \begin{bmatrix} i_{ia} \\ i_{ib} \\ i_{ic} \end{bmatrix} + L_f \frac{d}{dt} \begin{bmatrix} i_{ia} \\ i_{ib} \\ i_{ic} \end{bmatrix} \tag{1.36}$$

Using the Park transform in (1.37, any 3-phase signal can be transformed to dc signals in dq frame, where it is much more convenient to work with dc signals.

$$\begin{bmatrix} x_d \\ x_q \\ x_0 \end{bmatrix} = \sqrt{\frac{2}{3}} \underbrace{\begin{bmatrix} cos\ (\theta) & cos\ (\theta - \frac{2\pi}{3}) & cos\ (\theta + \frac{2\pi}{3}) \\ -sin\ (\theta) & -sin\ (\theta - \frac{2\pi}{3}) & -sin\ (\theta + \frac{2\pi}{3}) \\ \frac{1}{\sqrt{2}} & \frac{1}{\sqrt{2}} & \frac{1}{\sqrt{2}} \end{bmatrix}}_{\mathbf{T}_{dq}} \begin{bmatrix} x_a \\ x_b \\ x_c \end{bmatrix} \tag{1.37}$$

In this equation, x_{abc} and x_{dq0} are arbitrary signals in abc and dq frames, respectively, and $\theta = \omega_s t$, where ω_s represents the synchronous speed at which the dq frame rotates. By multiplying the inverse of $\mathbf{T}_{dq}$ to the both sides of (1.36 and further simplifying the results, equations (1.38 and (1.39 called the two-axis equation of the IBR are obtained.

$$\frac{di_{id}}{dt} = \frac{1}{L_f}(v_{id} - R_f i_{id} + \omega_s L_f i_{iq} - v_{od}) \tag{1.38}$$

$$\frac{di_{iq}}{dt} = \frac{1}{L_f}(v_{iq} - R_f i_{iq} - \omega_s L_f i_{id} - v_{oq}) \tag{1.39}$$

The current controller is depicted in Figure 1-5. The objective of this controller is to generate proper voltage modulation signals for which the current references are tracked. In addition, assuming the PLL effect, the signals in the controller frame deviate from the signals in the grid frame as depicted in Figure 1-4, and to differentiate between the two, those in the control frame are denoted with the superscript c.

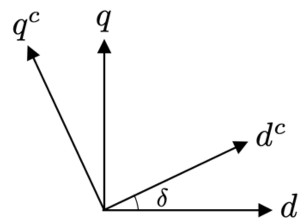

Figure 1-4 angle deviation between the grid and the controller frames

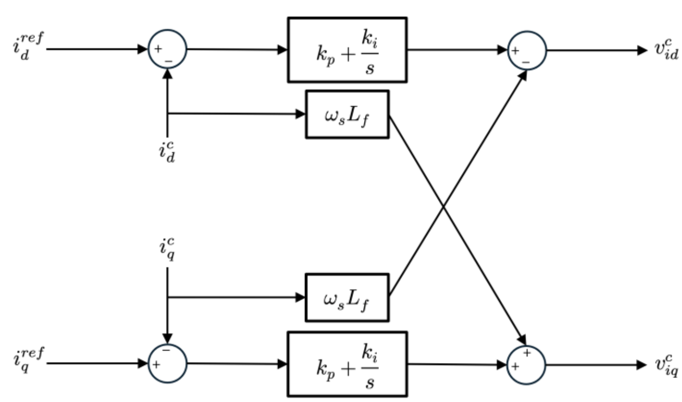

Figure 1-5 Two-axis current controller

By writing the equation of each channel separately, the output voltages are obtained as follows:

$$v_{id}^c = -\omega_s L_f i_{iq}^c + k_p\left(i_{id}^{ref} - i_{id}^c\right) + k_i \int \left(i_{id}^{ref} - i_{id}^c\right)dt \tag{1.40}$$

$$v_{iq}^c = \omega_s L_f i_{id}^c + k_p\left(i_{iq}^{ref} - i_{iq}^c\right) + k_i \int \left(i_{iq}^{ref} - i_{iq}^c\right)dt \tag{1.41}$$

Next, the PLL is implemented for the IBR to track the angle and the frequency of the grid. The controller block diagram of the PLL is depicted in Figure 1-6.

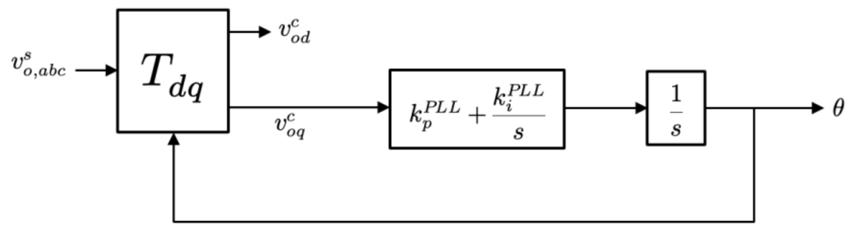

Figure 1-6 Synchronous reference frame PLL

which gives the following equation:

$$\Delta\theta = (k_p^{PLL}\Delta v_{oq}^c + k_i^{PLL}\int \Delta v_{oq}^c dt)\frac{1}{s} \tag{1.42}$$

The addition of PLL creates nonlinearity in the state equations. To develop the state space model, the linearized dynamics of the PLL are considered as follows.

$$\Delta\psi = \int \Delta v_{oq}^c dt \tag{1.43}$$

$$\frac{d}{dt}\begin{bmatrix}\Delta\theta \\ \Delta\psi\end{bmatrix} = \begin{bmatrix}0 & k_i^{PLL} \\ 0 & 0\end{bmatrix}\begin{bmatrix}\Delta\theta \\ \Delta\psi\end{bmatrix} + \begin{bmatrix}0 & k_p^{PLL} \\ 0 & 1\end{bmatrix}\begin{bmatrix}\Delta v_{od}^c \\ \Delta v_{oq}^c\end{bmatrix} \tag{1.44}$$

In equations (1.40, (1.41, and (1.44, signals are in the control frame. In the final state equations, all the signals should be on the same frame. In steady state, the angle δ is zero, which means that the two frames are aligned and the PLL is perfectly tracking the grid's angle and frequency. Once a small disturbance occurs, this propagates to the IBR through the PLL dynamics, for which there will be an angular difference for the grid's synchronous frame (denoted by s) and the IBR's control frame (denoted by c). The capital letters represent steady state values of the voltages and currents:

$$\begin{bmatrix}V_{id}^c \\ V_{iq}^c\end{bmatrix} = \begin{bmatrix}V_{id}^s \\ V_{iq}^s\end{bmatrix};\ \begin{bmatrix}V_{od}^c \\ V_{oq}^s\end{bmatrix} = \begin{bmatrix}V_{od}^s \\ V_{oq}^s\end{bmatrix};\ \begin{bmatrix}I_{id}^c \\ I_{iq}^c\end{bmatrix} = \begin{bmatrix}I_{id}^s \\ I_{iq}^s\end{bmatrix};\ \begin{bmatrix}I_{od}^c \\ I_{oq}^c\end{bmatrix} = \begin{bmatrix}I_{od}^s \\ I_{oq}^s\end{bmatrix} \tag{1.45}$$

Since these steady state values are equal, the superscripts are dropped, and capital letters indicate steady state values. Assuming a small disturbance in the angular frequency $\Delta\theta \approx 0$:

$$T_{\Delta\theta} = \begin{bmatrix}\cos(\Delta\theta) & \sin(\Delta\theta) \\ -\sin(\Delta\theta) & \cos(\Delta\theta)\end{bmatrix} = \begin{bmatrix}1 & \Delta\theta \\ -\Delta\theta & 1\end{bmatrix} \tag{1.46}$$

Using this transformation, the relationship between the signals in the system frame and the control frame is linearized as follows. For the output voltage:

$$\begin{bmatrix} V_{od} + \Delta v_{od}^c \\ V_{oq} + \Delta v_{oq}^c \end{bmatrix} = \begin{bmatrix} 1 & \theta \\ -\theta & 1 \end{bmatrix} \begin{bmatrix} V_{od} + \Delta v_{od}^s \\ V_{oq} + \Delta v_{oq}^s \end{bmatrix} \tag{1.47}$$

$$\begin{bmatrix} \Delta v_{od}^c \\ \Delta v_{oq}^c \end{bmatrix} \approx \begin{bmatrix} \Delta v_{od}^s + V_{oq}\Delta\theta \\ \Delta v_{oq}^s - V_{od}\Delta\theta \end{bmatrix}$$

And for the input voltage and current:

$$\begin{bmatrix} I_{id} + \Delta i_{id}^c \\ I_{iq} + \Delta i_{iq}^c \end{bmatrix} = \begin{bmatrix} 1 & \theta \\ -\theta & 1 \end{bmatrix} \begin{bmatrix} I_{id} + \Delta i_{id}^s \\ I_{iq} + \Delta i_{iq}^s \end{bmatrix} \tag{1.48}$$

$$\begin{bmatrix} V_{id} + \Delta v_{id}^s \\ V_{iq} + \Delta v_{iq}^s \end{bmatrix} = \begin{bmatrix} 1 & \theta \\ -\theta & 1 \end{bmatrix}^{-1} \begin{bmatrix} V_{id} + \Delta v_{od}^c \\ V_{iq} + \Delta v_{oq}^c \end{bmatrix} \tag{1.49}$$

Using the transformation in (1.47, the state equations of the PLL in (1.44 are transformed to the system's frame as follows:

$$\frac{d}{dt}\begin{bmatrix} \Delta\theta \\ \Delta\psi \end{bmatrix} = \begin{bmatrix} -k_p^{PLL} V_{od}^s & k_i^{PLL} \\ -V_{od}^s & 0 \end{bmatrix} \begin{bmatrix} \Delta\theta \\ \Delta\psi \end{bmatrix} + \begin{bmatrix} 0 & k_p^{PLL} \\ 0 & 1 \end{bmatrix} \begin{bmatrix} \Delta v_{od}^s \\ \Delta v_{oq}^s \end{bmatrix} \tag{1.50}$$

Next, the two axis controller equations are unified to the same frame. First, the following states are introduced to consider the integral action in the PI controller:

$$\Delta\gamma_d = \int \left(\Delta i_d^{ref} - \Delta i_d^c\right) dt \tag{1.51}$$

$$\Delta\dot{\gamma}_d = \Delta i_d^{ref} - \left(\Delta i_d^s + \Delta\theta I_q^s\right) \tag{1.52}$$

$$\Delta\gamma_q = \int \left(\Delta i_q^{ref} - \Delta i_q^c\right) dt \tag{1.53}$$

$$\Delta\dot{\gamma}_q = \Delta i_q^{ref} - \left(\Delta i_q^s - \Delta\theta I_d^s\right) \tag{1.54}$$

By inputting these linearized values into (1.40 and (1.41, the following equations are obtained:

$$\Delta v_{id}^s + V_{iq}\Delta\theta = -\omega_s L_f\left(\Delta i_{iq}^s - I_{id}\Delta\theta\right) + k_p\left(\Delta i_{id}^{ref} - \left(\Delta i_{id}^s + I_{iq}\Delta\theta\right)\right) + k_i\Delta\gamma_d \tag{1.55}$$

$$\Delta v_{iq}^s - V_{id}\Delta\theta = \omega_s L_f\left(\Delta i_{id}^s + I_{iq}\Delta\theta\right) + k_p\left(\Delta i_{iq}^{ref} - \left(\Delta i_{iq}^s - I_{id}\Delta\theta\right)\right) + k_i\Delta\gamma_q \tag{1.56}$$

By further simplifying these equations:

$$\Delta v_{id}^s = \left(-V_{iq} + \omega_s L_f I_{id} - k_p I_{iq}\right)\Delta\theta + k_p\Delta i_{id}^{ref} - k_p\Delta i_{id}^s - \omega_s L_f \Delta i_{iq}^s + k_i\Delta\gamma_d \tag{1.57}$$

$$\Delta v_{iq}^{s} = \left(V_{id} + \omega_s L_f I_{iq} - k_p I_{id}\right)\Delta\theta + k_p \Delta i_{iq}^{ref} - k_p \Delta i_{iq}^{s} + \omega_s L_f \Delta i_{id}^{s} + k_i \Delta\gamma_q \tag{1.58}$$

By inputting these voltage signals into (1.38 and (1.39:

$$\frac{d\Delta i_{id}^{s}}{dt} = \frac{1}{L_f}\Big(\big(-V_{iq}^{s} + \omega_s L_f I_{id}^{s} - k_p I_{iq}^{s}\big)\Delta\theta + k_p \Delta i_{id}^{ref} - \big(k_p + R_f\big)\Delta i_{id}^{s} + k_i \Delta\gamma_d - \Delta v_{od}^{s}\Big) \tag{1.59}$$

$$\frac{d\Delta i_{iq}^{s}}{dt} = \frac{1}{L_f}\Big(\big(V_{id}^{s} + \omega_s L_f I_{iq}^{s} + k_p I_{id}^{s}\big)\Delta\theta + k_p \Delta i_{iq}^{ref} - \big(k_p + R_f\big)\Delta i_{iq}^{s} + k_i \Delta\gamma_q - \Delta v_{oq}^{s}\Big) \tag{1.60}$$

Next, the dynamics of the filter's capacitor are introduced by writing a KCL at POI as follows:

$$\boldsymbol{T}_{dq}^{-1} \times \frac{d}{dt}\begin{bmatrix}\Delta v_{oa}^{s}\\ \Delta v_{ob}^{s}\\ \Delta v_{oc}^{s}\end{bmatrix} = \frac{1}{C_f} \times \boldsymbol{T}_{dq}^{-1} \times \left(\begin{bmatrix}\Delta i_{ia}^{s}\\ \Delta i_{ib}^{s}\\ \Delta i_{ic}^{s}\end{bmatrix} - \begin{bmatrix}\Delta i_{oa}^{s}\\ \Delta i_{ob}^{s}\\ \Delta i_{oc}^{s}\end{bmatrix}\right) \tag{1.61}$$

By transforming this into the dq frame, the following dynamics are obtained:

$$\frac{d\Delta v_{od}^{s}}{dt} = \frac{1}{C_f}\left(\Delta i_{id}^{s} + \omega_s C_f \Delta v_{oq}^{s} - \Delta i_{od}^{s}\right) \tag{1.62}$$

$$\frac{d\Delta v_{oq}^{s}}{dt} = \frac{1}{C_f}\left(\Delta i_{iq}^{s} - \omega_s C_f \Delta v_{od}^{s} - \Delta i_{oq}^{s}\right) \tag{1.63}$$

Finally, the dynamics of the grid are added as follows:

$$\begin{bmatrix}\Delta v_{oa}\\ \Delta v_{ob}\\ \Delta v_{oc}\end{bmatrix} - \begin{bmatrix}\Delta v_{ga}\\ \Delta v_{gb}\\ \Delta v_{gc}\end{bmatrix} = R_g \begin{bmatrix}\Delta i_{oa}\\ \Delta i_{ob}\\ \Delta i_{oc}\end{bmatrix} + L_g \frac{d}{dt}\begin{bmatrix}\Delta i_{oa}\\ \Delta i_{ob}\\ \Delta i_{oc}\end{bmatrix} \tag{1.64}$$

Transforming (1.64 to the dq frame, the two axis grid dynamics equations are obtained as in (1.65 and (1.66:

$$\frac{d\Delta i_{gd}^{s}}{dt} = \frac{1}{L_g}\left(\Delta v_{od}^{s} - R_g \Delta i_{gd}^{s} - \omega_s L_g \Delta i_{gq}^{s} - \Delta v_{gd}^{s}\right) \tag{1.65}$$

$$\frac{d\Delta i_{gq}^{s}}{dt} = \frac{1}{L_g}\left(\Delta v_{oq}^{s} - R_g \Delta i_{gq}^{s} - \omega_s L_g \Delta i_{gd}^{s} - \Delta v_{gq}^{s}\right) \tag{1.66}$$

In the system developed above, the state vector X, the input vector u, and the output vector y are depicted in (1.67.

$$X = [\Delta i_{id}^{s}, \Delta i_{iq}^{s}, \Delta i_{od}^{s}, \Delta i_{oq}^{s}, \Delta v_{od}^{s}, \Delta v_{oq}^{s}, \Delta\theta, \Delta\psi, \Delta\gamma_d, \Delta\gamma_q]$$
$$u = [\Delta i_{id}^{ref}, \Delta i_{iq}^{ref}, \Delta v_{gd}^{s}, \Delta v_{gq}^{s}] \tag{1.67}$$
$$y = [\Delta i_{id}^{s}, \Delta i_{iq}^{s}, \Delta v_{od}^{s}, \Delta v_{oq}^{s}]$$

Where $\dot{X} = AX + Bu$ and $y = CX$, and matrices A, B, and C are as follows:

$$A = \begin{bmatrix} -\frac{k_p+R_f}{L_f} & 0 & 0 & 0 & -1 & 0 & \frac{-V_{iq}+\omega_s L_f I_{id}-k_p I_{iq}}{L_f} & 0 & \frac{k_i}{L_f} & 0 \\ 0 & -\frac{k_p+R_f}{L_f} & 0 & 0 & 0 & -1 & \frac{V_{id}+\omega_s L_f I_{iq}-k_p I_{id}}{L_f} & 0 & 0 & \frac{k_i}{L_f} \\ 0 & 0 & -\frac{R_g}{L_g} & \omega_s & \frac{1}{L_g} & 0 & 0 & 0 & 0 & 0 \\ 0 & 0 & -\omega_s & -\frac{R_g}{L_g} & 0 & \frac{1}{L_g} & 0 & 0 & 0 & 0 \\ \frac{1}{C_f} & 0 & -\frac{1}{C_f} & 0 & 0 & \omega_s & 0 & 0 & 0 & 0 \\ 0 & \frac{1}{C_f} & 0 & -\frac{1}{C_f} & -\omega_s & 0 & 0 & 0 & 0 & 0 \\ 0 & 0 & 0 & 0 & 0 & k_p^{PLL} & -k_p^{PLL} V_{od} & k_i^{PLL} & 0 & 0 \\ 0 & 0 & 0 & 0 & 0 & 1 & -V_{od} & 0 & 0 & 0 \\ -1 & 0 & 0 & 0 & 0 & 0 & -I_{iq} & 0 & 0 & 0 \\ 0 & -1 & 0 & 0 & 0 & 0 & I_{id} & 0 & 0 & 0 \end{bmatrix} \tag{1.68}$$

$$B = \begin{bmatrix} \frac{k_p}{L_f} & 0 & 0 & 0 \\ 0 & \frac{k_p}{L_f} & 0 & 0 \\ 0 & 0 & -\frac{1}{L_g} & 0 \\ 0 & 0 & 0 & -\frac{1}{L_g} \\ 0 & 0 & 0 & 0 \\ 0 & 0 & 0 & 0 \\ 0 & 0 & 0 & 0 \\ 0 & 0 & 0 & 0 \\ 1 & 0 & 0 & 0 \\ 0 & 1 & 0 & 0 \end{bmatrix} \tag{1.69}$$

$$C = \begin{bmatrix} 1 & 0 & 0 & 0 & 0 & 0 & 0 & 0 \\ 0 & 1 & 0 & 0 & 0 & 0 & 0 & 0 \\ 0 & 0 & 1 & 0 & 0 & 0 & 0 & 0 \\ 0 & 0 & 0 & 1 & 0 & 0 & 0 & 0 \end{bmatrix} \tag{1.70}$$

1.5 Impedance model

The Nyquist theory is one of the fundamental tools in studying the stability of linear feedback control systems. In involves plotting the loci of the open loop transfer function of the system in complex plane for frequencies in $(-\infty, \infty)$ range. This plot essentially maps the complex values of the open loop gain in a range of frequencies. To plot the Nyquist graph, a sufficiently large contour is considered that contains the closed right half plane and as s travels on this contour, in clockwise direction, the open loop characteristic loci encircles the $-1 + j0$ point N times, where

$$N_N = Z_N - P_N \tag{1.71}$$

In equation (1.71, Z_N and P_N are zeros and poles of the open loop characteristic function inside the abovementioned contour. The number of unstable closed-loop poles Z_N is equal to the number of unstable open-loop poles P_N plus the number of encirclements of the $-1 + j0$ point. For the system to be stable, Z_N should be zero, resulting in $N_N = -P_N$. This means that for stability, the Nyquist plot should not encircle the $-1 + j0$ point.

This concept of Nyquist stability perfectly predicts the behavior of a single input single output (SISO) systems. In addition, efforts have been made to extend this concept for stability analysis of multi input multi output (MIMO) systems, a proof of which is offered in [11]. In MIMO systems, each output may be affected by several inputs and this coupling interactions are modelled through a matrix. Once again, the open loop characteristic loci of the system is obtained and since this forms a matrix, the loci of eigenvalues of this characteristic are plotted and the focus is on how each eigenvalue loci behaves in the s plane. Essentially, these eigenvalues comprise the modes of the system and analyzing their behavior provides insight into the response of the system's modes.

To apply the GNC to the inverter system, the concept of impedance-based stability analysis is used. Consider that the grid is modelled as an ideal voltage source $V_g(s)$ series with an impedance $Z_g(s)$. As explained in the previous section, the IBR is also modelled as a current source, paralleled with its impedance $Z_{IBR}(s)$. In addition, it is assumed that the grid's voltage source is stable on its own, and when $Z_g(s) = 0$, the IBR's current source is stable as well. With these assumptions, the goal is to derive a condition in which the current in this interconnected system is and remains stable.

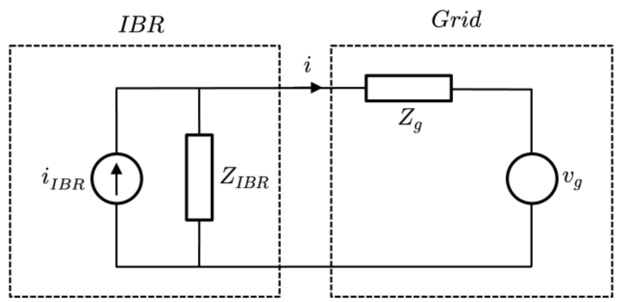

Figure 1-7 Equivalent small signal model of the grid-tied IBR

The current in this model is obtained as follows:

$$I(s) = (I_{IBR}(s) - \frac{v_g(s)}{Z_{IBR}(s)}) \times \frac{1}{1 + Z_g(s)/Z_{IBR}(s)} \tag{1.72}$$

Based on the stability assumption in the previous section, the first term in (1.72 is stable, and if the second term is stable (satisfying the Nyquist stability criterion), the system is stable.

To apply this criterion to the inverter system, the following model for the grid equivalent is developed.

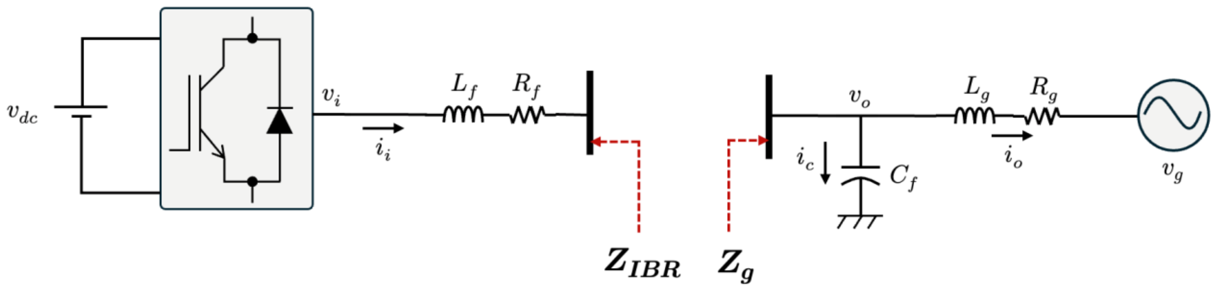

Figure 1-8 Partitioning the grid-tied IBR system for stability analysis

As depicted above, the grid is modelled as a series inductor and resistor. To conduct the stability analysis with the GNC, first the impedance behavior of the IBR, Z_{IBR}, needs to be obtained. Consider the following state space of a standalone IBR:

$$\frac{d}{dt}\begin{bmatrix}\Delta\gamma_d\\ \Delta\gamma_q\\ \Delta i_{id}^s\\ \Delta i_{iq}^s\\ \Delta\theta\\ \Delta\psi\end{bmatrix}=\begin{bmatrix}0 & 0 & -1 & 0 & -I_q^s & 0\\ 0 & 0 & 0 & -1 & I_d^s & 0\\ \frac{k_i}{L_f} & 0 & -\frac{k_p+R_f}{L_f} & 0 & \frac{-V_{iq}^s+\omega_0 L_f I_d^s-k_p I_q^s}{L_f} & 0\\ 0 & \frac{k_i}{L_f} & 0 & -\frac{k_p+R_f}{L_f} & \frac{V_{id}^s+\omega_0 L_f I_q^s+k_p I_d^s}{L_f} & 0\\ 0 & 0 & 0 & 0 & -k_p^{PLL}V_{od}^s & k_i^{PLL}\\ 0 & 0 & 0 & 0 & -V_{od}^s & 0\end{bmatrix}\begin{bmatrix}\Delta\gamma_d\\ \Delta\gamma_q\\ \Delta i_{id}^s\\ \Delta i_{iq}^s\\ \Delta\theta\\ \Delta\psi\end{bmatrix}$$
$$+\begin{bmatrix}1 & 0 & 0 & 0\\ 0 & 1 & 0 & 0\\ \frac{k_p}{L_f} & 0 & -\frac{1}{L_f} & 0\\ 0 & \frac{k_p}{L_f} & 0 & -\frac{1}{L_f}\\ 0 & 0 & 0 & k_p^{PLL}\\ 0 & 0 & 0 & 1\end{bmatrix}\begin{bmatrix}\Delta i_{id}^{ref}\\ \Delta i_{iq}^{ref}\\ \Delta v_{od}^s\\ \Delta v_{oq}^s\end{bmatrix} \tag{1.73}$$

$$\begin{bmatrix}\Delta i_{id}^s\\ \Delta i_{iq}^s\end{bmatrix}=\begin{bmatrix}0 & 0 & 1 & 0 & 0 & 0\\ 0 & 0 & 0 & 1 & 0 & 0\end{bmatrix}\begin{bmatrix}\Delta\gamma_d\\ \Delta\gamma_q\\ \Delta i_{id}^s\\ \Delta i_{iq}^s\\ \Delta\theta\\ \Delta\psi\end{bmatrix} \tag{1.74}$$

To develop the admittance behavior of this system, the following transfer function, $G=\frac{y}{U}=C\times(sI-A)^{-1}B$, based on the abovementioned state space.

$$\begin{bmatrix}\Delta i_{id}^s\\ \Delta i_{iq}^s\end{bmatrix}=\begin{bmatrix}G_{11} & G_{12} & G_{13} & G_{14}\\ G_{21} & G_{22} & G_{23} & G_{24}\end{bmatrix}\begin{bmatrix}\Delta i_{id}^{ref}\\ \Delta i_{q}^{ref}\\ \Delta v_{od}^s\\ \Delta v_{oq}^s\end{bmatrix} \tag{1.75}$$

Since the system is linear hence superposition rule holds, by assuming $\Delta i_{id}^{ref} = \Delta i_{iq}^{ref} = 0$, the admittance of the inverter as a function of frequency as follows:

$$Y_{IBR} = Z_{IBR}^{-1} = \begin{bmatrix} Y_{dd} & Y_{dq} \\ Y_{qd} & Y_{qq} \end{bmatrix} = \begin{bmatrix} G_{13} & G_{14} \\ G_{23} & G_{24} \end{bmatrix} \tag{1.76}$$

$$Y_{dd} = -\frac{s}{k_i + (R_f + k_p)s + L_f s^2} \tag{1.77}$$

$$Y_{dq} = -\frac{I_{iq}k_i k_i^{PLL} + \left(V_{iq}k_i^{PLL} + I_{iq}k_i k_p^{PLL} + I_{iq}k_i^{PLL}k_p - I_{id}L_f k_i^{PLL}\right)s + \left(V_{iq}k_p^{PLL} + I_{iq}k_p k_p^{PLL} - I_{id}L_f k_p^{PLL}\omega_s\right)s^2}{(s^2 + V_{od}k_p^{PLL}s + V_{od}k_i^{PLL})(k_i + (R_f + k_p)s + L_f s^2)} \tag{1.78}$$

$$Y_{qd} = 0 \tag{1.79}$$

$$Y_{qq} = \frac{I_{id}k_i k_i^{PLL} + \left(V_{id}k_i^{PLL} - V_{od}k_i^{PLL} + I_{id}k_i k_p^{PLL} + I_{id}k_p k_i^{PLL} - I_{iq}L_f k_i^{PLL}\omega_s\right)s + \left(V_{id}k_p^{PLL} - V_{od}k_p^{PLL} + I_{id}k_p k_p^{PLL} + I_{iq}L_f k_p^{PLL}\omega_s\right)s^2 - s^3}{(s^2 + V_{od}k_p^{PLL}s + V_{od}k_i^{PLL})(k_i + (R_f + k_p)s + L_f s^2)} \tag{1.80}$$

Now that the admittance is derived, the impedance ratio can be formed, and the eigenvalues are obtained as follows:

$$L = Z_g(s) \times Y_{IBR}(s) = \begin{bmatrix} L_{11}(s) & L_{12}(s) \\ L_{21}(s) & L_{22}(s) \end{bmatrix} \tag{1.81}$$

$$\begin{pmatrix} e_1(s) \\ e_2(s) \end{pmatrix} = \frac{1}{2} \times \begin{pmatrix} L_{11}(s) + L_{22}(s) - \sqrt{L_{11}^2(s) - 2L_{11}(s)L_{22}(s) + L_{22}^2(s) + 4L_{12}(s)L_{21}(s)} \\ L_{11}(s) + L_{22}(s) + \sqrt{L_{11}^2(s) - 2L_{11}(s)L_{22}(s) + L_{22}^2(s) + 4L_{12}(s)L_{21}(s)} \end{pmatrix} \tag{1.82}$$

The loci of these eigenvalues are utilized to study the stability of the grid-tied IBR system.

1.6 LVRT grid code

Figure 1-9 a) and Figure 1-9 b) demonstrate typical requirements for the operation of IBRs in facing faults that cause voltage sags.

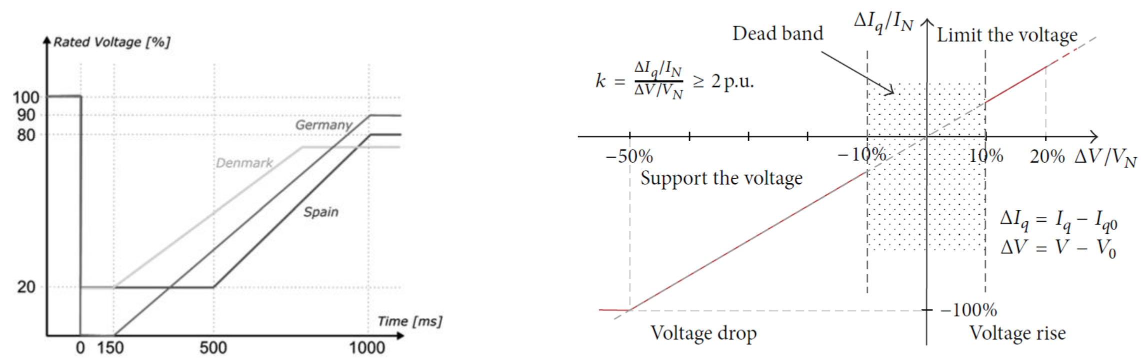

a) b)

Figure 1-9 a) LVRT requirement in Germany, Denmark, and Spain b) Reactive power requirement grid code upon low voltage events [12]

The current output of the inverter must also be limited to a certain maximum value, as stated in (1.83.

$$\sqrt{I_{id}^2 + I_{iq}^2} < I_{max} \tag{1.83}$$

Where $I_{max} = kI_n$, where I_n is the nominal current of the inverter and k is typically equal to 1.2. similar constraints are considered for the voltage as follows:

$$\sqrt{v_{id}^2 + v_{iq}^2} < V_{max} \tag{1.84}$$

With these limitations in mind, in this project the LVRT logic is implemented as follows.

ALGORITHM 1: LVRT LOGIC

Input v_{id}
$\boldsymbol{I_{iq}^{check} = 2(1 - v_{id})I_N}$
If $v_{id} > 0.9$
  $I_{iq}^{modified} = I_{iq}^{ref}$; $I_{id}^{modified} = I_{id}^{ref}$
If $v_{id} \leq 0.9$
  If $I_q^{check} \geq I_{max}$
    $I_{iq}^{modified} = I_{max}$; $I_d^{modified} = 0$
  If $I_q^{check} < I_{max}$
    $I_q^{modified} = I_q^{check}$
    If $I_d^{no\ limit} \geq \sqrt{I_{max}^2 - \left(I_q^{check}\right)^2}$
      $I_d^{modified} = \sqrt{I_{max}^2 - \left(I_q^{check}\right)^2}$
    If $I_d^{no\ limit} < \sqrt{I_{max}^2 - \left(I_q^{check}\right)^2}$
      $I_d^{modified} = I_d^{no\ limit}$

1.7 Numerical analysis

The analysis is conducted in two sections. First, case studies are designed to examine and compare the effectiveness of the two stability analysis tools to understand how the strength of the grid can affect the synchronization stability of the grid-tied IBR system. In the second part, time domain simulations are conducted to study the effect of delay in the LVRT grid code on the TOV given various grid strengths.

1.7.1 Grid Synchronization Stability analysis

In this section, a test system with the parameters shown in Table 1 is studied.

Table 1 Parameters of the VSC

Parameter	Value
k_p	0.023
k_i	25.59
k_p^{PLL}	4.46, 8.92, 17.84
k_i^{PLL}	991, 3964, 15860
ω_s	$2\pi \times 60\ rad/s$
R_f	120 $m\Omega$
L_f	970 μH
C_f	10 μF
I_{id}^s	-11 Amp
I_{iq}^s	0 Amp
v_{id}^s	100 v
v_{iq}^s	0 v
v_{od}^s	99.9 v
v_{oq}^s	0 v

To start with, the impedance/admittance behavior of the IBR is studied. This admittance was derived in (1.76. To understand the effect of PLL bandwidth on the impedance behavior, three different sets of PLL parameters in the increasing order. The results are as follows:

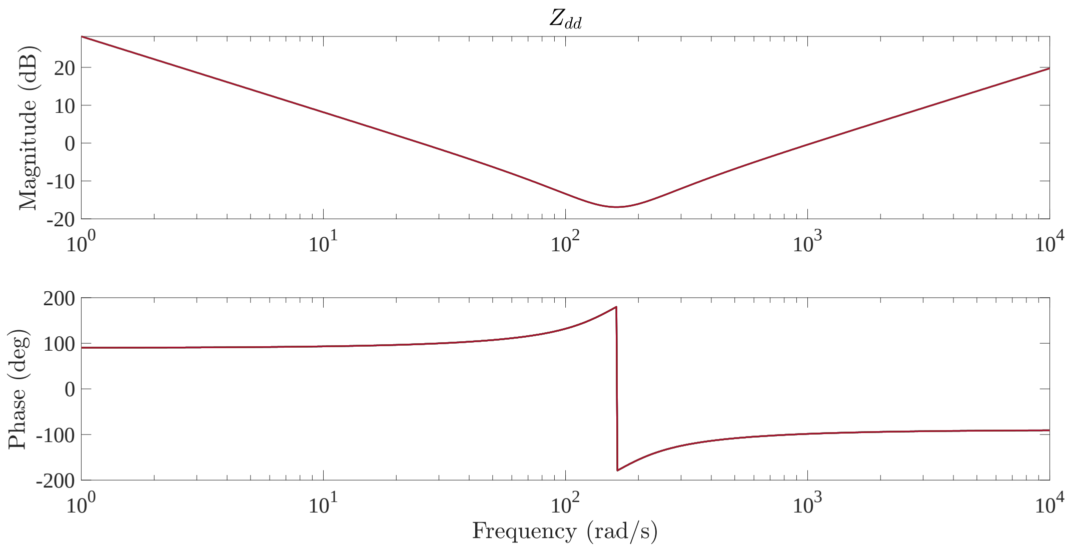

Figure 1-10 dd channel impedance of the IBR

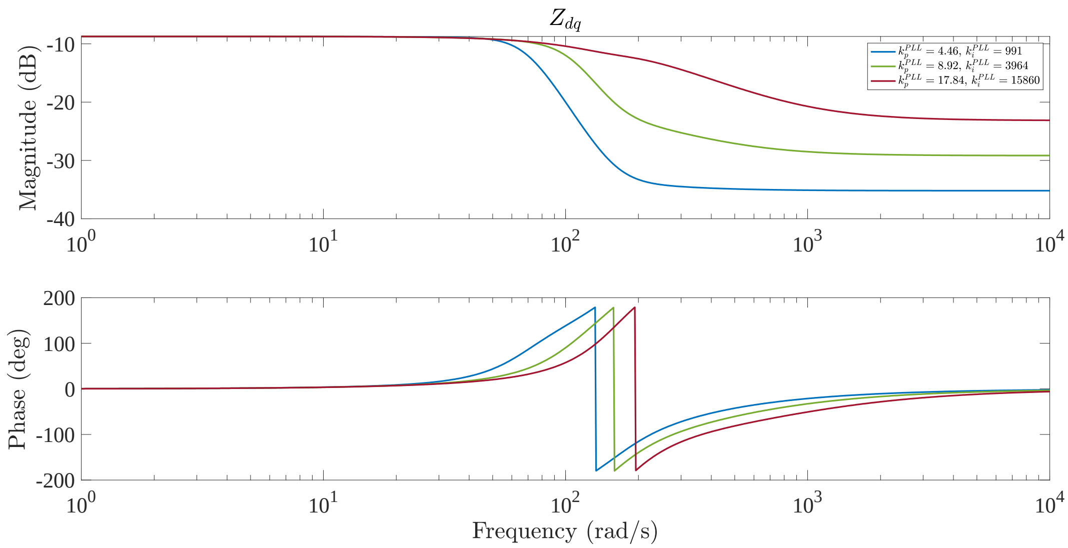

Figure 1-11 dq channel impedance of the IBR

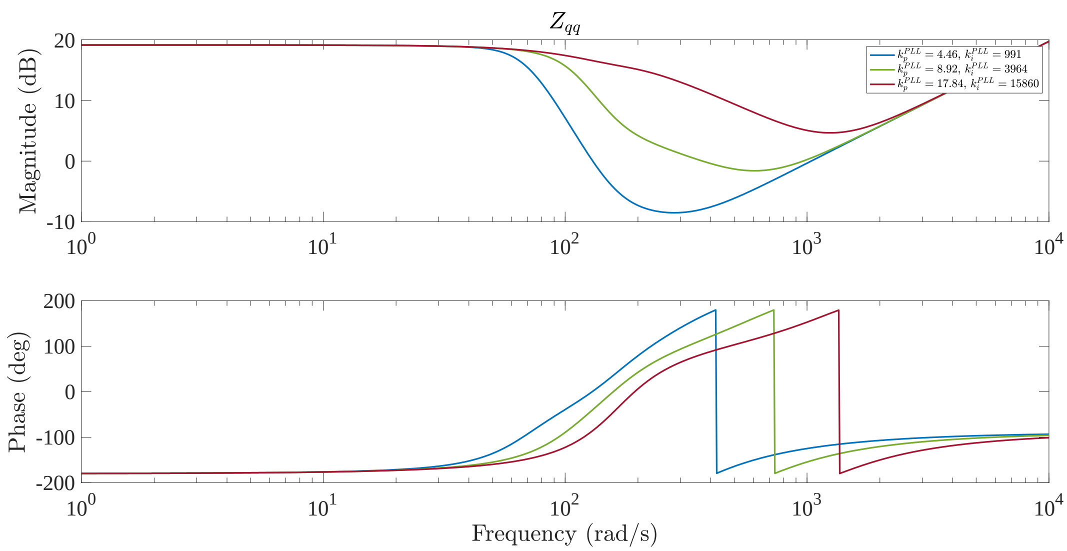

Figure 1-12 qq channel impedance of the IBR

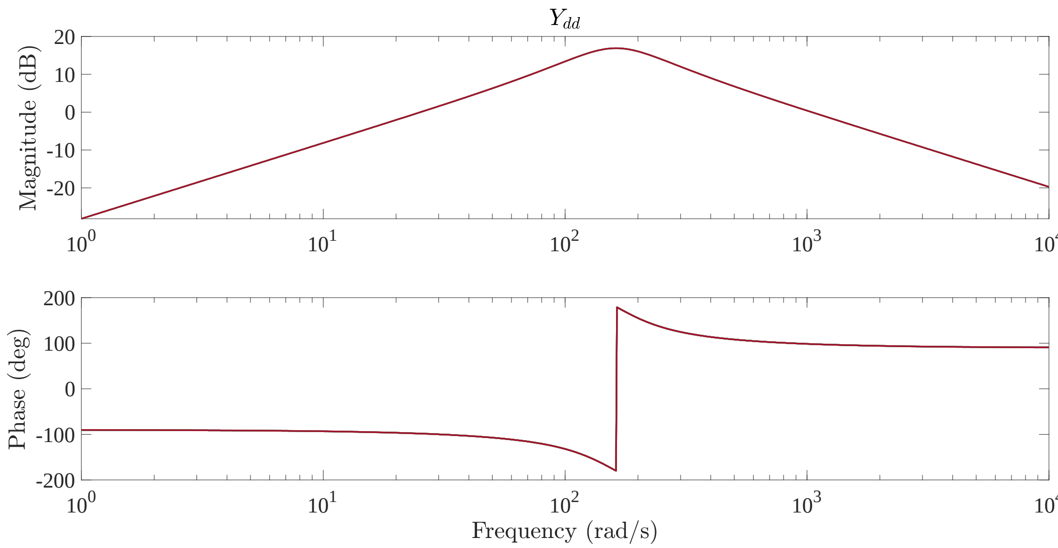

Figure 1-13 dd channel admittance of the IBR

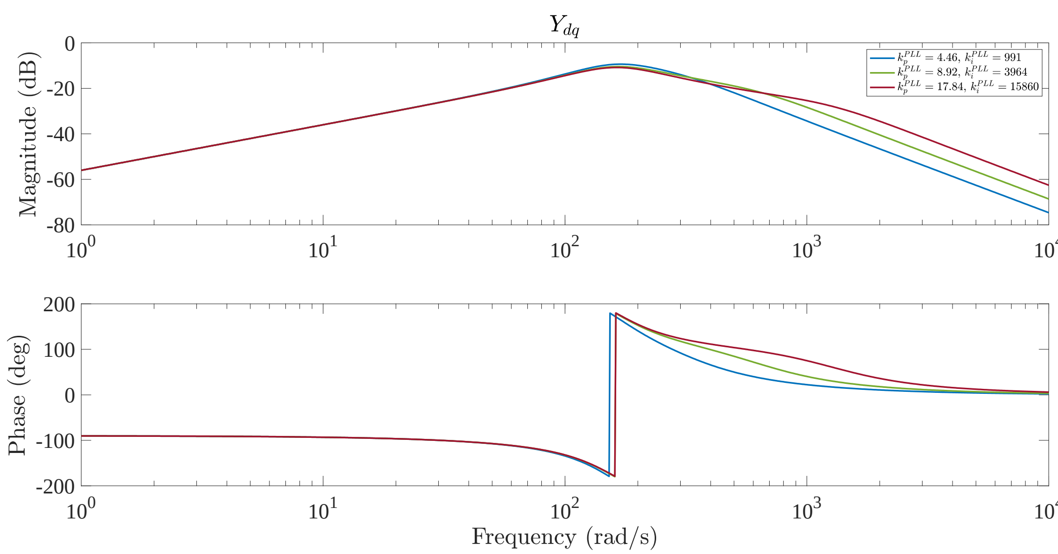

Figure 1-14 dq channel admittance of the IBR

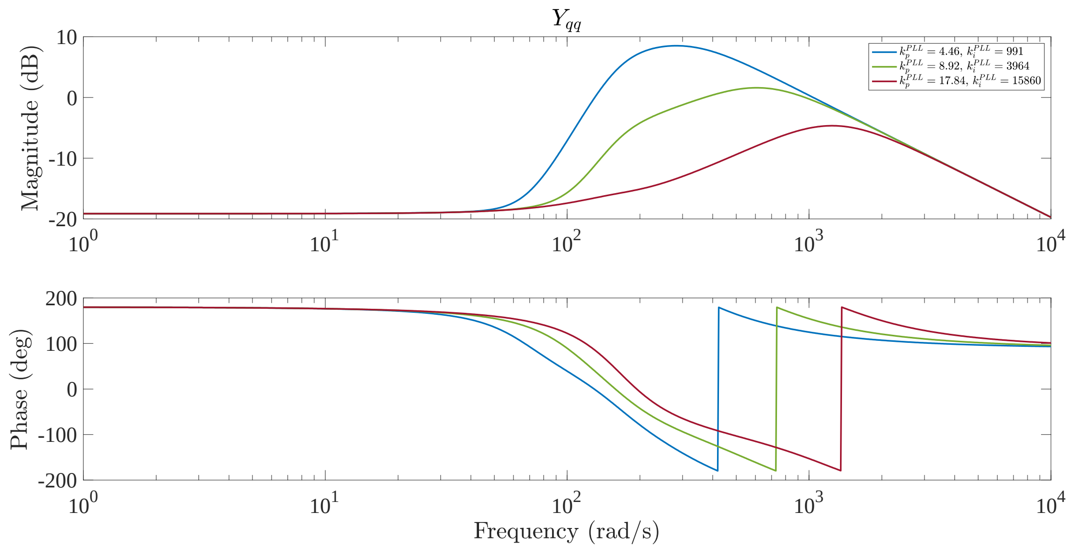

Figure 1-15 qq channel admittance of the IBR

The main takeaway from these impedance behaviors is that the matrix is close to diagonal, as the qd channel is zero, and the dq channel is sufficiently small. In addition, the qq channel acts as a negative resistance where the bandwidth of the PLL determines the range of frequency for this behavior, as depicted in Figure 1-12.

Next, this IBR is synchronized with a grid and the effect of various grid strengths on the grid synchronization stability of the IBR system is studied.

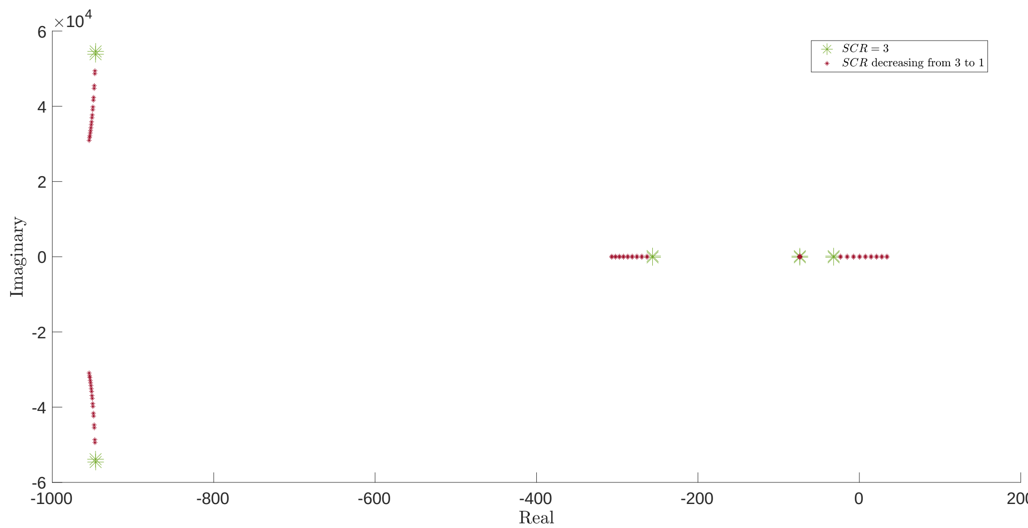

Figure 1-16 Eigenvalues of the grid-tied IBR system as a function of grid strength.

As shown in Figure 1-16, when the grid is strong, the interconnection is stable. The system as modelled in (1.68 has 10 modes, and when $\mathsf{SCR} = \mathit{3}$ (the green dots in Figure 1-16), the system is small signal stable. This is also verified in the GNC plot of the system in Figure 1-17, as the eigenvalues do not cross the critical point.

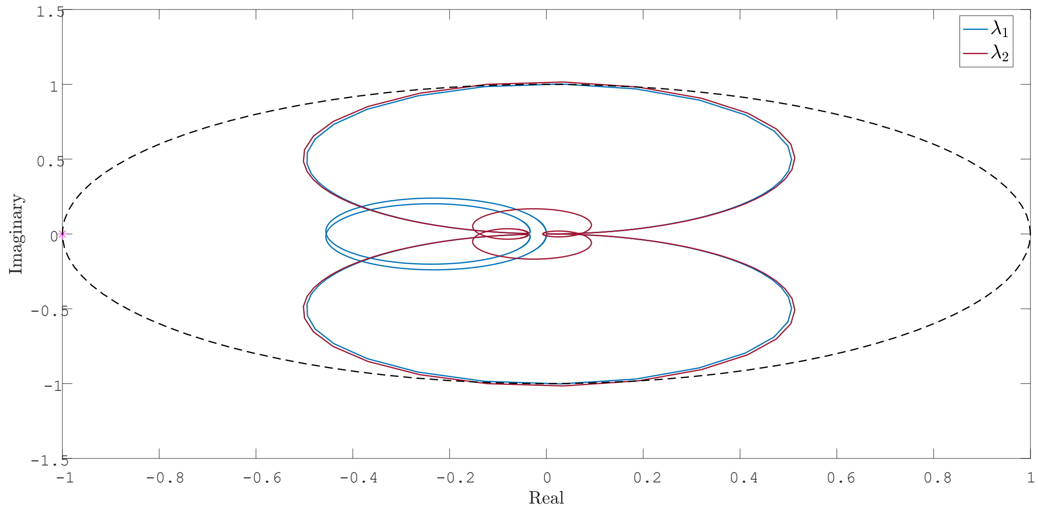

Figure 1-17 GNC plot of the grid-tied IBR system at $\text{SCR} = 3$

Next, the grid strength has been reduced. As depicted in Figure 1-16, as the grid becomes weaker (higher impedance) at some point the two modes on the right cross the $j\omega$ axis which indicates the loss of synchronism and instability of the system. This result is also verified using the following three GNC plots in Figure 1-18, Figure 1-19, and Figure 1-20. As the strength decreases, λ_1 moves towards the critical point and as shown in Figure 1-20, at $\text{SCR} = 1$ the loci encircles the critical point twice.

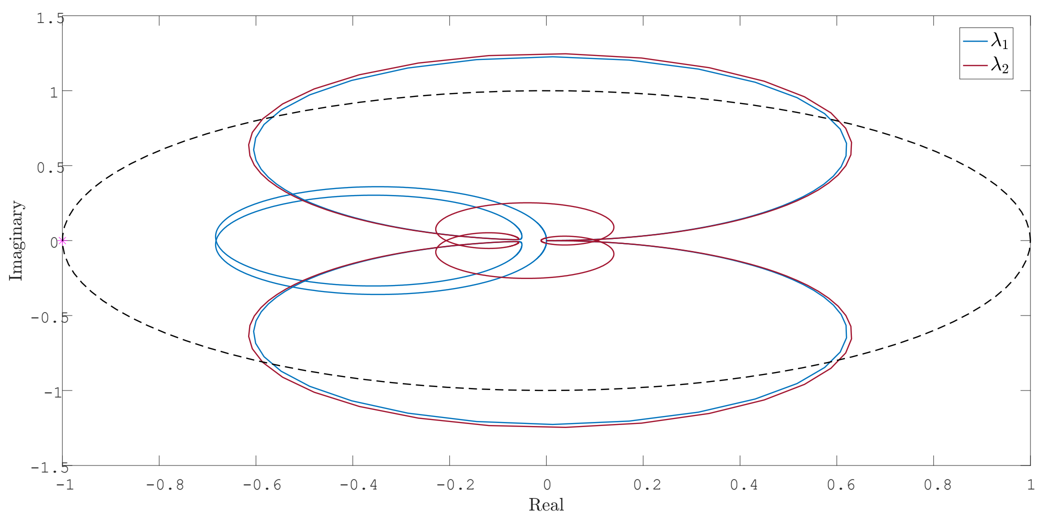

Figure 1-18 GNC plot of the grid-tied IBR system at $\text{SCR} = 2$

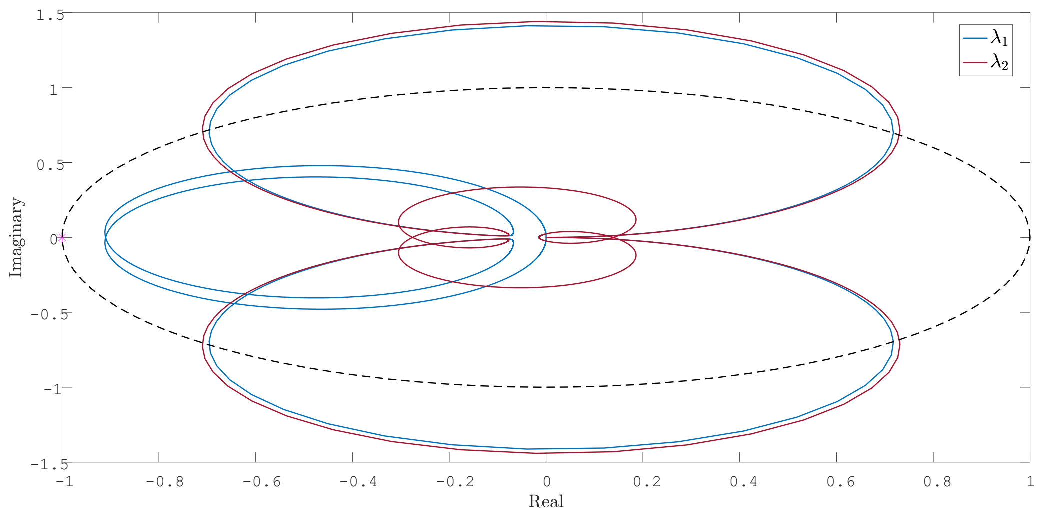

Figure 1-19 GNC plot of the grid-tied IBR system at $\mathsf{SCR} = \mathit{1.5}$

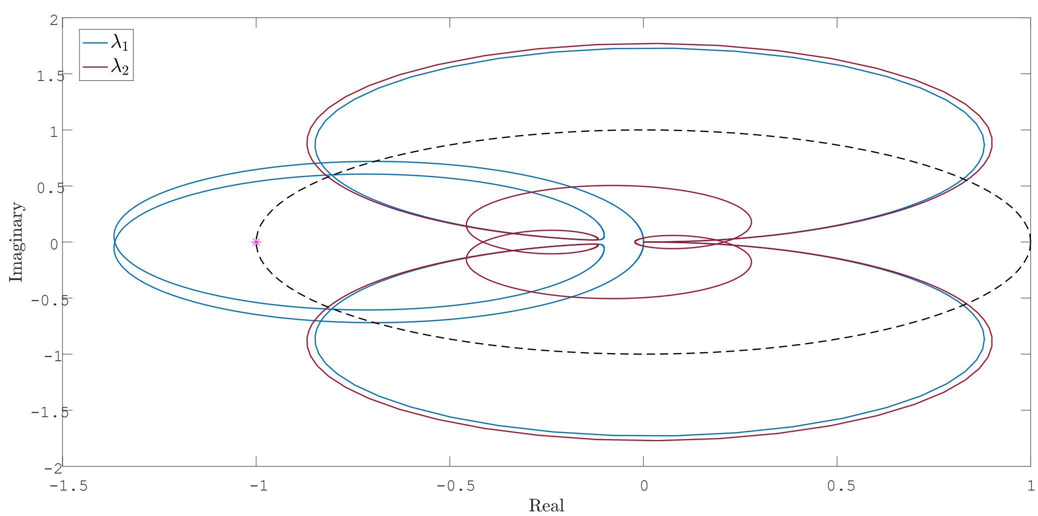

Figure 1-20 GNC plot of the grid-tied IBR system at $\mathsf{SCR} = \mathit{1}$

1.7.2 Time domain simulations

In this section impact of delay in the LVRT logic and grid strength are studied. The delays are related to the time required by the LVRT to detect the exact fault clearance time to switch between during fault and post fault conditions. To start with, the grid-tied IBR system as depicted in Figure 1-21 is simulated in MATLAB/Simulink®, the difference being that the IBR is connected to the grid via two identical transmission lines. In this system, $S_{IBR} = 100\ kVA$, and the output voltage of the inverter is 500 v. The IBR is connected to the grid via two identical transmission lines where the voltage is boosted and decreased at the terminals of the transmission lines via a 500⁄69 kV and a 69⁄500 V transformers, respectively. In addition, a PLL is utilized to track the grid's angle and frequency, based on which the IBR controller operates. A three-phase symmetrical fault occurs on one of the transmission lines at $t = 0.2\ s$. This fault is cleared after $0.1\ s$. In the first scenario, it is assumed that the grid is strong ($\text{SCR} = 20$), and the fault is cleared by itself, hence, the grid's strength remains unchanged. Once a voltage sag is detected, the LVRT is used based on Algorithm 2.

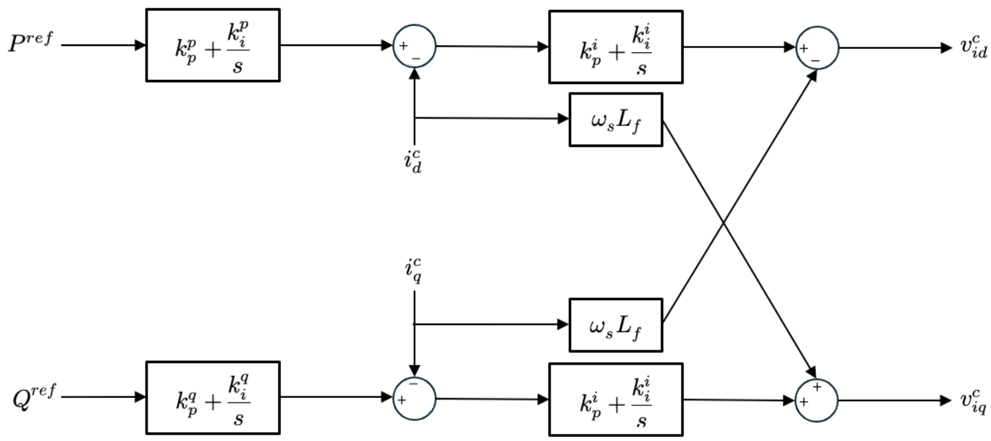

Figure 1-21 cascaded inner/outer control loops

First, assume an operating condition where there is zero controller action delay. The grid is strong (SCR = 20), and a three-phase symmetrical fault occurs on one of the lines at 0.2 s, and lasts for 0.01 s (Case 1). Figure 1-22 shows the voltage profile at POI.

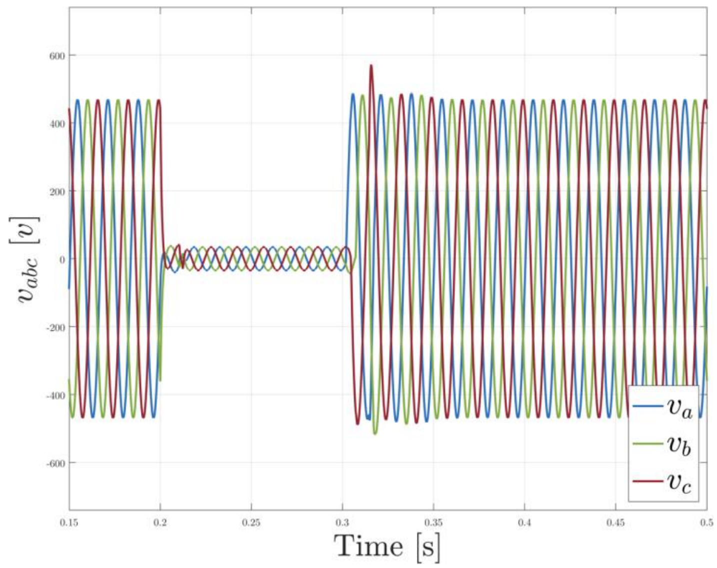

Figure 1-22 Case one with zero delay, max is $572.5\ v$, steady state $469.5\ v$

Next, a $5\ ms$ delay is introduced to the LVRT grid code action. This indicates that for $5\ ms$ after the fault clearance, the IBR keeps on injecting reactive power to support the grid as depicted in Figure 1-23. Same results are also presented with $10\ ms$, $20\ ms$, and $30\ ms$ delay in Figure 1-24, Figure 1-25, and Figure 1-26, respectively. It is shown that in a strong grid interconnection, the TOV duration is proportional to the delay, but this relationship is not necessarily linear.

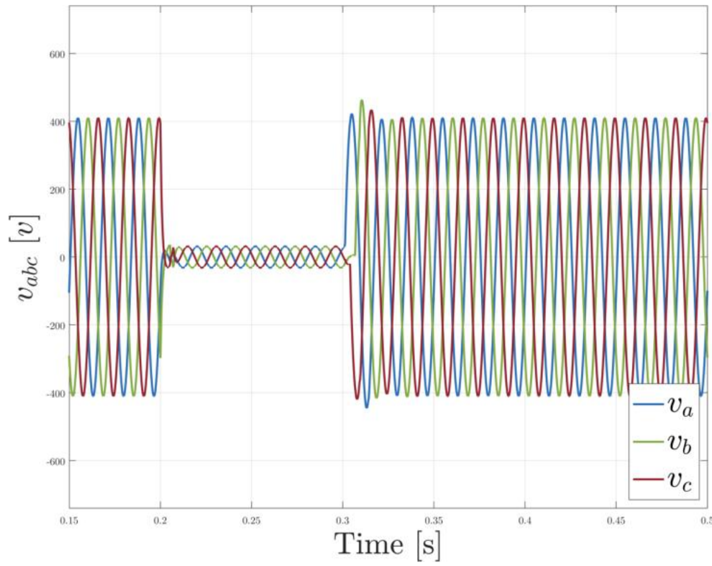

Figure 1-23 Case one with $5\ ms$ delay, max is $464.5\ v$, steady state $410\ v$

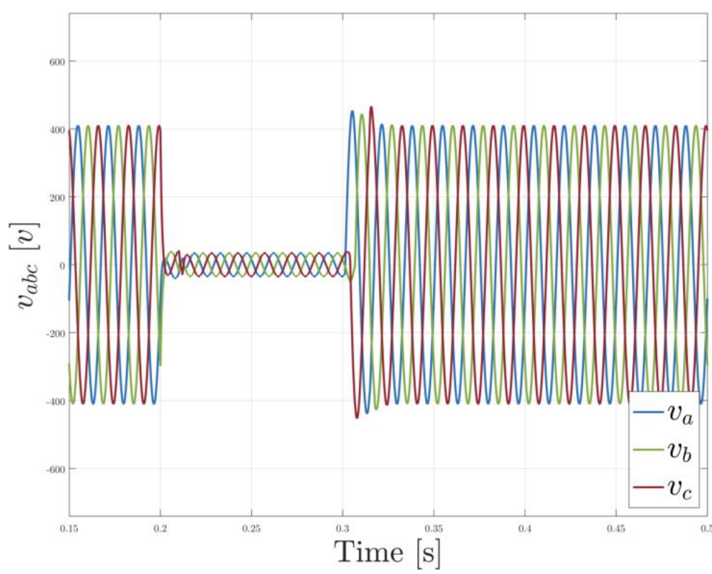

Figure 1-24 Case one with $10\ ms$ delay, max is $467.5\ v$, steady state $412\ v$

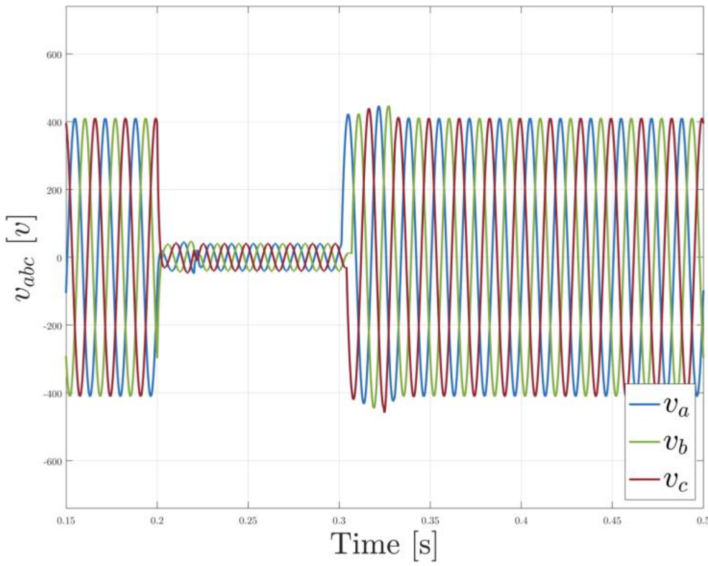

Figure 1-25 Case one with *20 ms* delay, max is *448.5 v*, steady state *412 v*

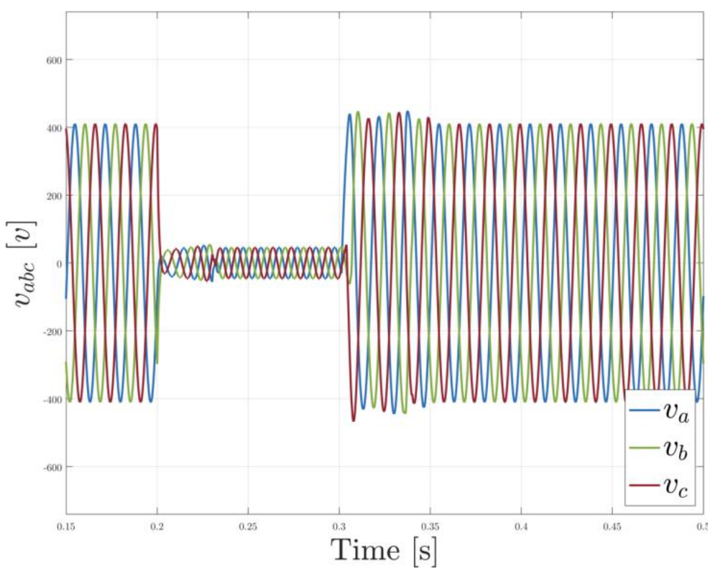

Figure 1-26 Case one with *30 ms* delay, max is *448.5 v*, steady state *412 v*

Next, it is assumed that the grid is weak, and after fault clearance, the strength remains unchanged. In the following analysis, SCR = 1 at pre fault, during fault, and post fault (Case 2). The TOV results for different delays are depicted in Figure 1-27 and Figure 1-28. The TOV magnitude and severity are worse than the strong grid and possible instable condition may occur. The strong grid can accommodate a faster PLL and tolerate longer delays, unlike the weak system. For instance, any delay longer than *10 ms* causes the IBR loses its synchronism.

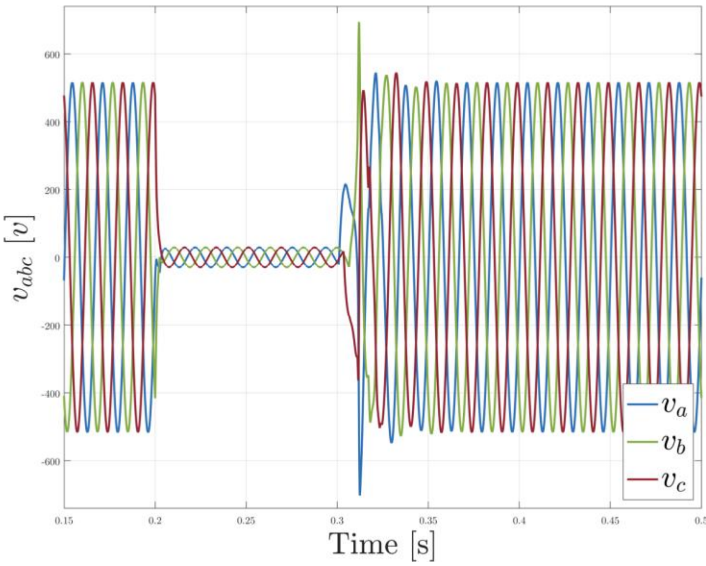

Figure 1-27 Case two with $0\ ms$ delay, max is $695.5\ v$, steady state $517\ v$

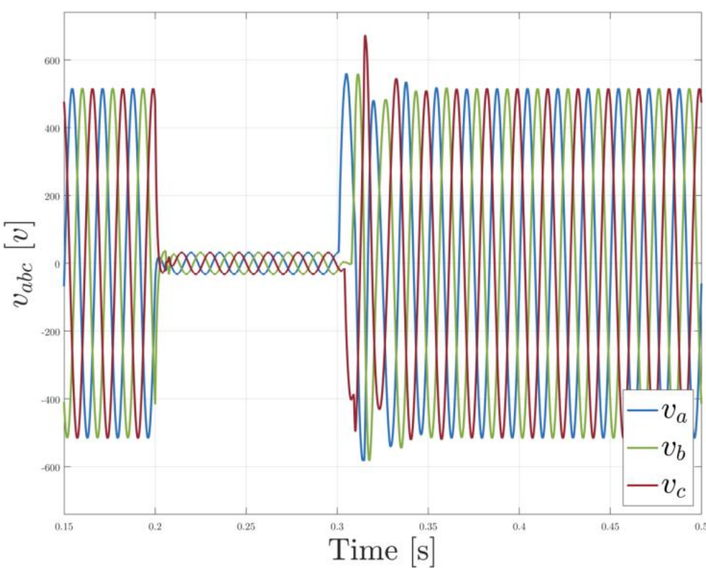

Figure 1-28 Case two with $5\ ms$ delay, max is $673.5\ v$, steady state $517\ v$

Another case that is investigated is when the strength changes after the fault clearance (Case 3) in which the faulted lone is taken out of service to clear the fault. As depicted in Figure 1-29 to Figure 1-32, compared to the two other cases, the change in the grid's strength causes a more severe TOV.

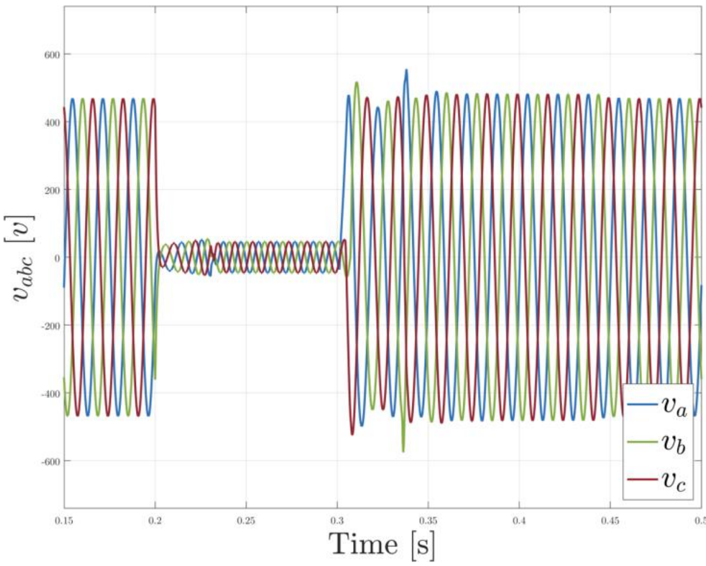

Figure 1-29 Case three with *0* ms delay, max is *556.5* v, steady state *468* v

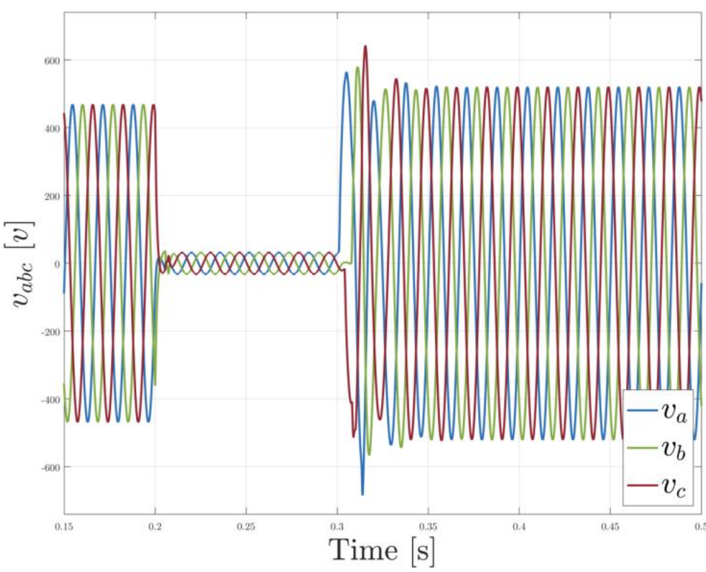

Figure 1-32 Case three with *5* ms delay, max is *643.5* v, steady state *521* v

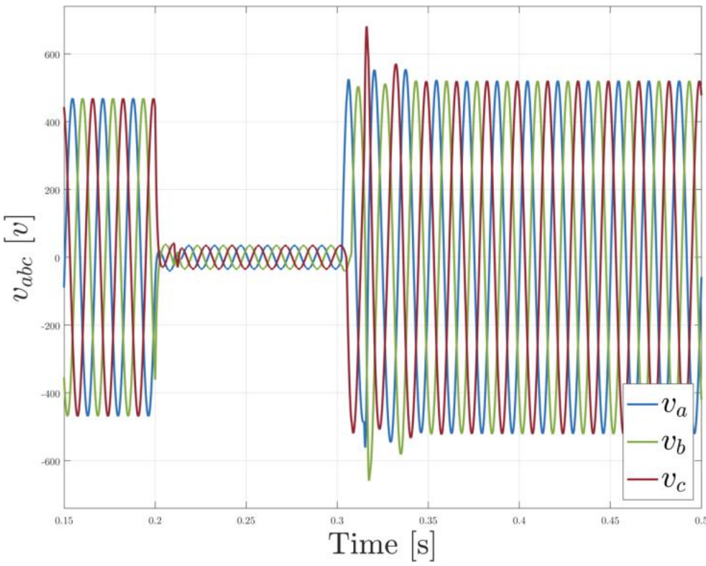

Figure 1-30 Case three with *10 ms* delay, max is *682.5 v*, steady state *521 v*

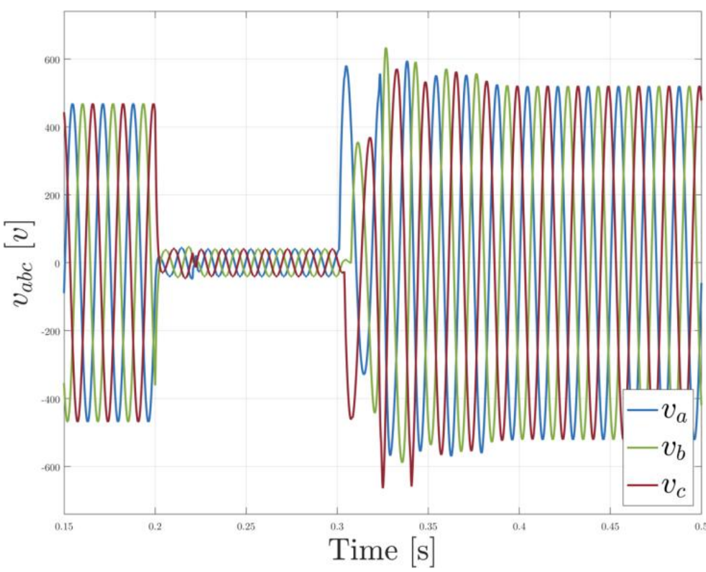

Figure 1-31 Case three with *20 ms* delay, max is *665.5 v*, steady state *521 v*

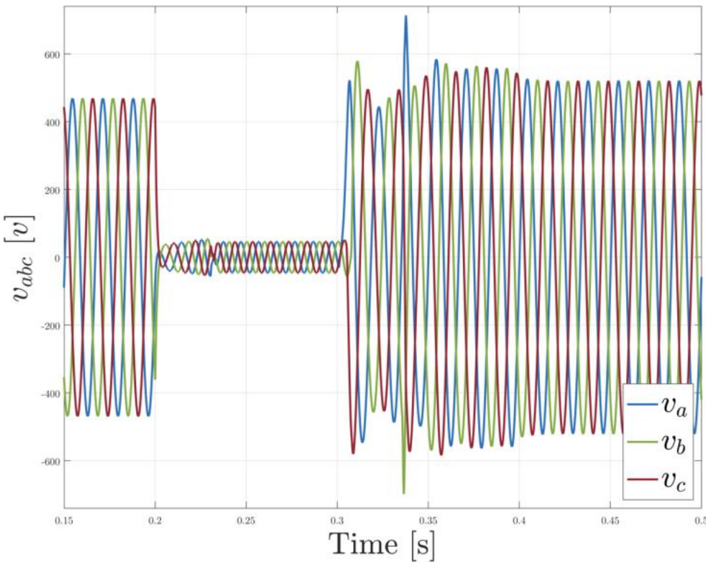

Figure 1-32 Case three with $30\ ms$ delay, max is $413.5\ v$, steady state $521\ v$

In addition, the effect of PLL dynamics is investigated. In Case 1, in the presence of $20\ ms$ delay, the PLL bandwidth is increased from $484.13\ Hz$ to $4110.3\ Hz$, which is the maximum PLL speed for which the system to remain stable during the post fault. The TOV profile is depicted in Figure 1-33. Next, for the same setup, in Case three, the PLL bandwidth is increased to $1686.2\ Hz$. As stated before, in a weak grid, the PLL bandwidth is limited compared to a strong grid. In addition, weaker grids exhibit larger TOVs and a higher risk of synchronization instability, as depicted in Figure 1-34 and Figure 1-35.

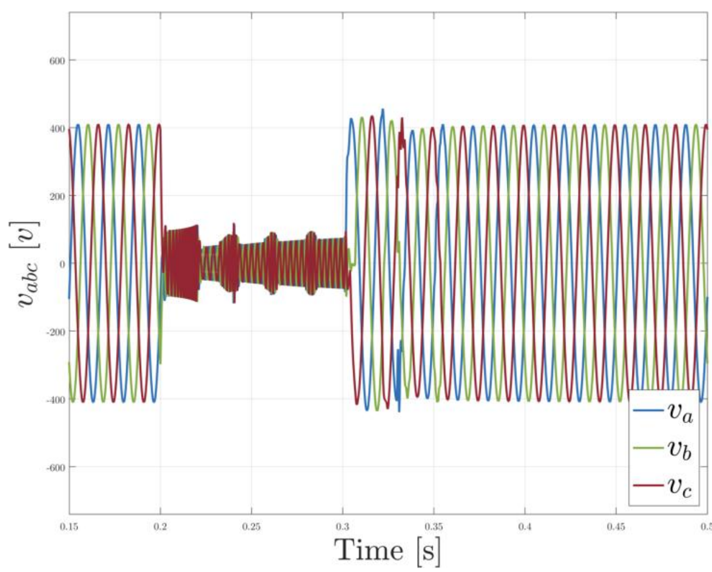

Figure 1-33 Case one with $20\ ms$ delay, max is $453.5\ v$, steady state $412\ v$, faster PLL

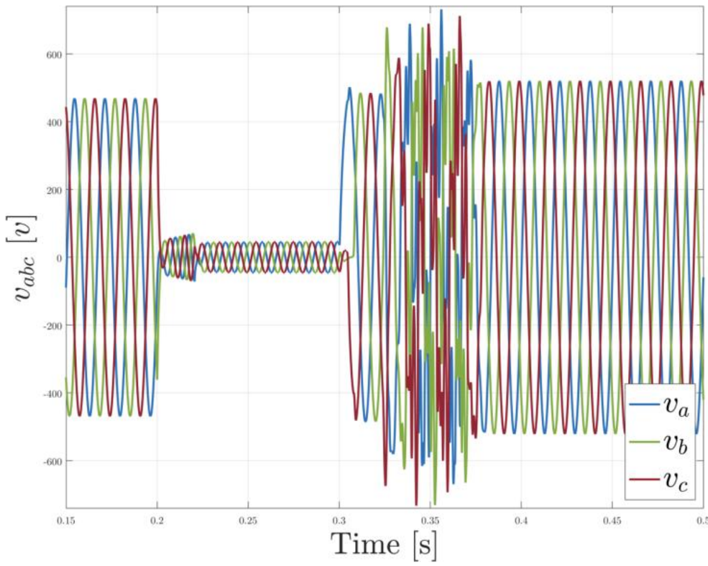

Figure 1-34 Case three with $20\ ms$ delay, max is $732.5\ v$, steady state $521\ v$, faster PLL

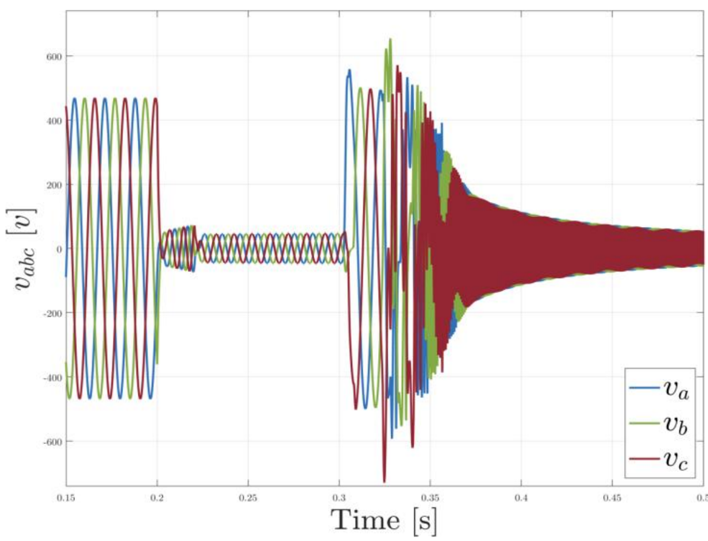

Figure 1-35 Case three, instability with faster PLL bandwidth

1.8 Conclusions

In this report, the TOV phenomenon caused by IBR dominated power systems was studied in detail. Given that grid strength is directly correlated with numerous issues caused by GFL IBRs, a thorough study and comparison of various strength indices were conducted. Since the conventional SCR fails to measure grid strength in many different configurations, it is crucial to choose an approach that captures the desired dynamics of the grid under study. Subsequently, a model-based approach was developed to calculate the impedance behavior of the grid-tied IBR system. Stability analysis using GNC, and conventional eigenvalue analysis was performed, and the results of each method were cross-checked. Finally, a time-domain simulation was conducted to perform a parametric study on the effects of controller action delay in causing TOVs at the POI. The results validate that weak systems exhibit more severe TOVs and are prone to loss of synchronism.

References

[1] "IEEE Recommended Practice for Surge Voltages in Low-Voltage AC Power Circuits," *IEEE Std C6241-1991*, pp. 1–112, Oct. 1991, doi: 10.1109/IEEESTD.1991.101029.

[2] "Risk Assessment of Post-Fault Temporary Overvoltage Using Generalized Short-Circuit Ratio | IEEE Journals & Magazine | IEEE Xplore." Accessed: Feb. 19, 2024. [Online]. Available: https://ieeexplore.ieee.org/document/10035300

[3] "RAPA - Short-Circuit Modeling and System Strength..." Accessed: May 17, 2024. [Online]. Available: https://www.nerc.com/pa/RAPA/Lists/RAPA/DispForm.aspx?id=291&Source=https://www.nerc.com/pa/RAPA/Pages/Calendar.aspx

[4] M. O. Qays, I. Ahmad, D. Habibi, A. Aziz, and T. Mahmoud, "System strength shortfall challenges for renewable energy-based power systems: A review," *Renew. Sustain. Energy Rev.*, vol. 183, p. 113447, Sep. 2023, doi: 10.1016/j.rser.2023.113447.

[5] "Systems with multiple DC Infeed." Accessed: Jun. 04, 2024. [Online]. Available: https://www.e-cigre.org/publications/detail/364-systems-with-multiple-dc-infeed.html

[6] D. Wu, G. Li, M. Javadi, A. M. Malyscheff, M. Hong, and J. N. Jiang, "Assessing Impact of Renewable Energy Integration on System Strength Using Site-Dependent Short Circuit Ratio," *IEEE Trans. Sustain. Energy*, vol. 9, no. 3, pp. 1072–1080, Jul. 2018, doi: 10.1109/TSTE.2017.2764871.

[7] "Connection of wind farms to weak AC networks." Accessed: Apr. 15, 2024. [Online]. Available: https://www.e-cigre.org/publications/detail/671-connection-of-wind-farms-to-weak-ac-networks.html

[8] C. Henderson, A. Egea-Alvarez, T. Kneuppel, G. Yang, and L. Xu, "Grid Strength Impedance Metric: An Alternative to SCR for Evaluating System Strength in Converter Dominated Systems," *IEEE Trans. Power Deliv.*, pp. 1–10, 2023, doi: 10.1109/TPWRD.2022.3233455.

[9] P. O. Dorile, D. R. Jagessar, L. Guardado, R. A. McCann, and M. Ahanch, "Grid Strength Assessment and Maximum Loadability of a Wind-Dominated Power System Through QV Modal Analysis," in *2021 IEEE PES/IAS PowerAfrica*, Aug. 2021, pp. 1–5. doi: 10.1109/PowerAfrica52236.2021.9543346.

[10] G. Wang, H. Xin, D. Wu, Z. Li, L. Huang, and P. Ju, "Generalized Short Circuit Ratio for Grid Strength Assessment in Inhomogeneous Multi-infeed LCC-HVDC Systems," Dec. 18, 2020, *arXiv*: arXiv:2011.07564. doi: 10.48550/arXiv.2011.07564.

[11] A. G. J. MAcFARLANE and I. POSTLETHWAITE, "The generalized Nyquist stability criterion and multivariable root loci," *Int. J. Control*, vol. 25, no. 1, pp. 81–127, Jan. 1977, doi: 10.1080/00207177708922217.

[12] M. Diaz, R. Cardenas, P. Wheeler, J. Clare, and F. Rojas, "Resonant Control System for Low-Voltage Ride-Through in Wind Energy Conversion Systems," *IET Power Electron.*, vol. 9, Feb. 2016, doi: 10.1049/iet-pel.2015.0488.

Part II

Temporary Overvoltages Analysis

Sakis A. P. Meliopoulos
George J. Cokkinides
Abdulaziz M. Qwbaiban, Graduate Student

Georgia Institute of Technology

For information about this project, contact

A.P. Meliopoulos
Georgia Institute of Technology
School of Electrical and Computer Engineering
Atlanta, GA 30332
Phone: 404-894-2926
Email: sakis.m@gatech.edu

Power Systems Engineering Research Center

The Power Systems Engineering Research Center (PSERC) is a multi-university Center conducting research on challenges facing the electric power industry and educating the next generation of power engineers. More information about PSERC can be found at the Center's website: http://www.pserc.org.

For additional information, contact:

Power Systems Engineering Research Center
Arizona State University
527 Engineering Research Center
Tempe, Arizona 85287-5706
Phone: 480-965-1643
Fax: 480-727-2052

Notice Concerning Copyright Material

Table of Contents

List of Figures

List of Tables

1. Introduction and Objectives

1.1 Introduction

Temporary overvoltages may occur due to various reasons such as transients in the filters, capacitors and other components of IBRs following fault clearing events or a fault onset. This report investigates impacts of such factors on the temporary overvoltages.

1.2 Objectives

The objectives of this project were to investigate the effects of temporary over-voltages on power systems with high concentration of inverter-based resources. Specifically:

- To model and realistically simulate power systems with high penetration of IBRs.
- To study the impact of different parameters in the system model on the temporary over- voltage peak values.
- To simulate and recreate the transient effects on existing legacy generator protection systems such as false triggering of loss of field (LOF) relay.
- Propose remedial actions to reduce the temporary over-voltage such as using estimation- based protection methods.

2. Proper Representation of Inverter-Based Resources in Transient Studies

This section discusses the importance of proper representation of inverter-based resources (IBR) in transient studies. It starts with the previous work done in developing IBR models discussing the pros and cons of each method. Then, it discusses the approach for IBR modeling in this project.

2.1 The Need of Proper IBR Modeling

The ever-increasing grid integration of inverter-based resources (IBRs) such as solar and wind power generation, battery energy storage systems (BESS) and HVDC systems challenges power systems control and operations [1=3]. Figure 2.1 [4] shows the recorded temporary overvoltage subsequent to the short-circuit in this incident.

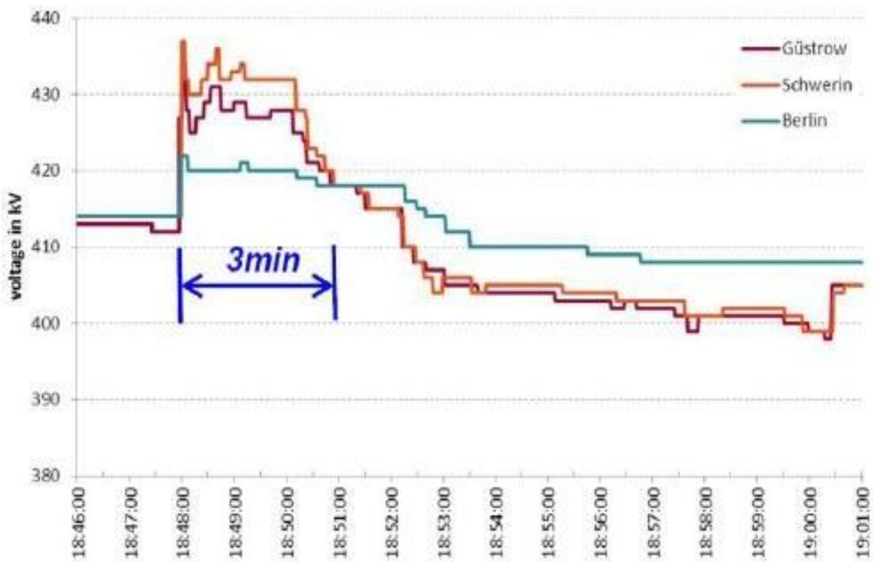

Figure 2.1: Temporary overvoltage subsequent to a short-circuit in the German transmission system in 2012 that caused tripping of wind turbines [4]

2.2 Literature review of Inverter-Based Resource Models for Transient Analysis

There are multiple studies conducted to observe the impact of modeling IBRs on the dynamic response of protection relays as well as the overall transient response. A slight deviation from the correct model can result in mis-operation of protection relays as well as not having proper EMT dynamic response.

The number of model parameters for IBR is essential to run EMT simulations with accurate transients' representation. The issue is that not many models are available to conduct EMT analysis along with sudden events or disturbances. The parameters the user is allowed to change do not have the capability to view the dynamic behavior of systems that experience sudden events [12-15].

Reference [11] indicates that there is almost no generally accepted models for EMT analysis in IBR dominated bulk power systems. In this work, the authors have developed a three-phase PV model via laboratory tests for commercial PV inverters. The developed model include active and reactive power models, DC source controller models, PI controller and current limiter for active and reactive power control, grid interconnection protection models, and converter models. Figure 2.2 shows the block diagram of the IBR model developed in [11].

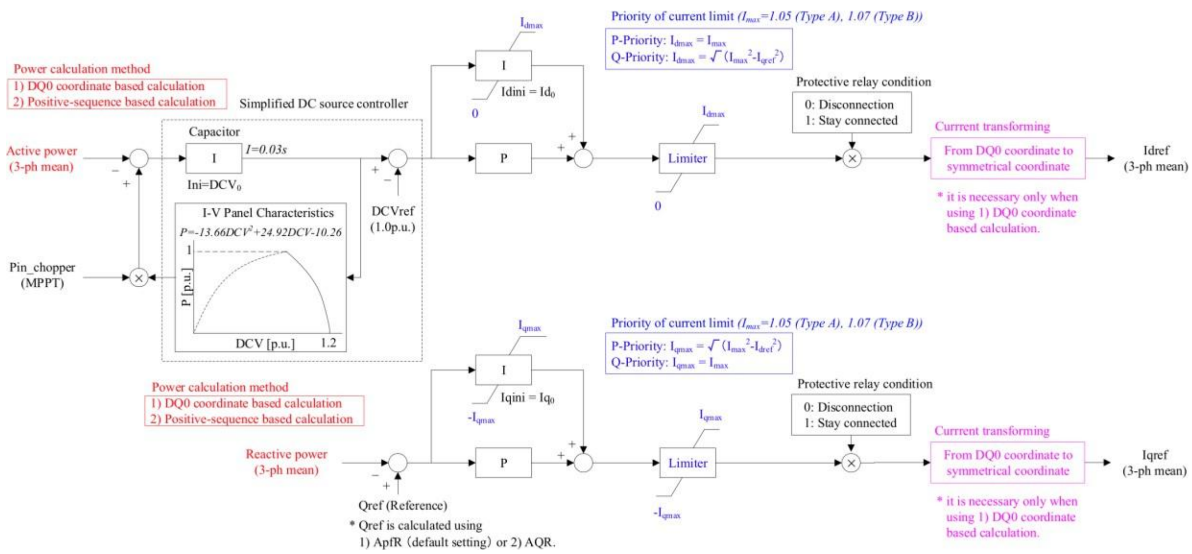

Figure 2.2: Block diagram of the IBR model developed in [11]

EPRI, University of Washington, University of Illinois Urbana Champaign, and University of Minnesota have developed IBR generic grid forming positive sequence models to be implemented in PSCAD simulations [10]. The models can represent four types of control methods such as droop-characteristic based models and virtual synchronous machines based models. The model is a structure as a modular fashion where parameters can be adjusted in a graphical user interface. This model is widely used in the industry for EMT modeling but requires having the PSCAD software. Figure 2.3 shows the mathematical block diagram for the PSCAD model.

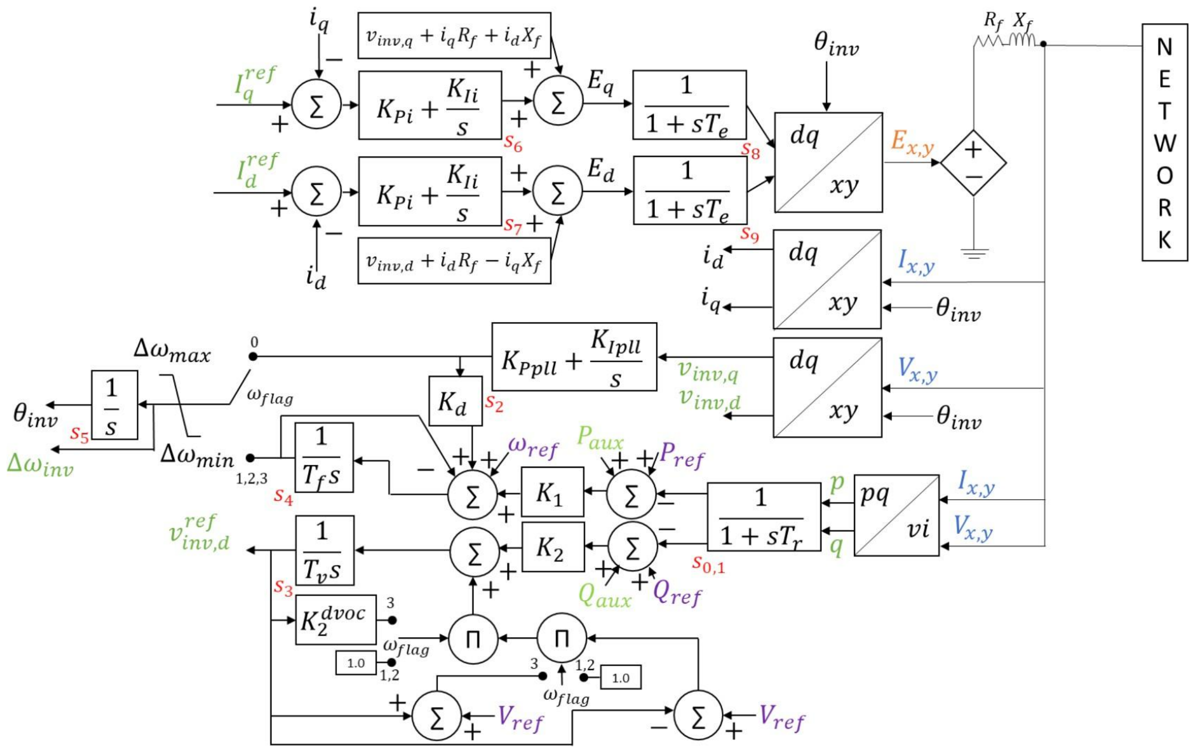

Figure 2.3: Block diagram of the IBR model developed in [10]

Reference [16] describes modules for central station PV plants connected to 60 kV or above transmission networks. Figure 2.4 presents distributed PV modules that integrate multiple subsystems into a single dynamic system. The models follow IEEE Standard 1547 where deployed models operate in constant power factor of constant reactive power control modes.

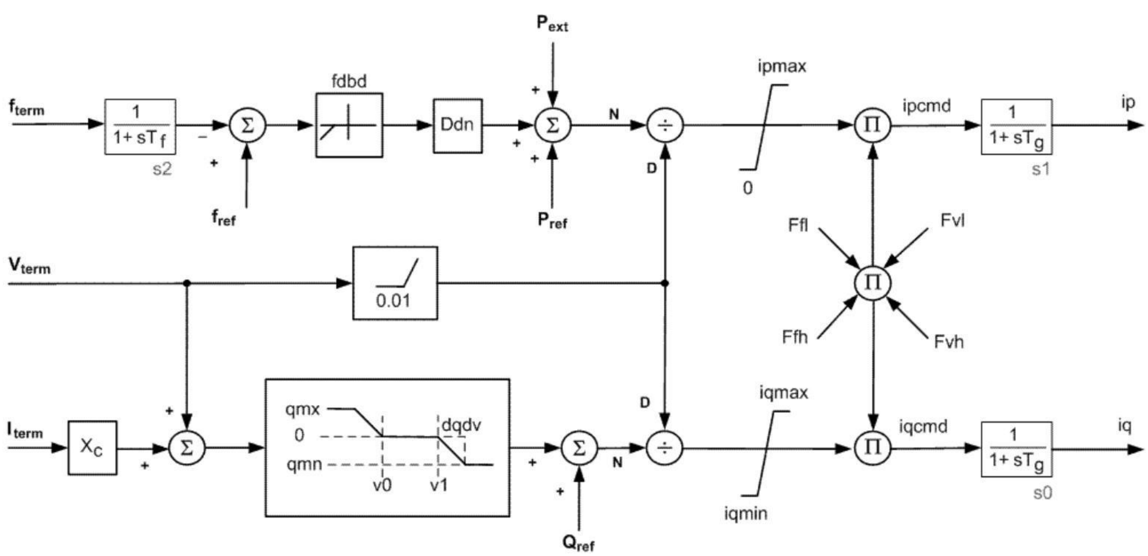

Figure 2.4: Block diagram of the IBR model developed in [16]

2.3 Developed Models of IBR for this Project

The developed models are used for (a) estimation-based protection of IBRs, and (b) simulation of temporary overvoltages in IBR dominated power systems. The initial step in implementing a Dynamic State Estimation (DSE) based protection system involves developing a high-fidelity model for the protection zone. This modeling process is divided into two main tasks. First, detailed mathematical models are constructed for each key component within the protection zone, including transmission lines, generators, transformers, and IBRs. An example IBR model is shown in Figure 2.5. These models are based on the physical characteristics of each component to ensure an accurate representation of their functionality and operational dynamics.

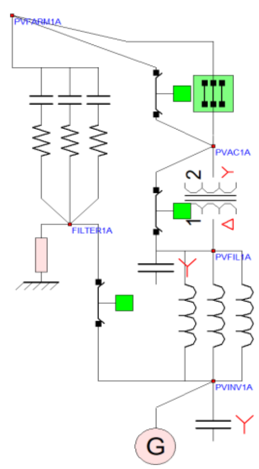

Figure 2.5: Inverter model developed in this project

Following this, the individual models are integrated to form a comprehensive network model that encapsulates the entire power system which includes all the protection zones. This aggregate model enables a holistic view of the system interactions and behaviors. To develop these individual device models, each physical circuit is meticulously described through mathematical equations. These are then cast in the State and Control Quadratized Device Model (SCQDM) format. The SCQDM model syntax is given below:

$$i(t) = Y_{eqx1}\mathbf{x}(t) + Y_{equ1}\mathbf{u}(t) + D_{eqxd1}\frac{d\mathbf{x}(t)}{dt} + C_{eqc1} \qquad (1)$$

$$0 = Y_{eqx2}\mathbf{x}(t) + Y_{equ2}\mathbf{u}(t) + D_{eqxd2}\frac{d\tilde{\mathbf{x}}(t)}{dt} + C_{eqc2} \qquad (2)$$

$$0 = Y_{eqx3}\mathbf{x}(t) + Y_{equ3}\mathbf{u}(t) + \begin{Bmatrix} \vdots \\ \mathbf{x}(t)^T\langle F^i_{eqxx3}\rangle\mathbf{x}(t) \\ \vdots \end{Bmatrix} + \begin{Bmatrix} \vdots \\ \mathbf{u}(t)^T\langle F^i_{equu3}\rangle\mathbf{u}(t) \\ \vdots \end{Bmatrix} + C_{eqc3} \qquad (3)$$

Where **x**(t) and *i*(t) represent the state variables and interface currents of the model, respectively, and *Y*, *D*, and *F* are coefficient matrices, with *C* being a constant vector. Equations that position interface currents on the left-hand side are termed interface current equations. Equations that are governed by physical laws and result in zero values on the left-hand side are identified as internal equations.

The protection zone may encompass multiple power devices, which necessitates the integration of these device models into a unified network-level model. Typically, a device model comprises three types of equations: (a) interface current equations at the boundary of the protection zone, (b) interface current equations at nodes shared by multiple devices, and (c) internal equations specific to each device. For equations of type (a) and (c), the states of individual devices are integrated into the overall network states. For type (b), all interface current equations related to a common node are aggregated, and Kirchhoff's Current Law (KCL) is applied to formulate a single equation for each node.

2.4 Measurement Model

Any physical quantity can be expressed in terms of an equation in terms of the state variables of the SCQDM model. We refer to this equation as the measurement model. The development of the measurement model follows first principles. This requires a detailed understanding of the types and locations of measurements, which are typically categorized as follows:

1. Actual Measurements: These are direct readings obtained from instrumentation within the system.
2. Derived Measurements: Calculated from one or more actual measurements.
3. Virtual Measurements: Represent constraints within the system, typically set as zeros in the equations of virtual linear and quadratic models.
4. Pseudo Measurements: these are estimated values for physical quantities that are not directly measured (e.g., neutral voltages, neutral currents, etc.). A high degree of uncertainty is also assigned for these measurements.

The inclusion of virtual and pseudo measurements enhances the system's observability and augments redundancy. Utilizing data from these measurements alongside the dynamic model of the protection zone, we construct a comprehensive network-level measurement model. For measurements taken across components, the model equation is formulated based on the corresponding states from the network-level model. For through measurements, it is derived from the current equations of the respective devices. The general formulation of the measurement model is expressed as follows:

$$\begin{aligned} z(t) &= Y_{zx}\mathbf{x}(t) + \left\{ \begin{array}{c} \vdots \\ \mathbf{x}^T \langle F^i_{zx} \rangle \mathbf{x} \\ \vdots \end{array} \right\} + D_{zx}\frac{dx(t)}{dt} + C_{zx} + \eta \\ &= \mathrm{h}(x) + \eta \end{aligned} \tag{4}$$

where **z**(t) is the measurement vector, **x**(t) is the network state vector, η is the noise introduced by the meter, Y_{zx}, D_{zx}, F_{zx} matrices are coefficient matrices and C_{zx} is the constant vector

There are two types of high-fidelity simulation methods to study electrical transients of the system, time-domain and frequency-domain analysis. Note that both time domain and frequency domain modeling and simulation is based on the SCQDM modeling of each component of the system.

For this study, we use time domain simulation to study temporary overvoltages. This is the most detailed representation of the system.

For this study, we also use frequency domain method to study the response of legacy protection systems in IBR dominated power systems. In frequency domain, we represent the inverters as well as the PV panels as a single equivalent voltage source with the appropriate parameters to mimic the behavior of the inverters. The value of the rms voltage for this voltage source is equivalent to the average voltage being produced by the PV panels during the day. In addition, it models the current limiting controllers of the inverter.

2.5 Summary

In this section, we have presented previous work done in modeling IBR during transient simulation analysis. There is a balance between having complicated models that require extensive simulation time as well as hardware resources and having a simplified model that still capture transient analysis. In this project, we aim to have a high-fidelity model with sufficient modeling of IBR resource to conduct transient analysis. This way, we conduct the analysis in sufficient time to capture the overvoltages allowing protection functions to operate successfully.

3. Description of the Example Test System

3.1 Requirements for Proper Dynamic Analysis of Test Systems

This section addresses the evaluation of the transient overvoltages in a IBR dominated power system by use of a high fidelity power system analysis and proper models of IBRs. The high-fidelity models guarantee that the analysis results are correct and conclusions can be reliably deducted from the results. The requirements for achieving a high-fidelity approach are from [17]:

a- Usability: The model should have enough control functions, able to run simulations at different time steps and time range, response to various power and voltage commands, and has enough documentation.

b- Efficiency: The model can run in reasonable time, reach steady state quickly, capable to run with advanced computing methods.

c- Accuracy: the model is accurate and able to be verified with clear components sizing, transformers are modeled with saturation, and protection functions are included.

3.2 Example Test System Description

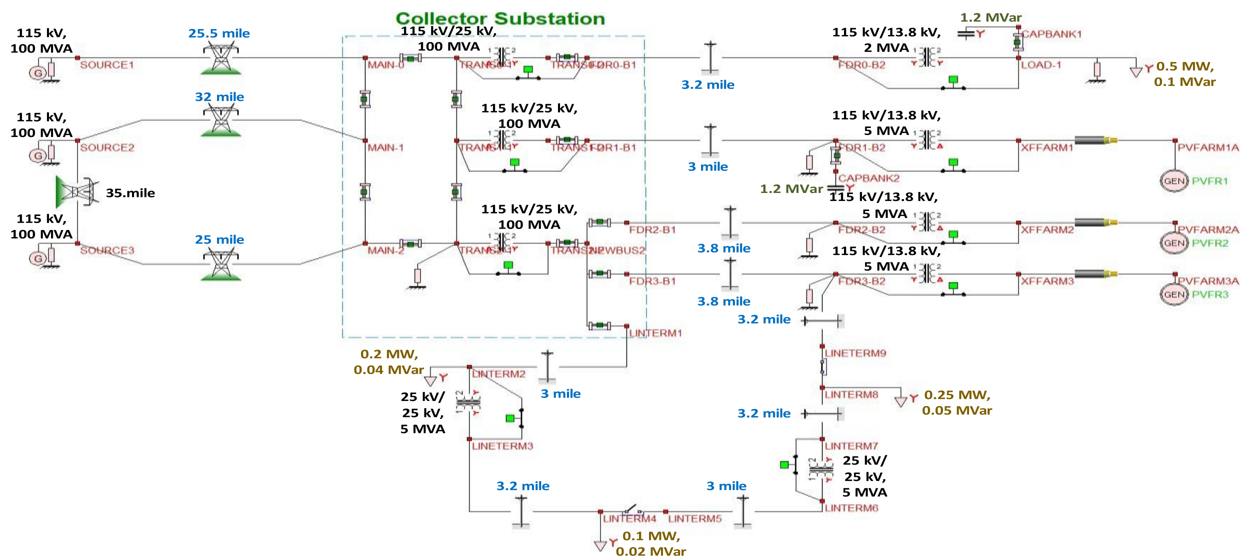

Figure 3.1: Test system under the study single line diagram

Figure 3.1 shows the single line diagram of a realistic system developed to simulate temporary over-voltage. The test system used in this study consists of three synchronous generators, a 115 kV transmission network connected to a collector substation 115kV/25 kV, a 25 kV distribution network with to various loads, and three PV farms. Table 3.1 presents the list of modelled levels along with detailed description.

Table 3.1 List of modelled system levels

Level	Description
Synchronous Generators	Three 25-30 MVA generators
Transmission Lines (115 kV)	Four 115 kV transmission lines connected to collector substation
Collector Substation (115 kV / 25 kV)	Three 115 kV/25 kV three-phase transformers with three loads connected
Distribution Lines (25 kV)	Five distribution lines including three lines connected to the PF farms via 13.4 kV lines
Distribution Lines (13.8 kV)	Connected to the 13.8 kV side of the step down transformers to PV farms 2 and 3
Loads	7 loads distributed across the system and they impact the overvoltage on PV farms module

We will explain in detail the levels of the system and how the models were developed.

3.2.1 25-30 MVA Equivalent Voltage Sources

There are three equivalent generating source models for the 115 kV Transmission system level. Figure 3.2 depicts the equivalent generating source number one showing the apparent power rating of 25.0 MVA. The other equivalent generating sources have 30.0 MVA and 25.0 MVA apparent power ratings, respectively. In addition, each source is placed with a different phase angle. All the generating sources have an angle of 90 degrees.

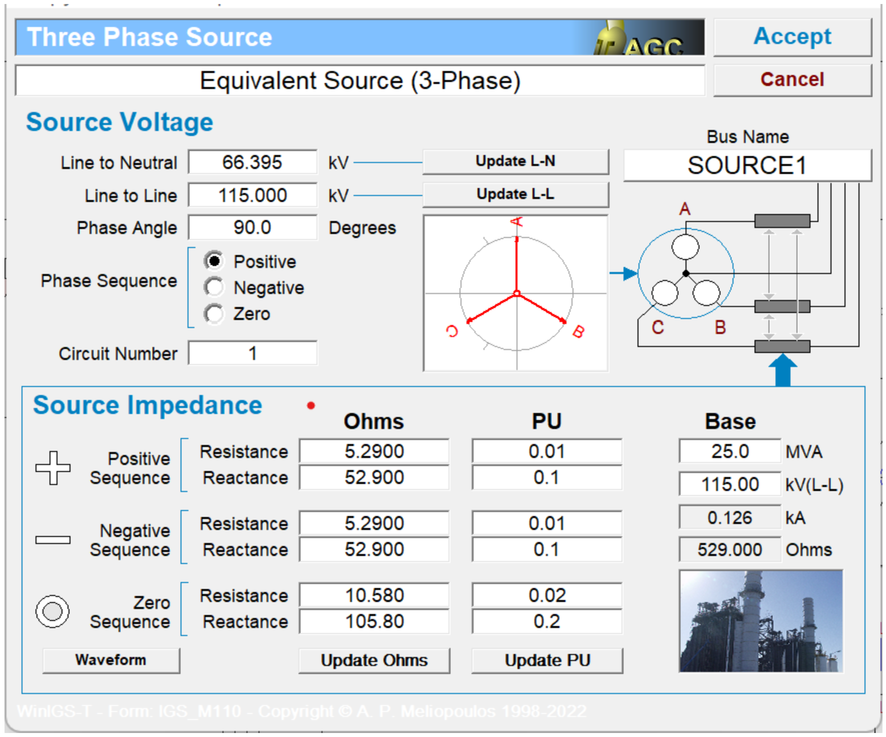

Figure 3.2: Equivalent source #1 for transmission lines

3.2.2 115 kV Transmission Lines Models

The transmission network consists of four circuits of 25.5-mile, 32-mile, 25-mile, and 35-mile transmission lines. Transmission lines are modeled using the 3-Phase Overhear Line model as depicted in Figure 3.3 for the 25.5-mile line. Other lines are modeled similarly with the exception of changing the line length.

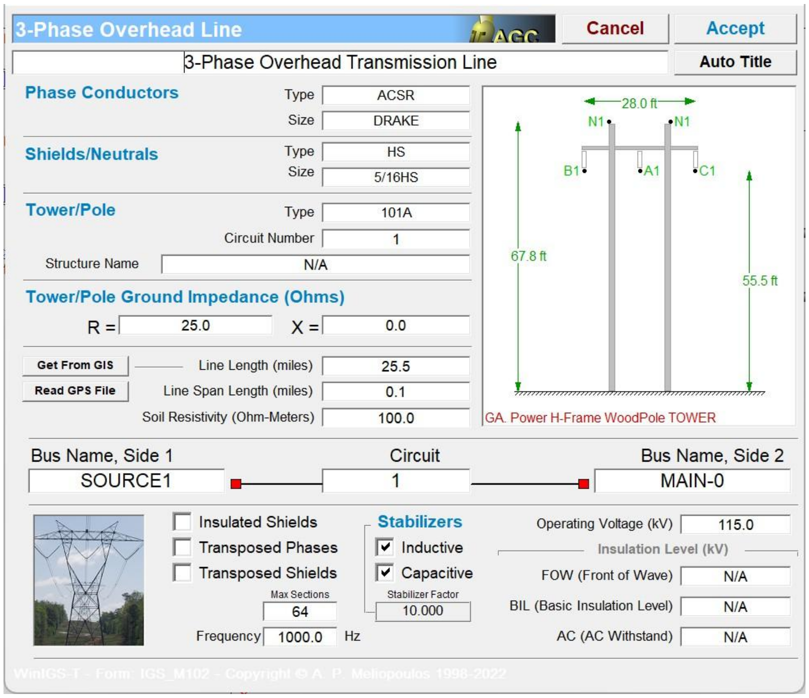

Figure 3.3: 3-phase overheard transmission line model

3.2.3 115 kV /25 kV Collector Substation Model

The 115 kV / 25 kV collector substation consists of 12 breakers, three 115 kV/ 25 kV step-down transformers rated at 100 MVA, and three loads. Figure 3.4 shows the model of the three-phase step-down transformers from 115 kV to 25 kV levels. The transformers are connected Delta at the high-side, and Wye at the low-side.

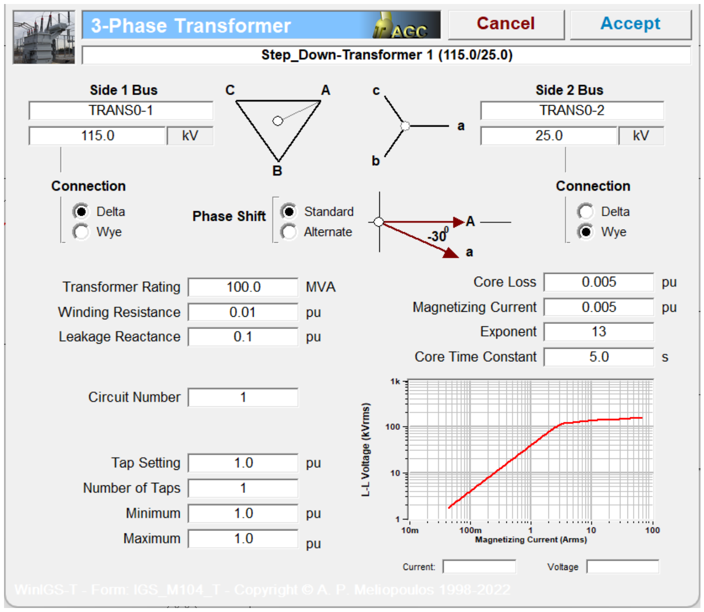

Figure 3.4: Model of the three-phase step-down transformer

3.2.4 25 kV Distribution Network

A five-feeder distribution system and three PV farms are connected to the system under study. The first feeder is connected to a 25 kV / 25 kV regulator which is connected to a load and a capacitor bank. Feeders 2 is connected to the 25 kV PV farm 1. Feeders 3 and 4 are connected to the 25 kV to 13.8 kV step-down transformers which is connected to the PV farms 2 and 3. Feeder 5 is forming a ring connection that connects with feeder 4 at the high-side of the 25 kV / 13.8 kV step down transformer. The purpose of this ring connection is to create good operational flexibility and high reliability, where any of the circuit breakers can be opened and isolated for maintenance without interruption of service. This makes the system more realistic where opening the breakers will change the nature of the distribution system. The behavior of this system exhibits similar behavior to systems that have high IBR penetration due to this connection. Figure 3.5 shows the model used to model the feeder using 3-phase overhead line. In this case, feeder 1 has a length of 3.2 miles.

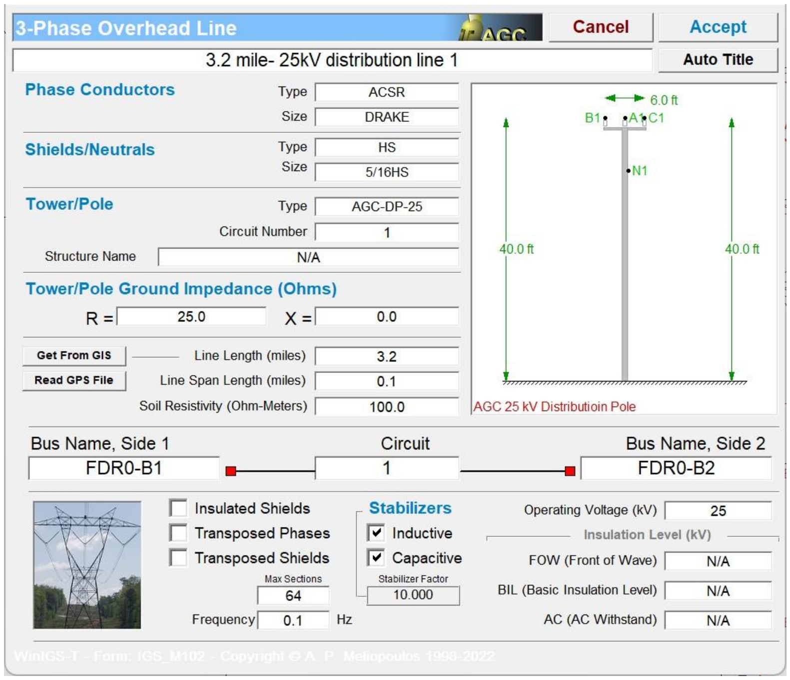

Figure 3.5: Modeling of the 25 kV feeder distribution line

3.2.5 PV Farms

Each PV module comprises an inverter and filters where part of the filters remains on-line when a PV module is temporarily disconnected during the study. This action leaves substantial capacitive load in the system, when the PV module is disconnected. Table 3.2 shows the details of PV farms 1, 2, and 3. In addition, it shows the value of harmonic filters used, series and shunt filters, as well as the harmonic banks. The purpose of the harmonic filters is to smooth and remove the harmonics from the voltage signals generated after the inverters.

Table 3.2: Details of PV farms and harmonic filters

Level	Description
PV Farm 1 (25 kV / 480 VDC)	Total capacity of 12 MWp with 12 modules 1 MWp each
PV Farm 2 (13.8 kV / 480 VDC)	Total capacity of 6 MWp with 12 modules 0.5 MWp each
PV Farm 3 (13.8 kV / 480 VDC)	Total capacity of 6 MWp with 12 modules 0.5 MWp each
Harmonic Filters	Modeled with R = 0.02 Ohms, X = -7,000 Ohms (C = 0.379 nF) per phase connected to the high-side line
Series L Filters	Modeled with R = 0.00 Ohms, X = 0.1 Ohms (L = 0.265 mH) per phase connected to the low-side of transformer
Shunt C Filters	Modeled with R = 0.00 Ohms, X=-0.05424 (C = 143.9 uF) per phase connected to the low-side of transformer
Capacitor Banks	Modeled with R = 0.00 Ohms, X=-0.05424 (C = 143.9 uF) per phase connected to the generator model of the PV

Figure 3.6 present the single line diagram for PV farm 1 which consists of 12 PV modules rated at 1 MWp. Thus, the total peak capacity of PV farm 1 is 12 MWp. Each module consists of a 480 V / 25 kV step-up transformer from the inverter to the feeder as depicted in Figure 3.7 where Delta connection is at the low-voltage side. The PV and the inverter are modelled as a three-phase voltage source, as depicted in Figure 3.8, with apparent power rated at 1 MVA and line-to-line voltage of 480 V with 30 degrees phase shift. The harmonic filter model is illustrated in Figure 3.9 with values available. Similar models are developed for the series reactor, shunt capacitor, and the grounding.

In addition, there are 12 Merging Units (MU) for data acquisitions at each module. Figure 3.10 shows the device settings for the MU used for data acquisition. Figure 3.11 shows the list of instrumentation channels used for data acquisition including the settings for the Current Transformers (CTs) and Potential Transformers (PTs). Similarly, Figure 3.12 shows the list of measurement channels that are mathematically calculated from the instrumentation channels for further data analysis. For example, the neutral current at some devices cannot be measured, instead it can be calculated by summing the measurement of the three phases of the measured currents.

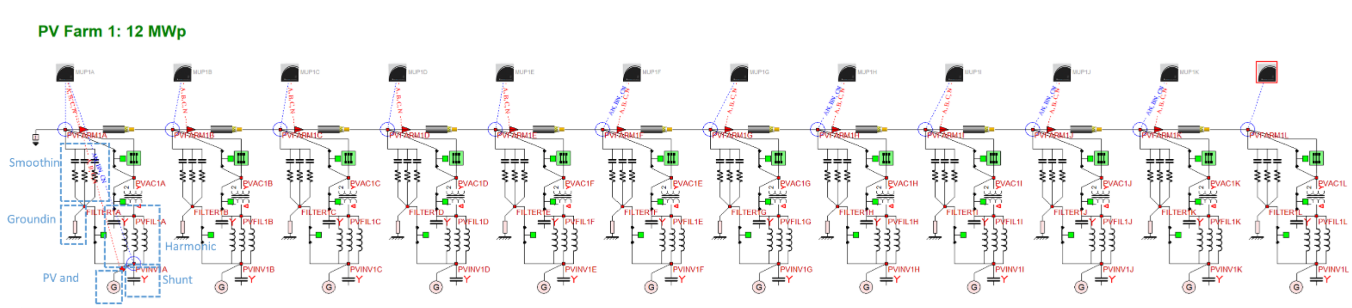

Figure 3.6: Single line diagram of PV farm 1

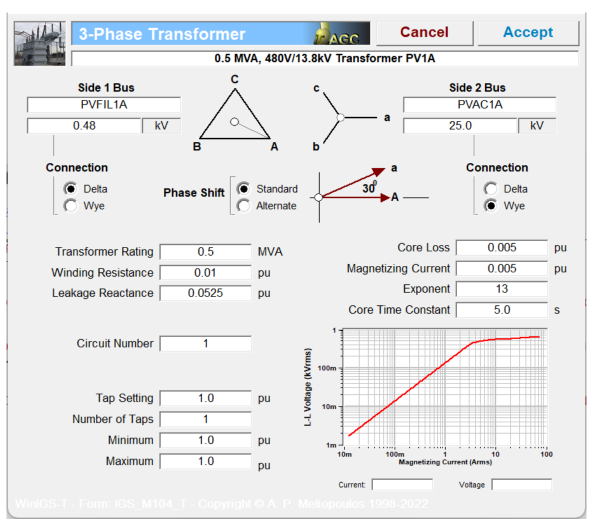

Figure 3.7: Inverter step-up transformer 3-phase module

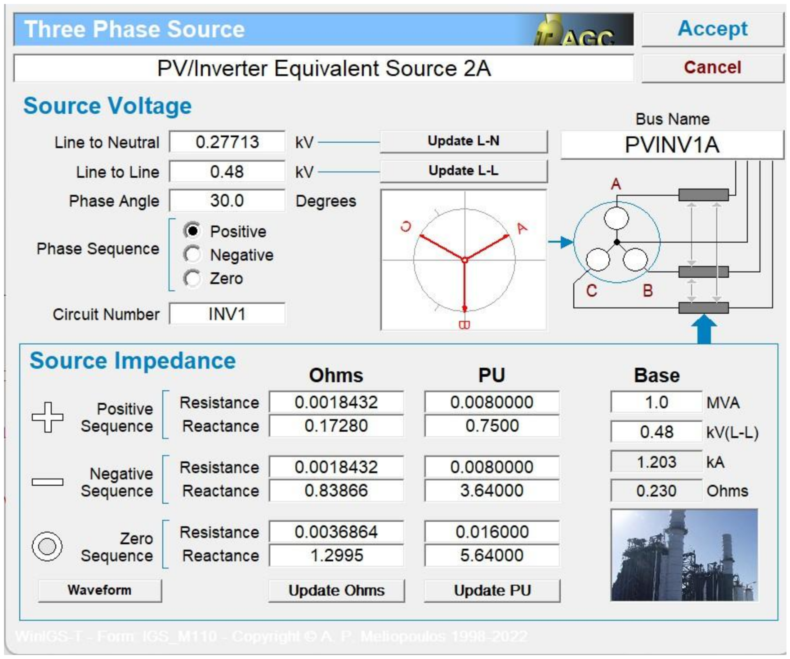

Figure 3.8: Three-phase source for PV and inverter equivalent

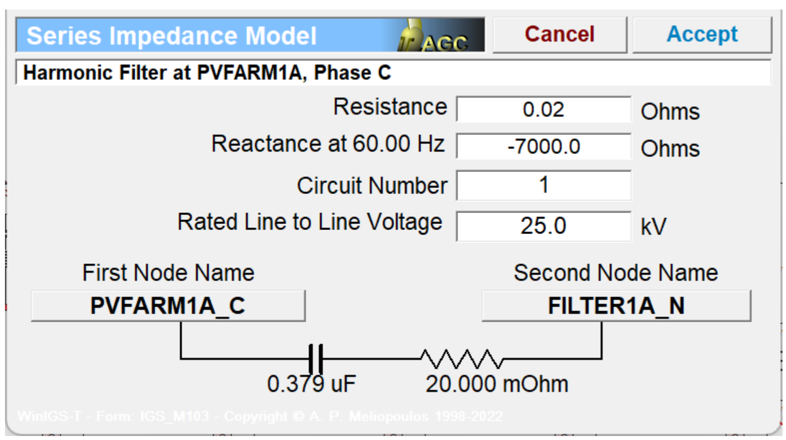

Figure 3.9: Harmonic filter model for PV farm 1 module 1

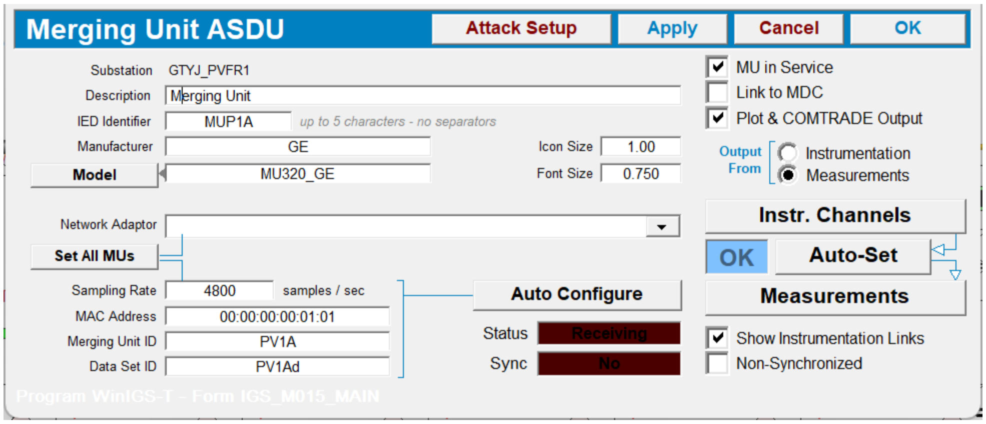

Figure 3.10: Merging Unit device settings

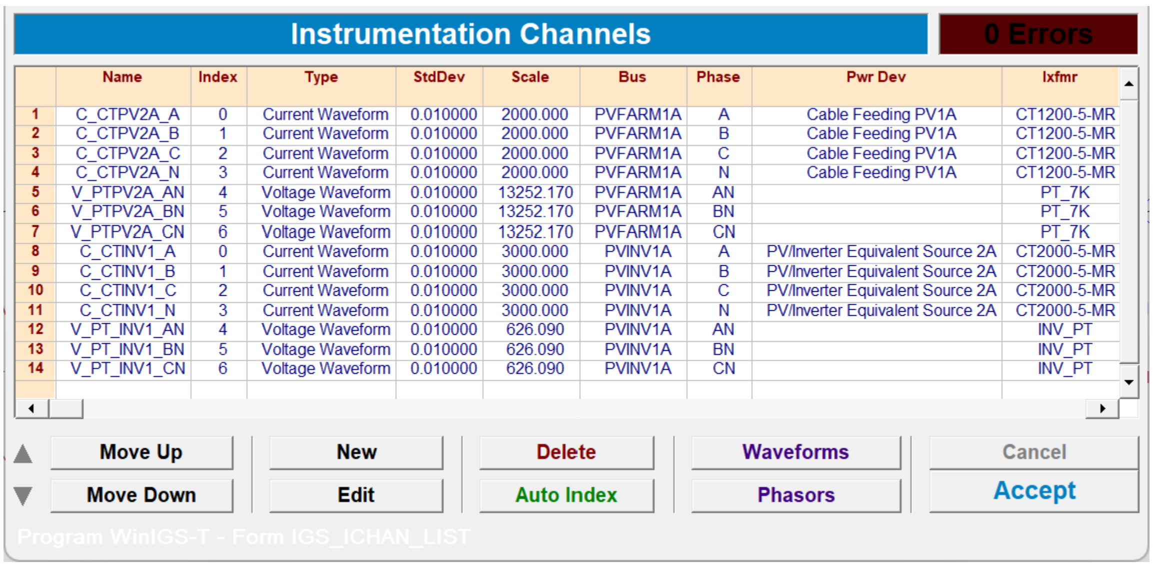

	Name	Index	Type	StdDev	Scale	Bus	Phase	Pwr Dev	Ixfmr
1	C_CTPV2A_A	0	Current Waveform	0.010000	2000.000	PVFARM1A	A	Cable Feeding PV1A	CT1200-5-MR
2	C_CTPV2A_B	1	Current Waveform	0.010000	2000.000	PVFARM1A	B	Cable Feeding PV1A	CT1200-5-MR
3	C_CTPV2A_C	2	Current Waveform	0.010000	2000.000	PVFARM1A	C	Cable Feeding PV1A	CT1200-5-MR
4	C_CTPV2A_N	3	Current Waveform	0.010000	2000.000	PVFARM1A	N	Cable Feeding PV1A	CT1200-5-MR
5	V_PTPV2A_AN	4	Voltage Waveform	0.010000	13252.170	PVFARM1A	AN		PT_7K
6	V_PTPV2A_BN	5	Voltage Waveform	0.010000	13252.170	PVFARM1A	BN		PT_7K
7	V_PTPV2A_CN	6	Voltage Waveform	0.010000	13252.170	PVFARM1A	CN		PT_7K
8	C_CTINV1_A	0	Current Waveform	0.010000	3000.000	PVINV1A	A	PV/Inverter Equivalent Source 2A	CT2000-5-MR
9	C_CTINV1_B	1	Current Waveform	0.010000	3000.000	PVINV1A	B	PV/Inverter Equivalent Source 2A	CT2000-5-MR
10	C_CTINV1_C	2	Current Waveform	0.010000	3000.000	PVINV1A	C	PV/Inverter Equivalent Source 2A	CT2000-5-MR
11	C_CTINV1_N	3	Current Waveform	0.010000	3000.000	PVINV1A	N	PV/Inverter Equivalent Source 2A	CT2000-5-MR
12	V_PT_INV1_AN	4	Voltage Waveform	0.010000	626.090	PVINV1A	AN		INV_PT
13	V_PT_INV1_BN	5	Voltage Waveform	0.010000	626.090	PVINV1A	BN		INV_PT
14	V_PT_INV1_CN	6	Voltage Waveform	0.010000	626.090	PVINV1A	CN		INV_PT

Figure 3.11: List of instrumentation channels for PV module 1 in PV farm

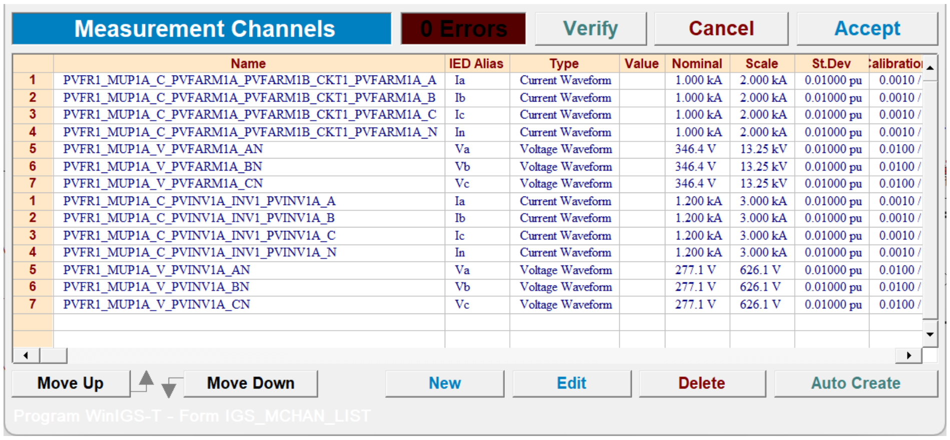

Measurement Channels | 0 Errors | Verify | Cancel | Accept

	Name	IED Alias	Type	Value	Nominal	Scale	St.Dev	:alibratio
1	PVFR1_MUP1A_C_PVFARM1A_PVFARM1B_CKT1_PVFARM1A_A	Ia	Current Waveform		1.000 kA	2.000 kA	0.01000 pu	0.0010 /
2	PVFR1_MUP1A_C_PVFARM1A_PVFARM1B_CKT1_PVFARM1A_B	Ib	Current Waveform		1.000 kA	2.000 kA	0.01000 pu	0.0010 /
3	PVFR1_MUP1A_C_PVFARM1A_PVFARM1B_CKT1_PVFARM1A_C	Ic	Current Waveform		1.000 kA	2.000 kA	0.01000 pu	0.0010 /
4	PVFR1_MUP1A_C_PVFARM1A_PVFARM1B_CKT1_PVFARM1A_N	In	Current Waveform		1.000 kA	2.000 kA	0.01000 pu	0.0010 /
5	PVFR1_MUP1A_V_PVFARM1A_AN	Va	Voltage Waveform		346.4 V	13.25 kV	0.01000 pu	0.0100 /
6	PVFR1_MUP1A_V_PVFARM1A_BN	Vb	Voltage Waveform		346.4 V	13.25 kV	0.01000 pu	0.0100 /
7	PVFR1_MUP1A_V_PVFARM1A_CN	Vc	Voltage Waveform		346.4 V	13.25 kV	0.01000 pu	0.0100 /
1	PVFR1_MUP1A_C_PVINV1A_INV1_PVINV1A_A	Ia	Current Waveform		1.200 kA	3.000 kA	0.01000 pu	0.0010 /
2	PVFR1_MUP1A_C_PVINV1A_INV1_PVINV1A_B	Ib	Current Waveform		1.200 kA	3.000 kA	0.01000 pu	0.0010 /
3	PVFR1_MUP1A_C_PVINV1A_INV1_PVINV1A_C	Ic	Current Waveform		1.200 kA	3.000 kA	0.01000 pu	0.0010 /
4	PVFR1_MUP1A_C_PVINV1A_INV1_PVINV1A_N	In	Current Waveform		1.200 kA	3.000 kA	0.01000 pu	0.0010 /
5	PVFR1_MUP1A_V_PVINV1A_AN	Va	Voltage Waveform		277.1 V	626.1 V	0.01000 pu	0.0100 /
6	PVFR1_MUP1A_V_PVINV1A_BN	Vb	Voltage Waveform		277.1 V	626.1 V	0.01000 pu	0.0100 /
7	PVFR1_MUP1A_V_PVINV1A_CN	Vc	Voltage Waveform		277.1 V	626.1 V	0.01000 pu	0.0100 /

Move Up | Move Down | New | Edit | Delete | Auto Create

Program WinIGS-T - Form IGS_MCHAN_LIST

Figure 3.12: List of measurement channels for PV module 1 at PV farm 1

Similar to PV farm 1, PV farms 2 and 3 are identical except the values used. This includes voltage levels (13.8 kV instead of 25 kV) and the rated power of each module (0.5 MWp). The values of the harmonic filters are also different. Figure 3.13 and Figure 3.14 show the single line diagrams for PV farms 2 and 3.

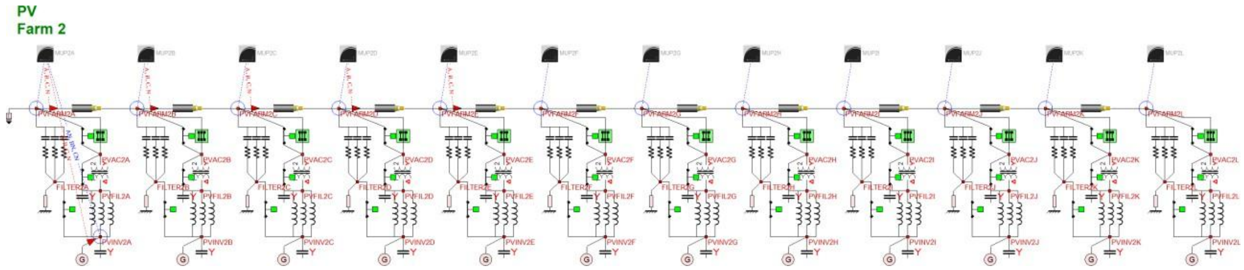

Figure 3.13: Single line diagram for PV farm 2

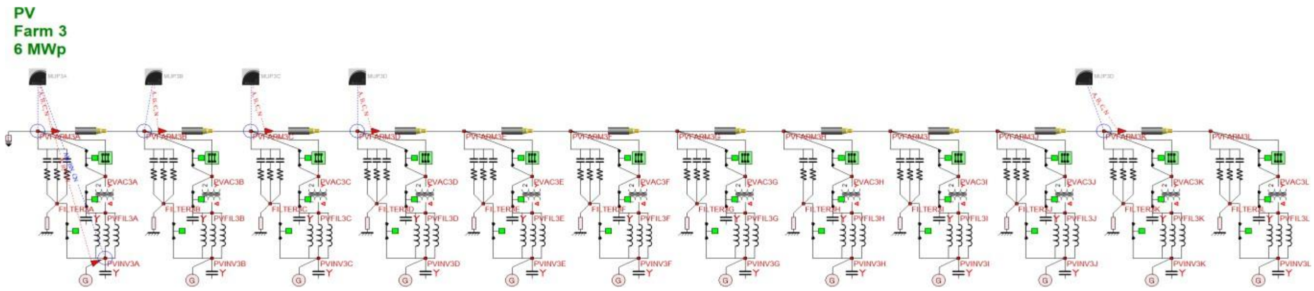

Figure 3.14: Single line diagram for PV farm 3

4. Parametric Study to Quantify the Impact of Parameters on Temporary Overvoltages

The goal of this section is to identify the parameters impacting temporary overvoltage in IBR-dominated power systems. It starts by identifying such parameters including the variations of each parameter. Then it presents selected events to simulate the changes on a realistic power system developed in the previous sections.

4.1 Parameters that Impact Temporary Overvoltages

Parameters affecting the temporary overvoltages in IBR-dominated networks can vary depending on the voltage levels and the layout of the grid. However, there are parameters that can influence the level of temporary overvoltage in IBR-dominated networks when the IBRs are disconnected from the grid. Below are the parameters that impact the overvoltage:

1- Size of the PV farms: is the primary factor in determining the levels of temporary overvoltage.
   There are two metrics that can define the size of the PV farm:
   - Number PV farms in the system: in this case study, there are three PV farms connected to different voltage levels, i.e. 25 kV and 13.8 kV.
   - Size of each PV farm module: this is an important parameter as having larger units will make the impact larger. In PV farm 1, the size of each unit is 1 MWp while PV farms 2 and 3 have modules of size 0.5 MWp.
   - Number of PV units per farm: every farm has a fixed number of modules where in this study we have decided to have 12 units per farm.
   - Location of PV farms: this factor is related to where the PV farms are placed. An overvoltage impact will be larger when the location of the farm is far away from the loads.

2- Connected Transformers: the parameters of connected transformers to the PV farms can influence the peak levels of overvoltages. Such parameters include:
   - Type of transformer connection: either Delta or Wye.
   - Grounding of the transformer: solidly grounded or impedance grounding.

3- Loading conditions:
   - Location of the load: for example, high-side of transformer or low-side.
   - Size of the real and reactive power of the load: we can expect different response for purely resistive loads compared to reactive or capacitive loads.

4- Grounding conditions:
   - Level of grounding impedance:
     - Low grounding impedance: below 1 Ohm.
     - High grounding impedance: up to 10 Ohms.

4.1.1 Selected events for the parametric study

There are hundreds of events that can be tested to study the impact on the peak of temporary overvoltages. However, such an approach can be impractical since transients' simulation analysis take long time to complete with sufficient accuracy. In any case, we studied many events and we finally decided to include the detailed results of the simulations for four events. Table 4.1 presents the selected events that were simulated to study the impact on transient temporary overvoltages in IBR-dominated network. The variations are made one at a time by changing up to two parameters to avoid duplicated results.

Table 4.1: Selected events for parametric case study

Event	Description
EVENT00	Base-case (System as developed with diverse PV farms and standard connections).
EVENT01	PV Farm 1 XRFM is Delta-connected, PV Farm 2 XRFM is Y-connected , PV Farm 3 XRFM is Y-connected.
EVENT02	PV 1 Farm's load is connected to the high side of XRFM, PV 3 Farm's load is connected to the high side of XRFM.
EVENT03	Low impedance ground for all farms (0.5 ohms).
EVENT04	All PV Farms are Delta-connected to XRFMs, and loads are moved to high-side for PV Farms 1 and 3.

4.2 Transient Simulation Results for the Selected Events

This section presents the transient simulation results for the selected 4 events. It provides the simulation results for the three PV farms including high and low-voltage level side. In addition, it provides analysis results by the application of the changes for the selected parameters.

4.2.1 EVENT00 (Base-Case)

This event reflects the system developed initially with diverse PV farms and standard connections. The simulation results indicated that there is not overvoltage at the high voltage side except a small spike as depicted in Figure 4.1. For the low voltage side, Figure 4.2 shows that there is a of 77.3% with a peak of 694.9 V.

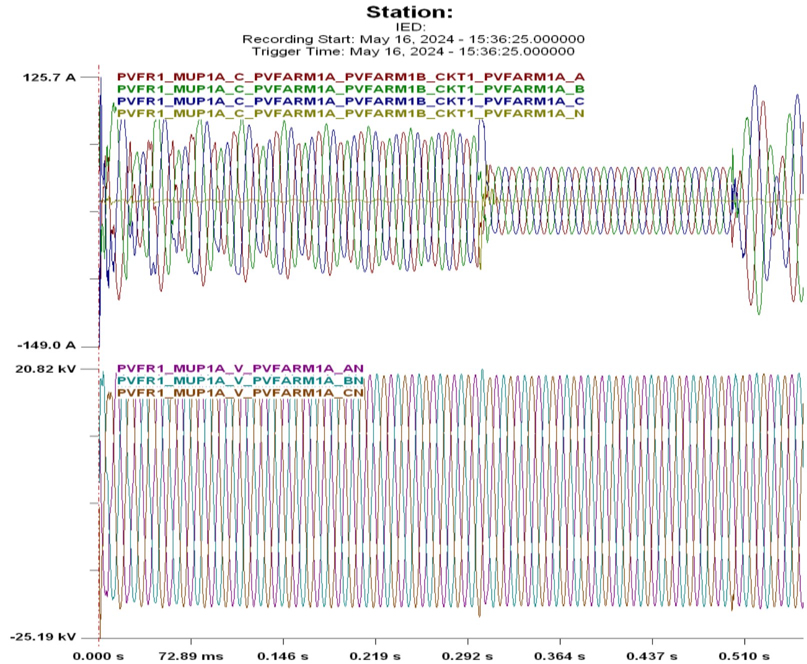

Figure 4.1: Transient current and voltage waveforms for PV farm 1 – module 1, 25 kV side (EVENT00)

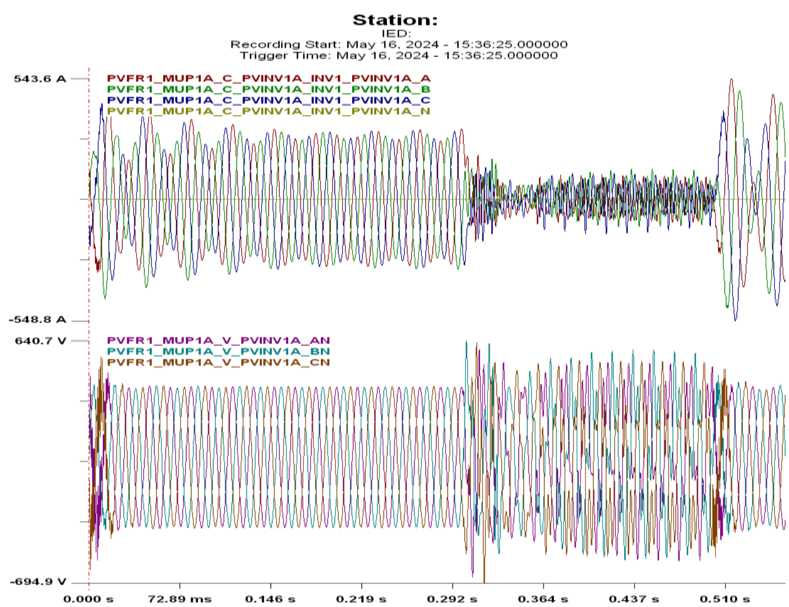

Figure 4.2: Transient current and voltage waveforms for PV farm 1 – module 1, 480 V side (EVENT00)

For PV farm 2, there is an overvoltage of 50.52% for the high-side with peak voltage of 16,960 V as indicated in Figure 4.3. For the low-side, there is an 81.77% with peak overvoltage of 712.4 V as shown in Figure 4.4.

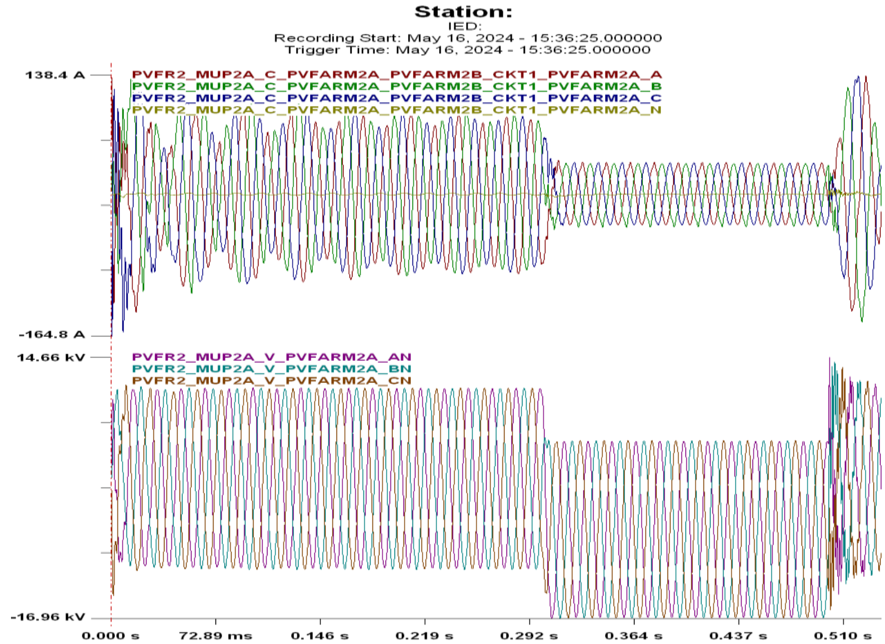

Figure 4.3: Transient current and voltage waveforms for PV farm 2 – module 1, 13.8 kV side (EVENT00)

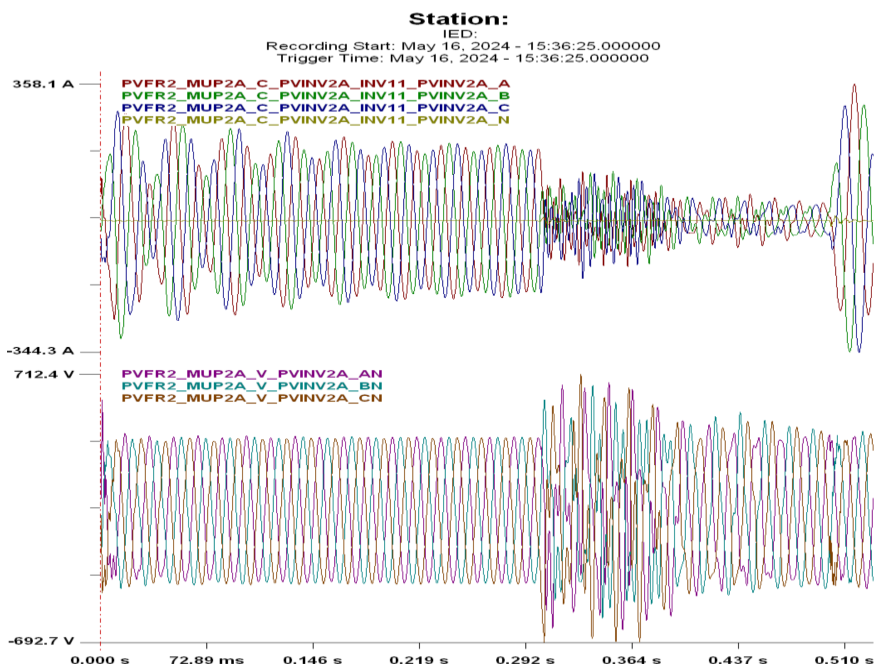

Figure 4.4: Transient current and voltage waveforms for PV farm 2 – module 1, 480 V side (EVENT00)

For PV farm 3, there is an overvoltage of 21.23% for the high-side with peak voltage of 13,660 V as indicated in Figure 4.5. For the low-side, there is an 85.47% with peak overvoltage of 726.9 V as shown in Figure 4.6.

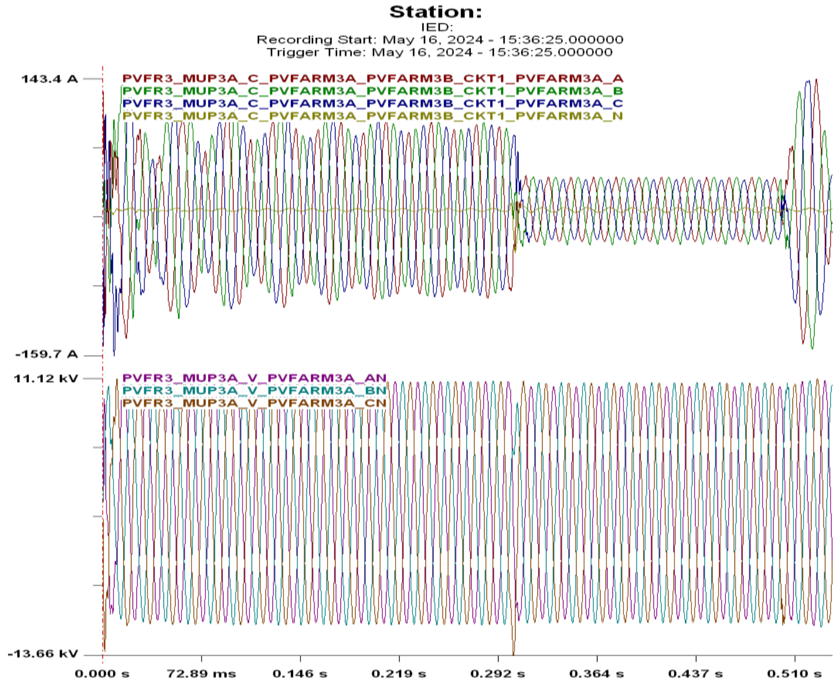

Figure 4.5: Transient current and voltage waveforms for PV farm 3 – module 1, 13.8 kV side (EVENT00)

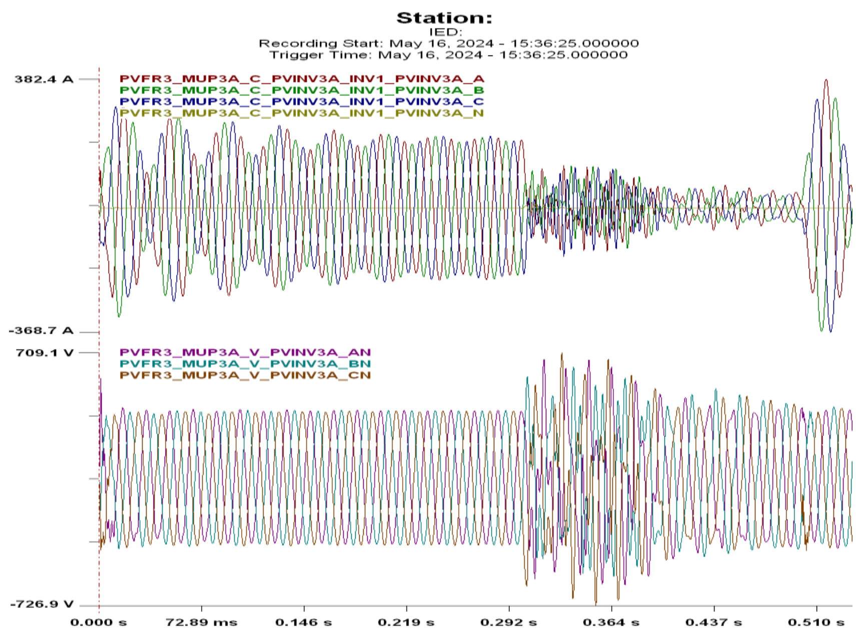

Figure 4.6: Transient current and voltage waveforms for PV farm 3 – module 1, 480 V side (EVENT00)

4.2.2 EVENT01

For EVENT01, we explore the change in temporary overvoltage when transformers connections is changed. PV Farm 1 XRFM is Delta-connected, PV Farm 2 XRFM is Y-connected, PV Farm 3 XRFM is Y-connected. The simulation results indicated that there is not overvoltage at the high voltage side except a small dip as depicted in Figure 4.7. For the low voltage side, Figure 4.8 shows that there is a of 64.21% with a peak of 643.6V.

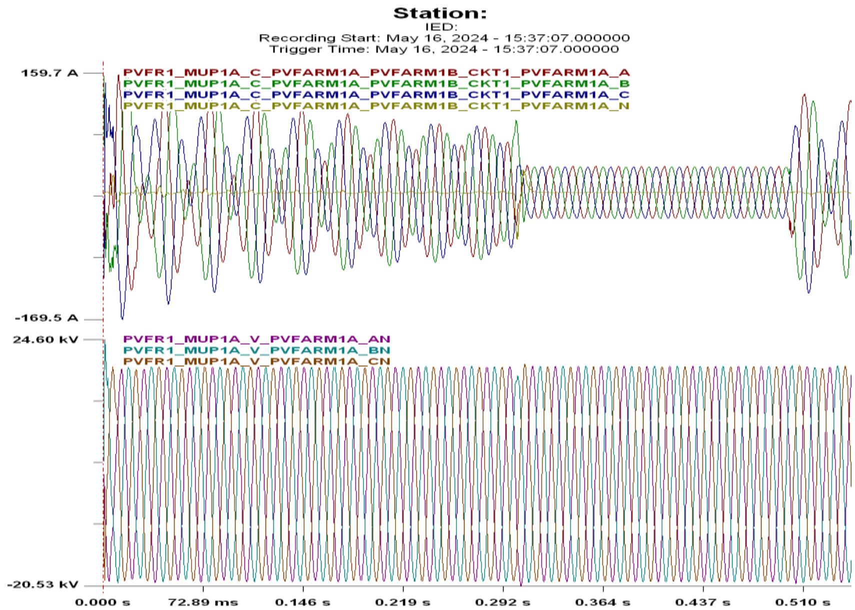

Figure 4.7: Transient current and voltage waveforms for PV farm 1 – module 1, 25 kV side (EVENT01)

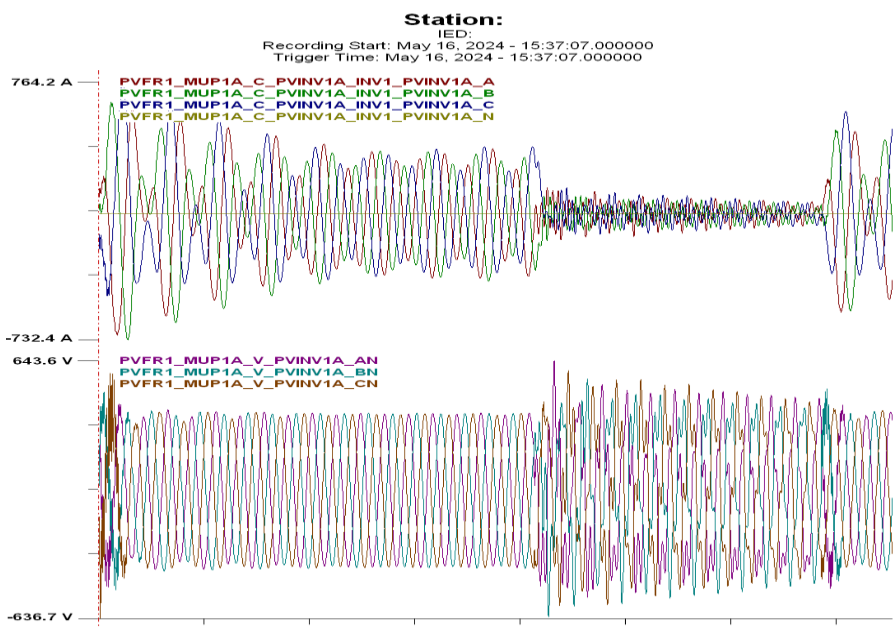

Figure 4.8: Transient current and voltage waveforms for PV farm 1 – module 1, 480 V side (EVENT01)

For PV farm 2, there is an no overvoltage for the high-side as presented in Figure 4.9. For the low-side, there is an 41.51% with peak overvoltage of 554.6 V as shown in Figure 4.10.

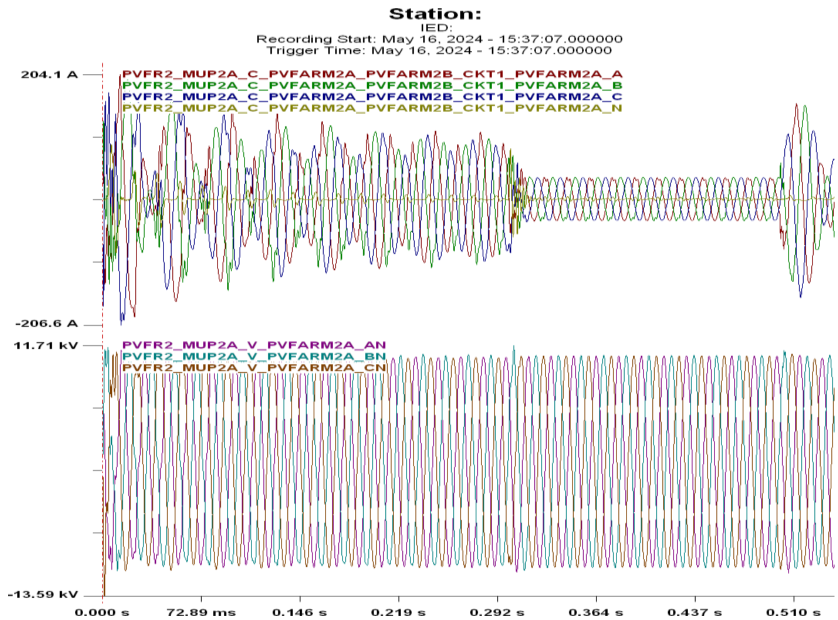

Figure 4.9: Transient current and voltage waveforms for PV farm 2 – module 1, 13.8 kV side (EVENT01)

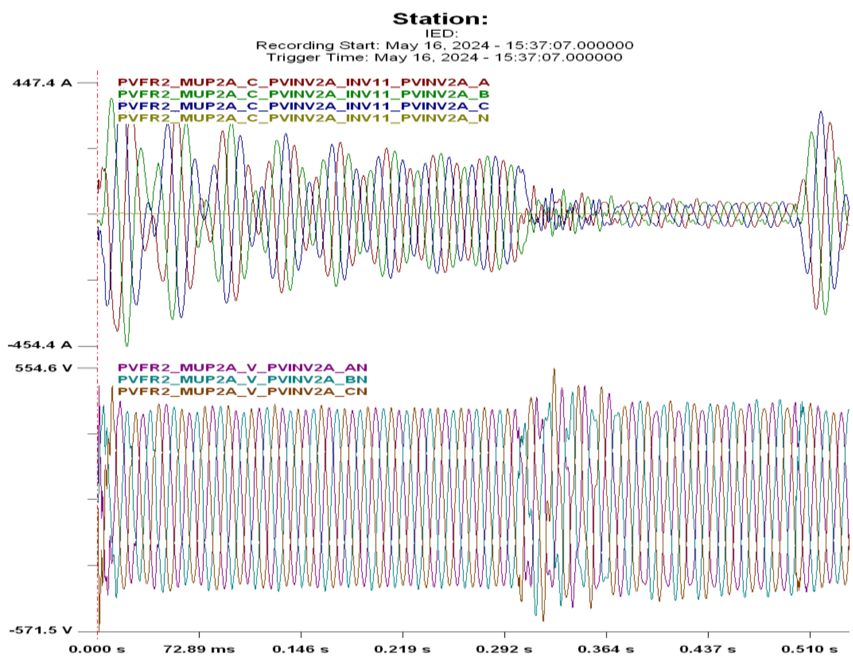

Figure 4.10: Transient current and voltage waveforms for PV farm 2 – module 1, 480 V side (EVENT01)

For PV farm 3, there is no overvoltage for the high-side as indicated in Figure 4.11. For the low-side, there is an 44.72% with peak overvoltage of 567.2 V as shown in Figure 4.12.

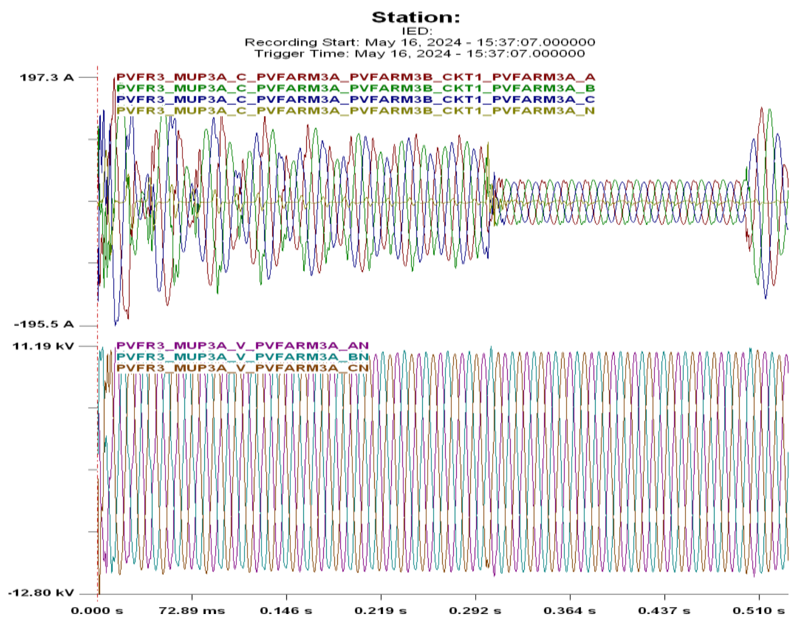

Figure 4.11: Transient current and voltage waveforms for PV farm 3 – module 1, 13.8 kV side (EVENT01)

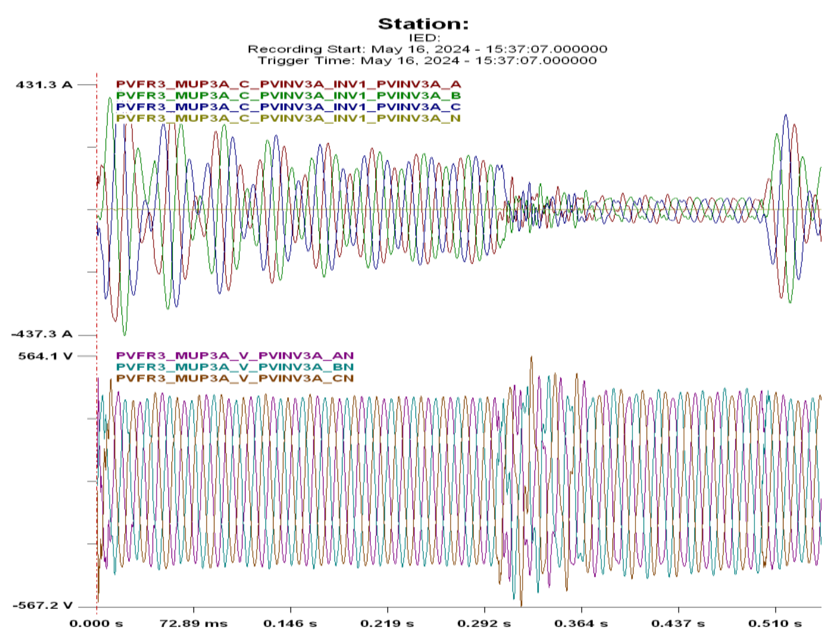

Figure 4.12: Transient current and voltage waveforms for PV farm 3 – module 1, 480 V side (EVENT01)

4.2.3 Remedial Actions EVENT01_RA00

Table 4.2: Remedial Actions for EVENT01_RA00

Item	Description
Event	PV Farm 1 XRFM is Delta-connected, PV Farm 2 XRFM is Y-connected, PV Farm 3 XRFM is Y-connected
RA	EVENT01_RA00: For XRFMs connected to PV Farm 2 and 3, change the high-side to Delta-connected
Simulation Results	Results of EVENT01_RA01 are shown in Figure 4.13 - Figure 4.18: PV Farm 1 • Reduction of high-side overvoltage spike. • Overvoltage at the low-side reduced by 7 volts. PV Farm 2 • No change in the overvoltage at the high-side. • Increase in low-side overvoltage. PV Farm 3 • No change in the overvoltage at the high-side. • Increase in low-side overvoltage. We were able to relieve PV Farm 1 but not PV Farms 2 and 3. This is due to the original connection not being optimized.

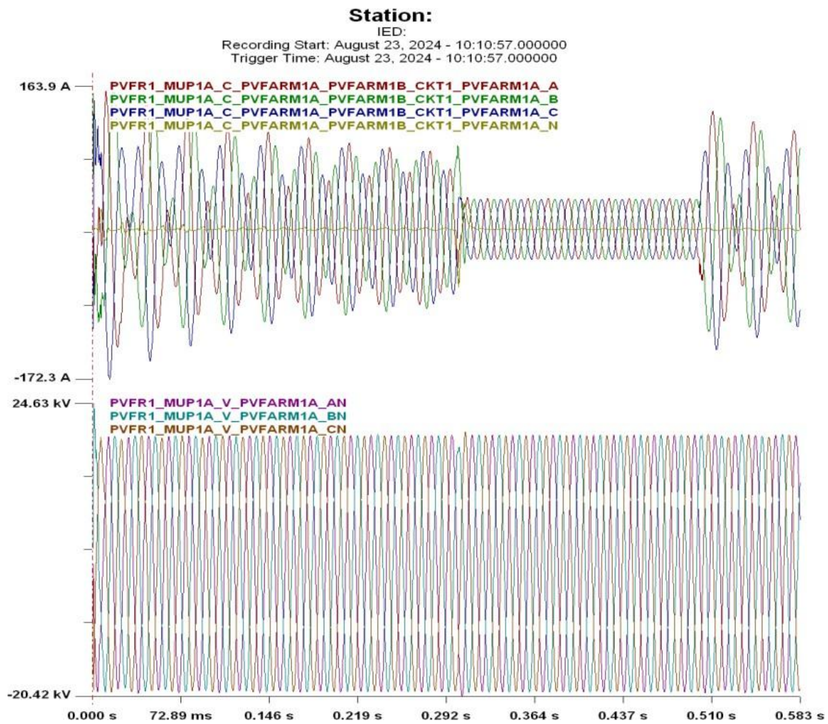

Figure 4.13: Transient current and voltage waveforms for PV farm 1 – module 1, 25 kV side (EVENT01_RA00)

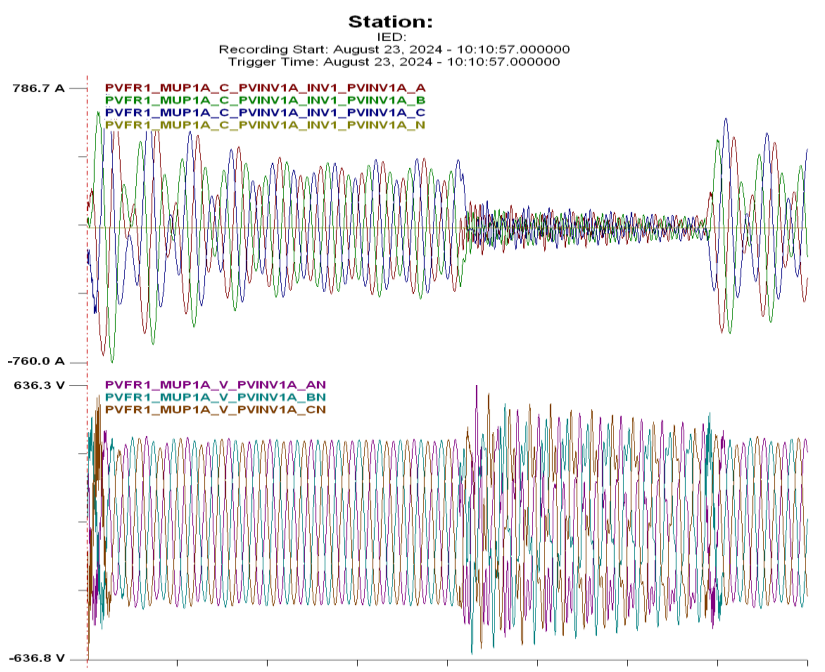

Figure 4.14: Transient current and voltage waveforms for PV farm 1 – module 1, 480 V side (EVENT01_RA00)

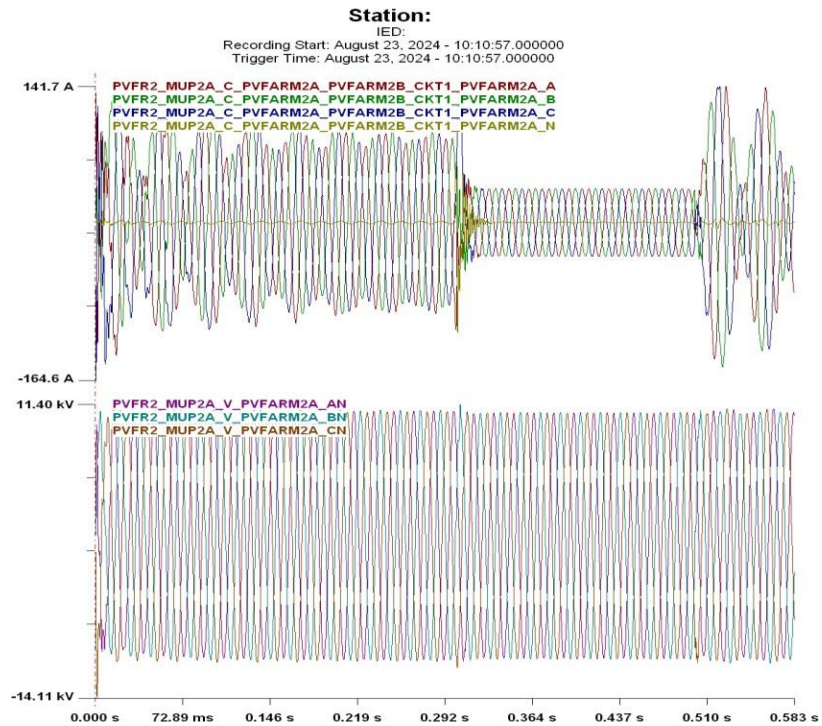

Figure 4.15: Transient current and voltage waveforms for PV farm 2 – module 1, 13.8 kV side (EVENT01_RA00)

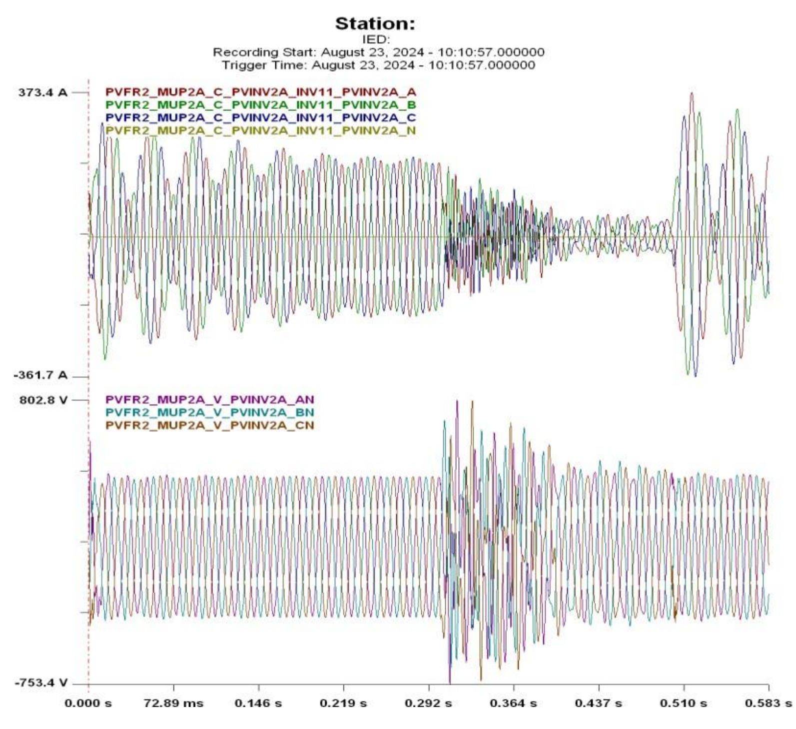

Figure 4.16: Transient current and voltage waveforms for PV farm 2 – module 1, 480 V side (EVENT01_RA00)

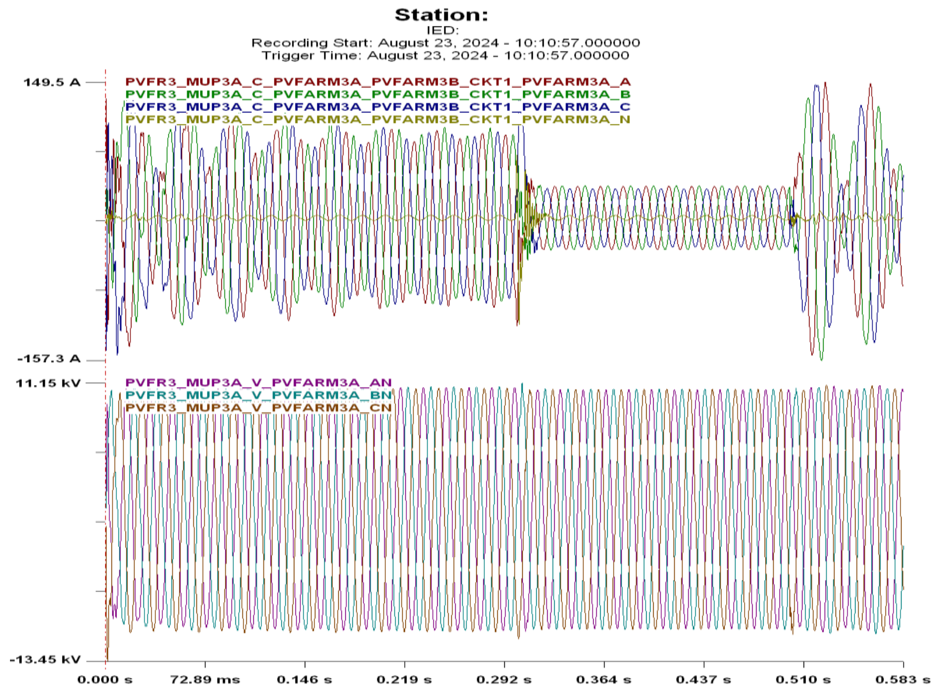

Figure 4.17: Transient current and voltage waveforms for PV farm 3 – module 1, 13.8 kV side (EVENT01_RA00)

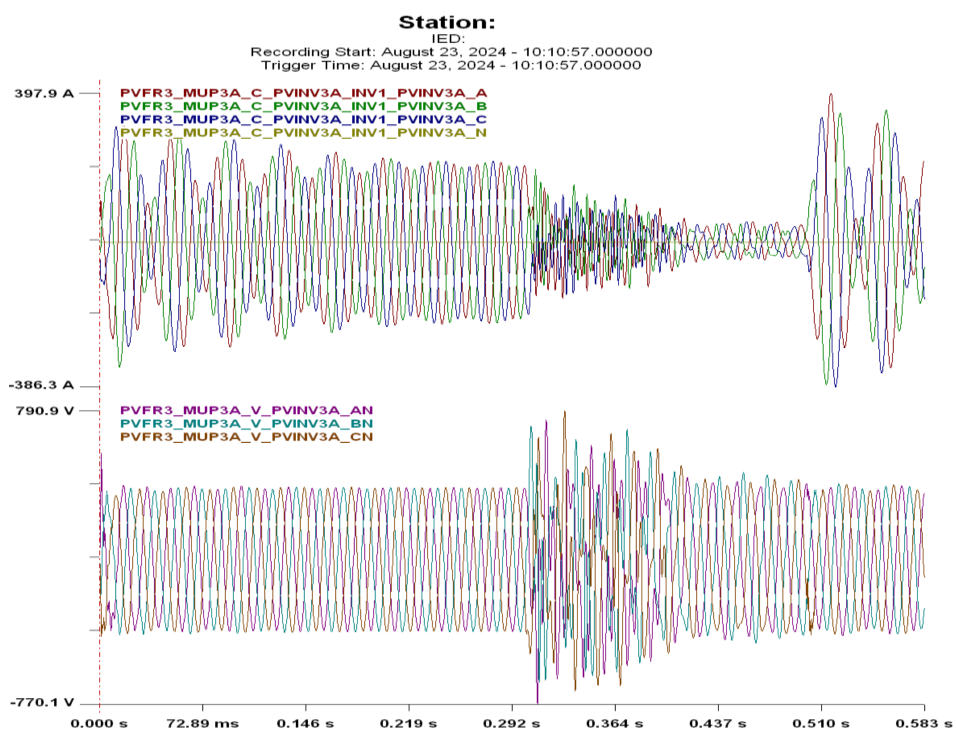

Figure 4.18: Transient current and voltage waveforms for PV farm 3 – module 1, 480 V side (EVENT01_RA00)

4.2.4 EVENT02

For EVENT02, we explore the change in temporary overvoltage when load connections is changed. PV 1 Farm's load is connected to the high side of XRFM, PV 3 Farm's load is connected to the high side of XRFM. Figure 4.19 through Figure 4.24 show the simulation results for EVENT02 at various PV farm locations.

The summary of the results for EVENT02 is provided below:

PV Farm 1

- No overvoltage at the high-side.
- Overvoltage at the low-side of 107.59% with a

peak of 813.6 V. PV Farm 2

- Overvoltage of 106.43% for the high-side with peak overvoltage of 23,260 V.
- Overvoltage of 113.94% for the low-side with peak

overvoltage of 838.5 V. PV Farm 3

- Overvoltage of 70.84% for the high-side with peak overvoltage of 19,250 V.
- Overvoltage of 114.97% for the low-side with peak overvoltage of 842.5 V.

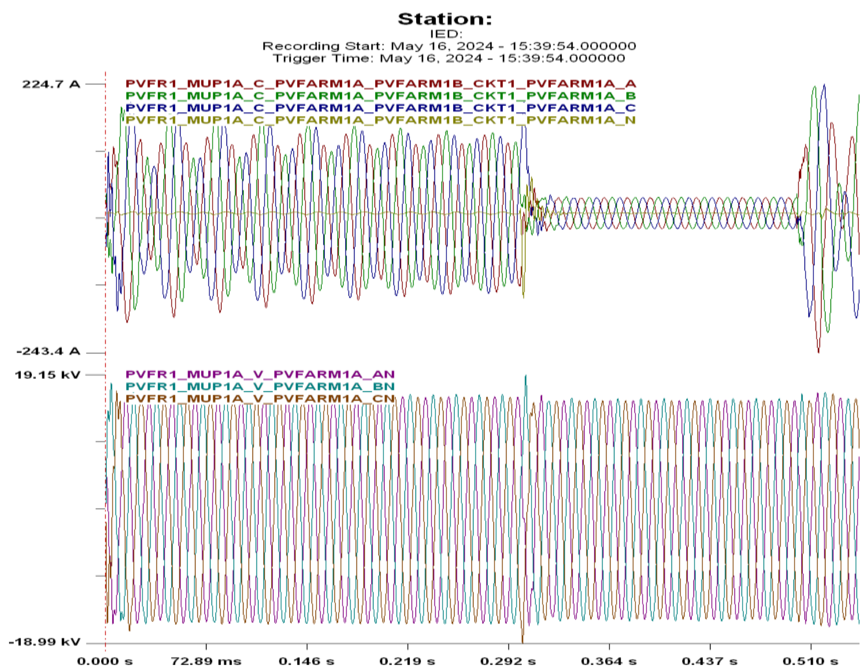

Figure 4.19: Transient current and voltage waveforms for PV farm 1 – module 1, 25 kV side (EVENT02)

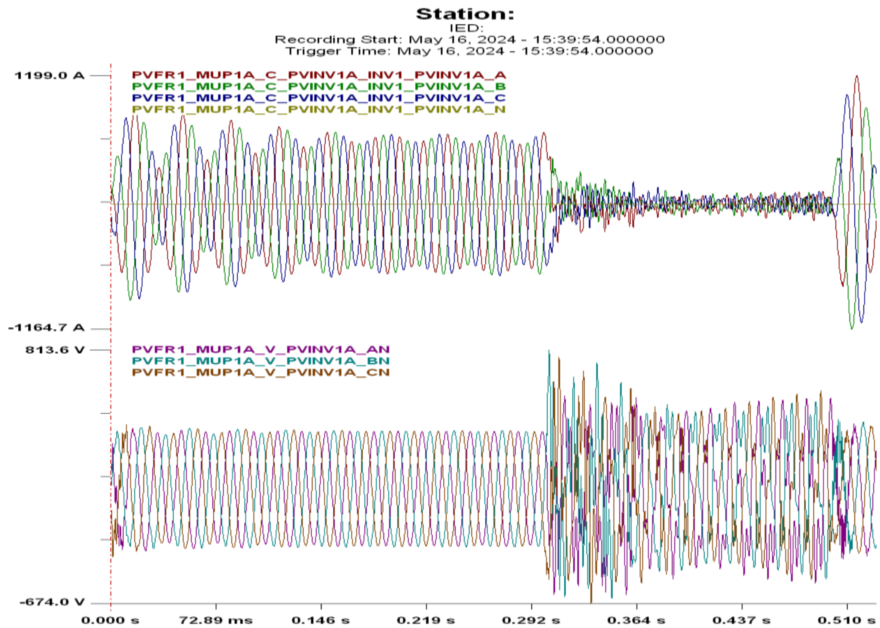

Figure 4.20: Transient current and voltage waveforms for PV farm 1 – module 1, 480 V side (EVENT02)

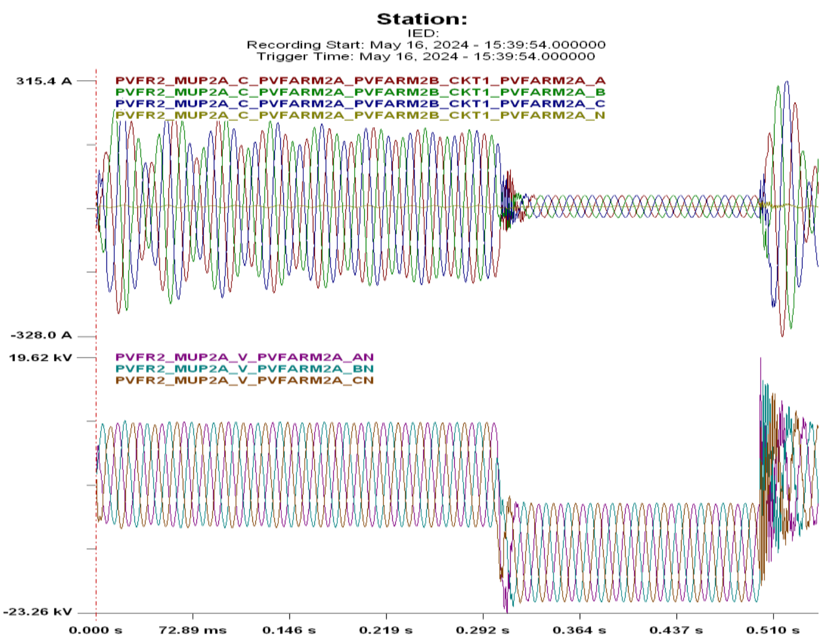

Figure 4.21: Transient current and voltage waveforms for PV farm 2 – module 1, 13.8 kV side (EVENT02)

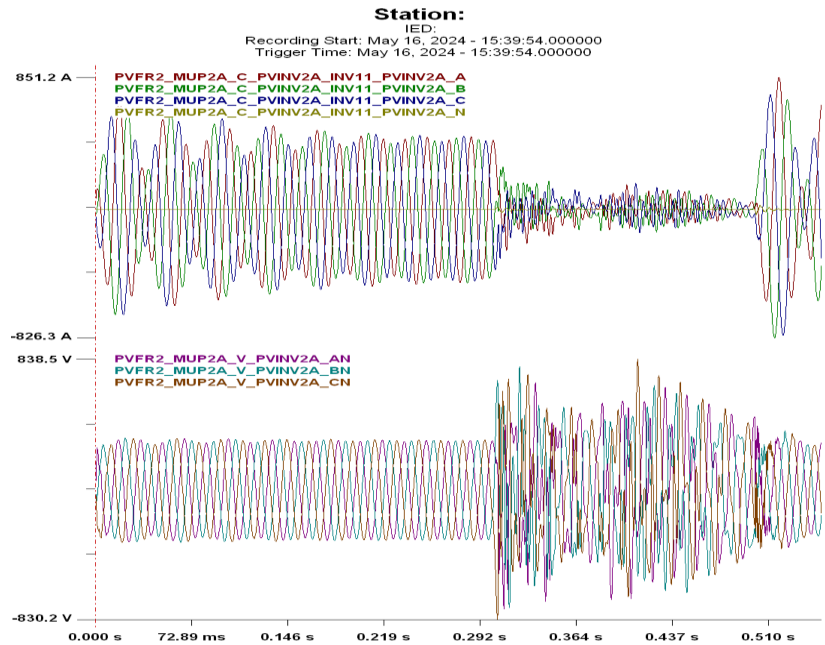

Figure 4.22: Transient current and voltage waveforms for PV farm 2 – module 1, 480 V side (EVENT02)

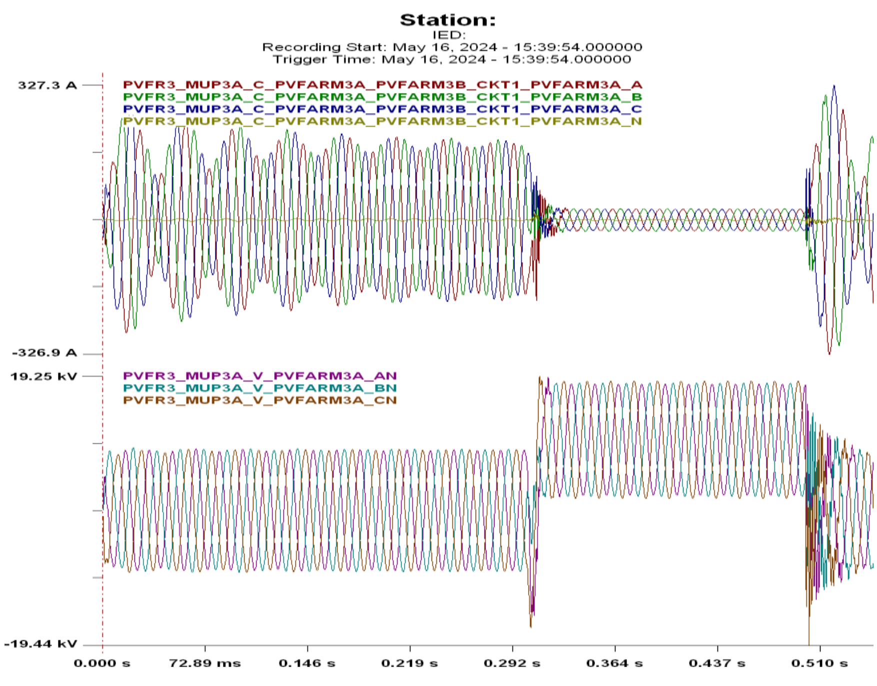

Figure 4.23: Transient current and voltage waveforms for PV farm 3 – module 1, 13.8 kV side (EVENT02)

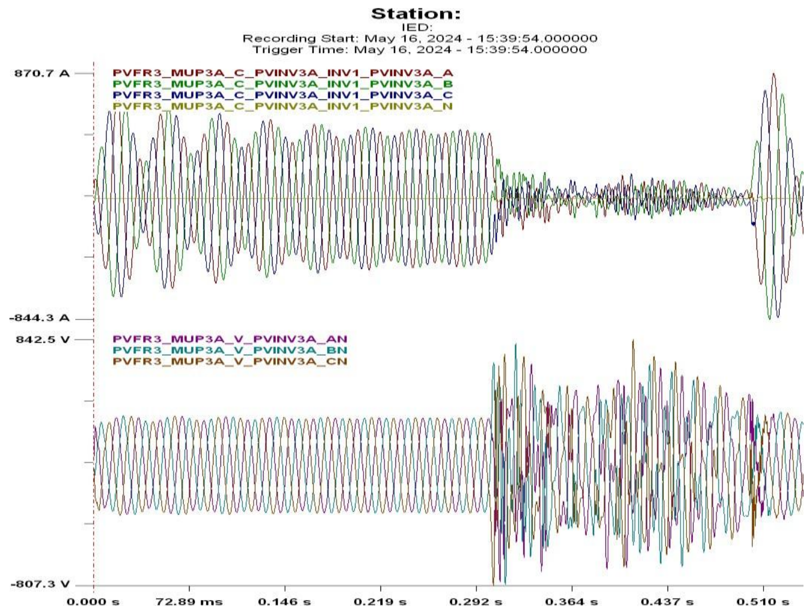

Figure 4.24: Transient current and voltage waveforms for PV farm 3 – module 1, 480 V side (EVENT02)

4.2.5 Remedial Actions EVENT02_RA00

Table 4.3: Remedial Actions for EVENT02_RA00

Item	Description
Event	PV 1 Farm’s load is connected to the high side of XRFM, PV 3 Farm’s load is connected to the high side of XRFM. In other words, changing load locations from low side of XRFM to high side of XRFM
Remedial Action	EVENT02_RA00: Connect 12 capacitor banks at each PV farm. Increase the value of the capacitor bank connected to the 25.0 kV side of PV Farm 1 XRFM. Add a new capacitor bank to the 13.8 kV side of XRFM connected to PV Farm 3.
Simulation Results	Results of EVENT02_RA00 are shown in Figure 4.25-Figure 4.30: PV Farm 1 • Reduction of high-side overvoltage spike. • No change in the low-side overvoltage. PV Farm 2 • Reduction in high-side overvoltage from 106% to 57% above nominal • Little increase of low-side overvoltage to 1564 V. PV Farm 3 • Reduction in high-side overvoltage from 70% to 57%. • Little increase of low-side overvoltage to 1560 V. We were able to reduce the overvoltage at the high-side of PV Farms.

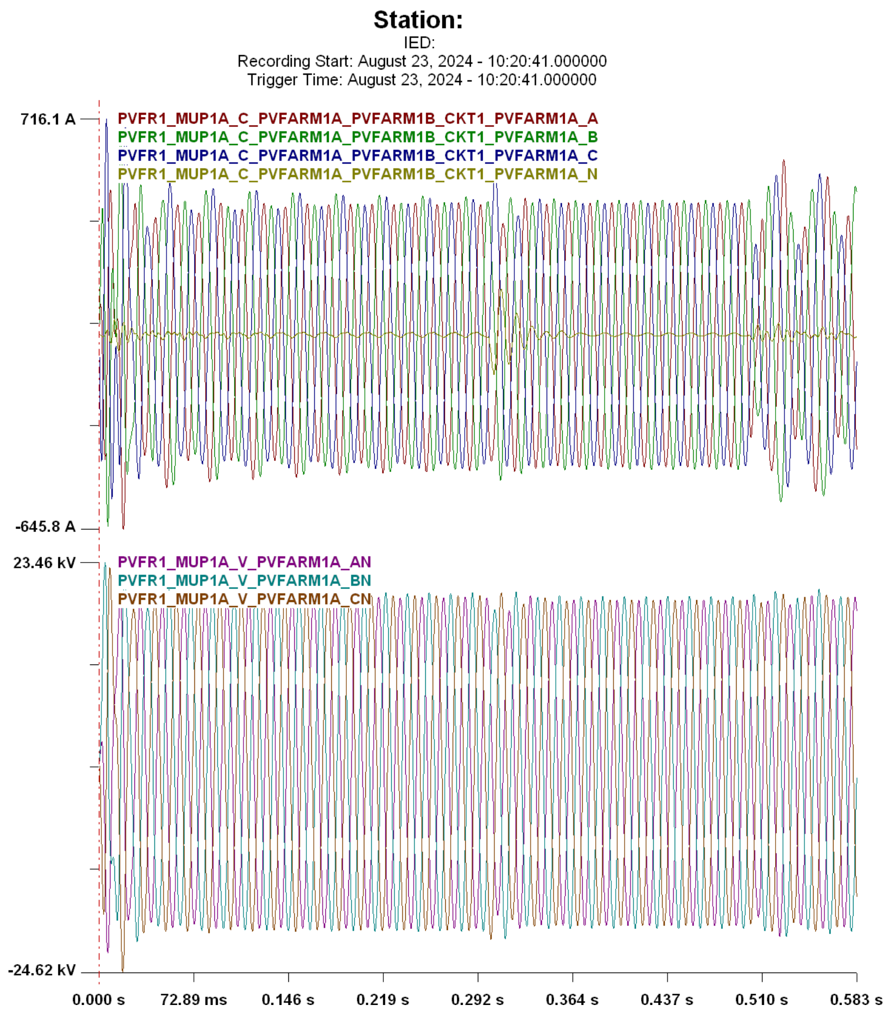

Figure 4.25: Transient current and voltage waveforms for PV farm 1 – module 1, 25 kV side (EVENT02_RA00)

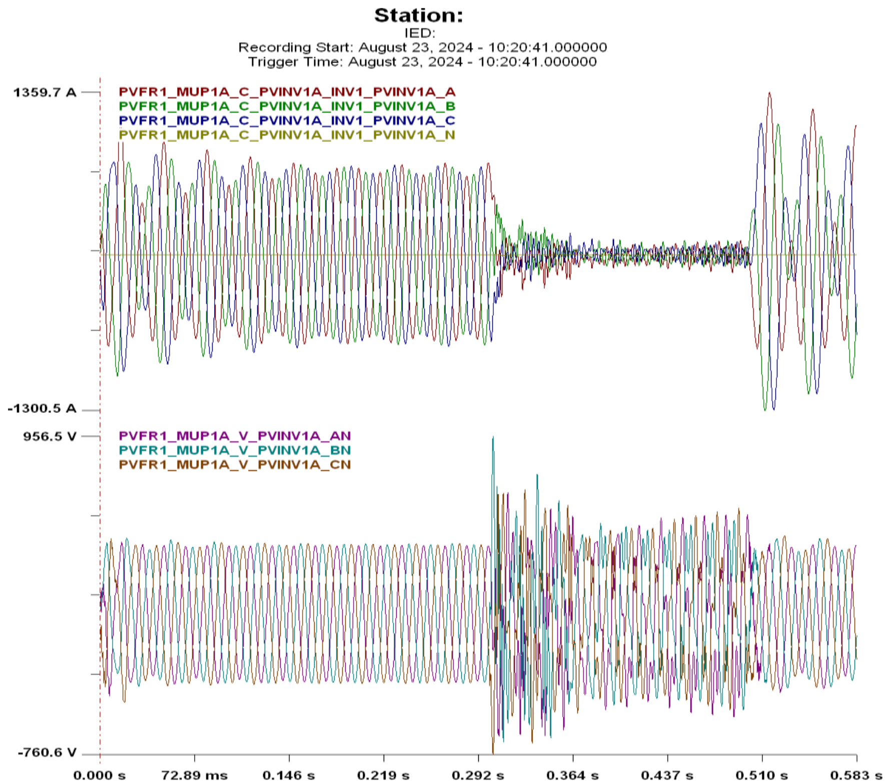

Figure 4.26: Transient current and voltage waveforms for PV farm 1 – module 1, 480 V side (EVENT02_RA00)

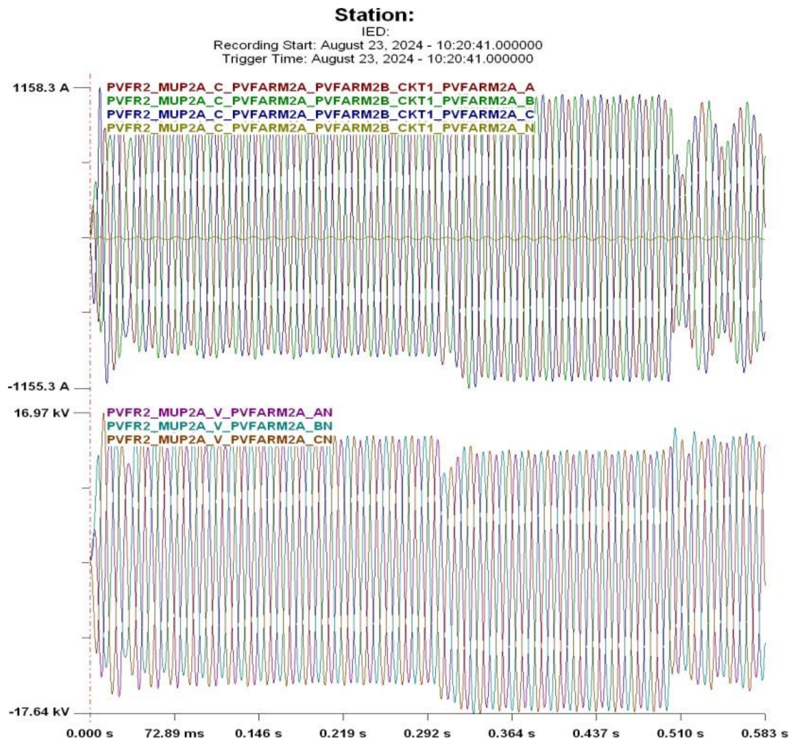

Figure 4.27: Transient current and voltage waveforms for PV farm 2 – module 1, 13.8 kV side (EVENT02_RA00)

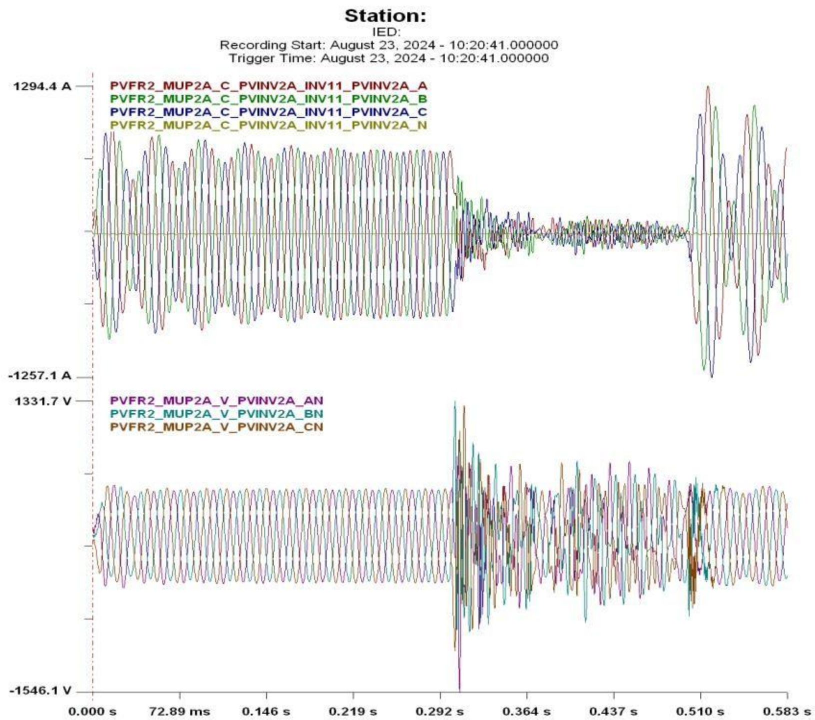

Figure 4.28: Transient current and voltage waveforms for PV farm 2 – module 1, 480 V side (EVENT02_RA00)

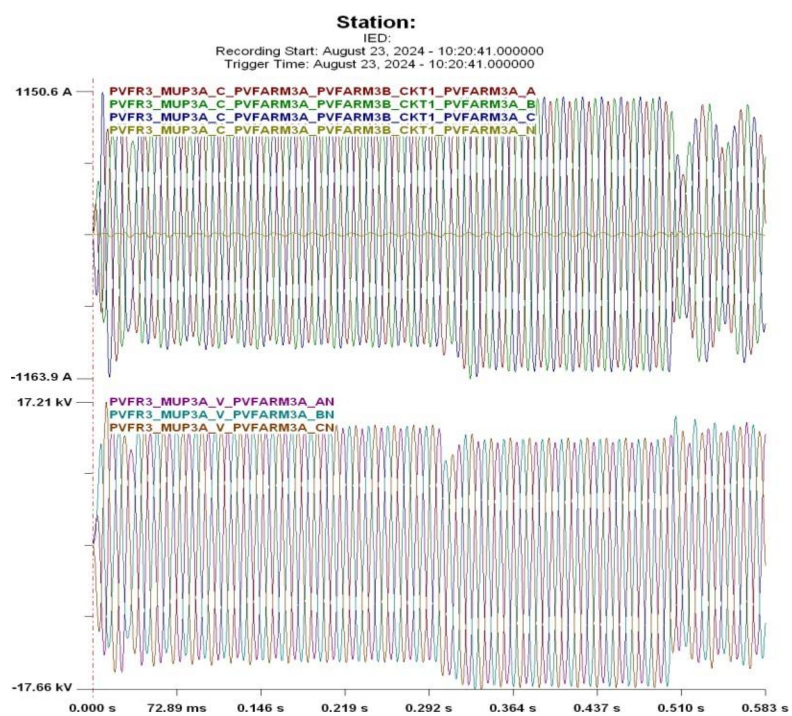

Figure 4.29: Transient current and voltage waveforms for PV farm 3 – module 1, 13.8 kV side (EVENT02_RA00)

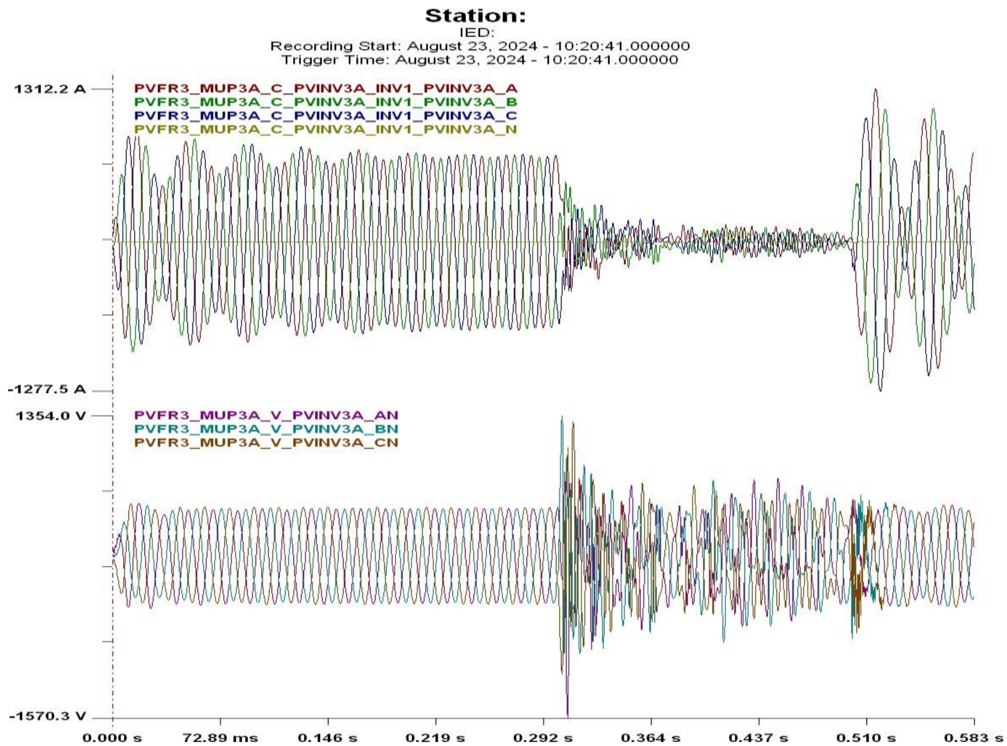

Figure 4.30: Transient current and voltage waveforms for PV farm 3 – module 1, 480 V side (EVENT02_RA00)

4.2.6 EVENT03

For EVENT03, we explore the change in temporary overvoltage when ground impedance is changed. Low impedance ground for all farms (0.5 ohms). Figure 4.31 through Figure 4.36 show the simulation results for EVENT03 at various PV farm locations.

The summary of the results for EVENT03 is provided below:
PV Farm 1
- No overvoltage at the high-side.
- Overvoltage at the low-side of 66.26% with a

peak of 694.7 V. PV Farm 2
- Overvoltage of 50.52% for the high-side with peak overvoltage of 16,960 V
- Overvoltage of 81.77% for the low-side with peak

overvoltage of 712.4 V. PV Farm 3
- An overvoltage of 21.23% at the high-side with peak overvoltage of 13,660 V.
- Overvoltage of 85.47% at the low-side with peak overvoltage of 726.9 V.

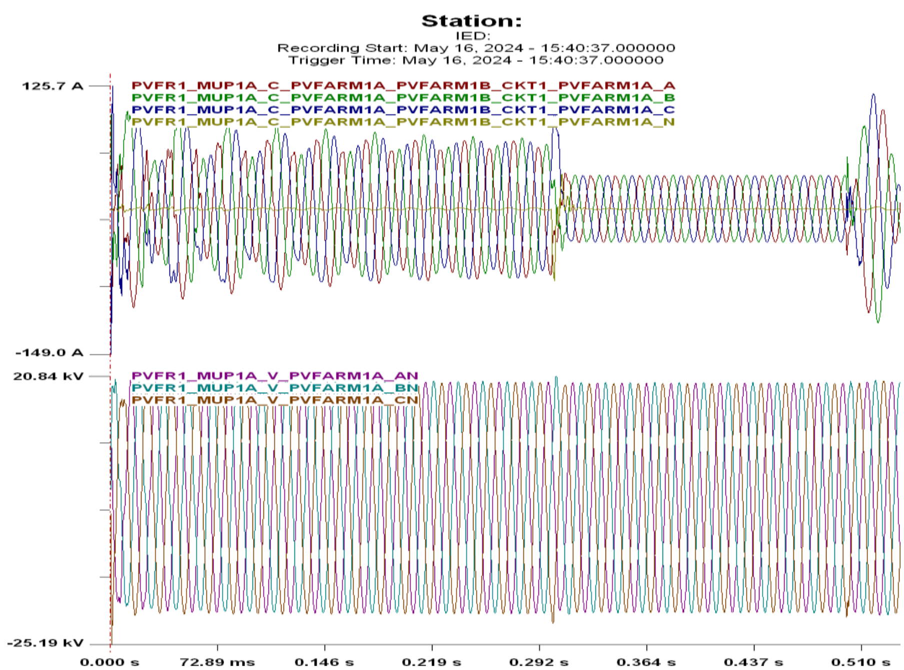

Figure 4.31: Transient current and voltage waveforms for PV farm 1 – module 1, 25 kV side (EVENT03)

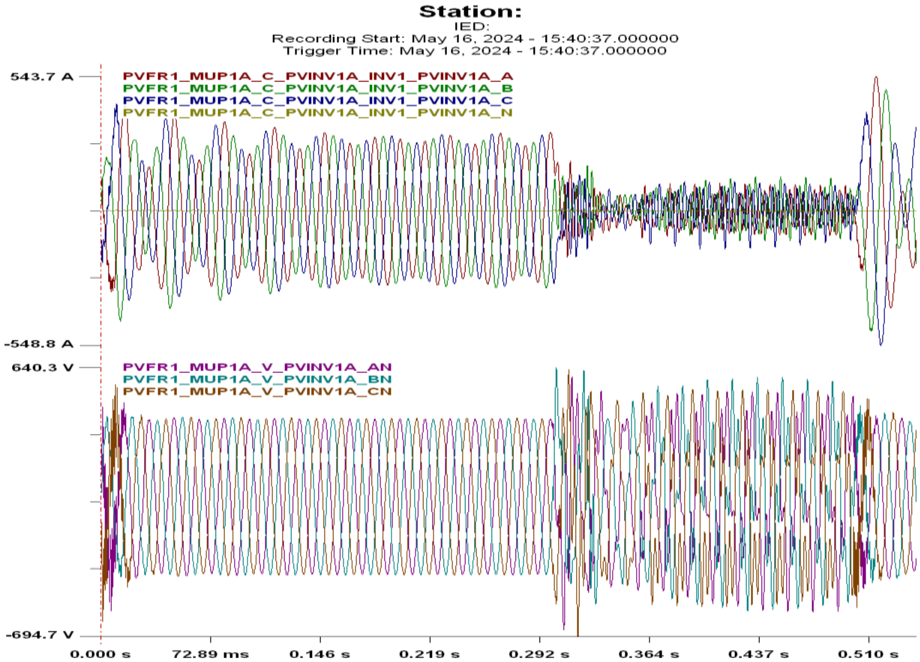

Figure 4.32: Transient current and voltage waveforms for PV farm 1 – module 1, 480 V side (EVENT03)

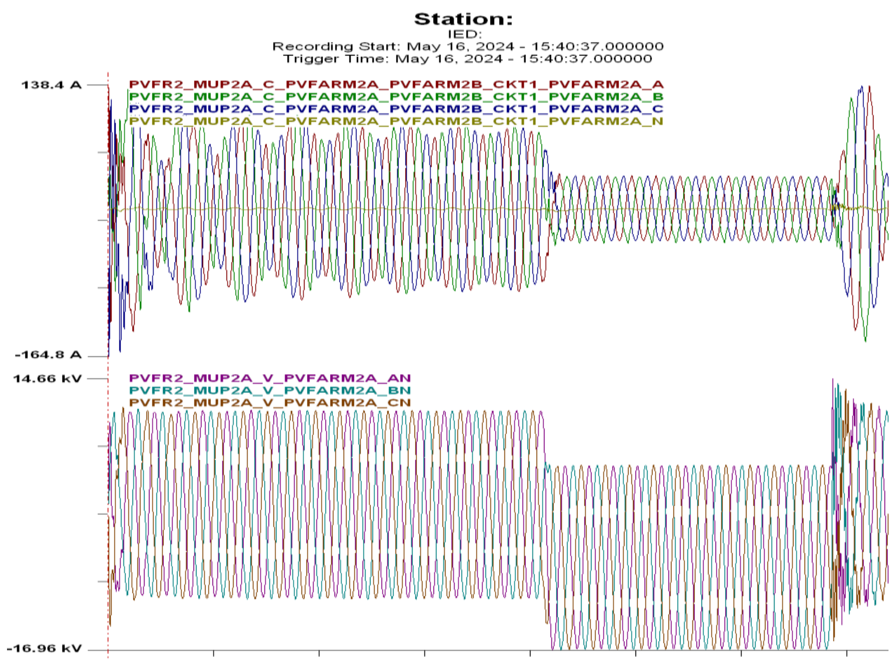

Figure 4.33: Transient current and voltage waveforms for PV farm 2 – module 1, 13.8 kV side (EVENT03)

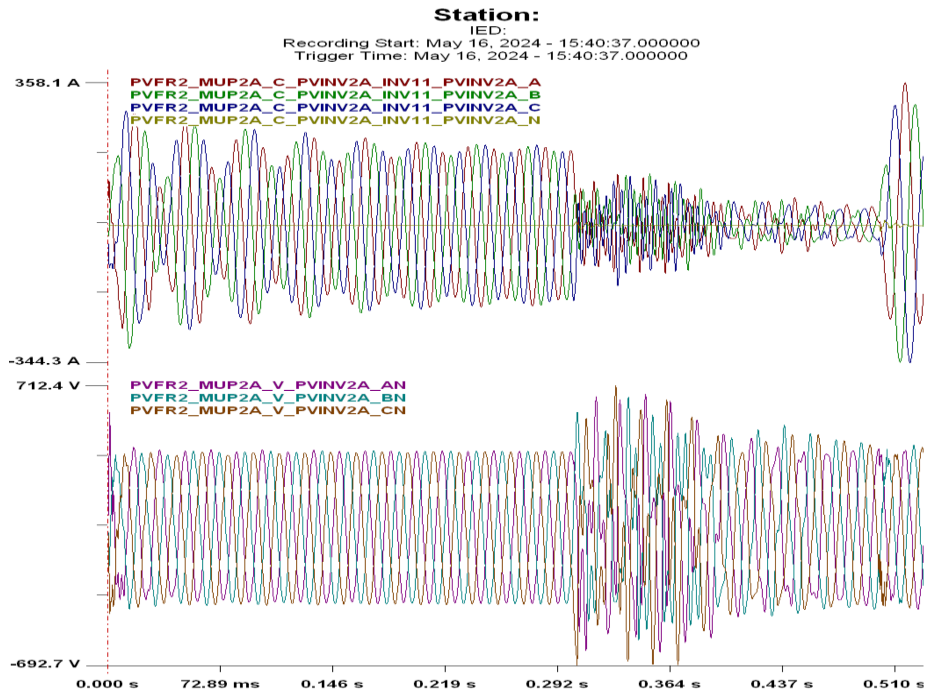

Figure 4.34: Transient current and voltage waveforms for PV farm 2 – module 1, 480 V side (EVENT03)

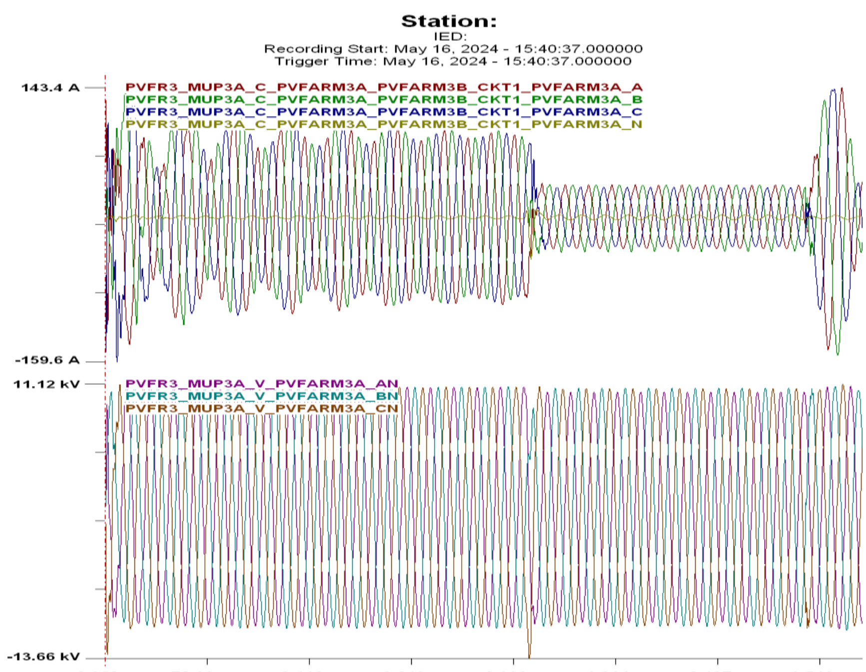

Figure 4.35: Transient current and voltage waveforms for PV farm 3 – module 1, 13.8 kV side (EVENT03)

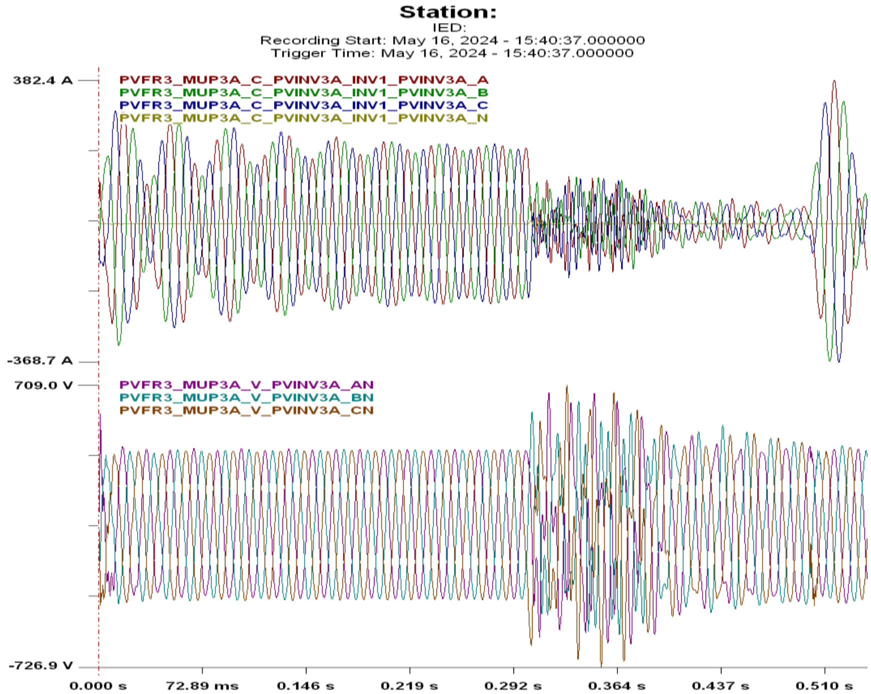

Figure 4.36: Transient current and voltage waveforms for PV farm 3 – module 1, 480 V side (EVENT03)

4.2.7 Remedial Actions EVENT03_RA00

Table 4.4: Remedial Actions for EVENT02_RA00

Item	Description
Event	Low impedance ground for all farms (0.5 ohms)
Remedial Action	EVENT03_RA00: Match the grounding of PV farms with the external XRFM. Increase the loads connected to PV Farms 1 and 3 by about 100%.

Simulation Results	Results of EVENT03_RA00 are shown in Figure 4.37-Figure 4.42: PV Farm 1- • Reduction of high-side overvoltage spike. • Little increase in the low-side overvoltage. PV Farm 2 • Little increase of high-side overvoltage spike. • Little increase of low-side overvoltage to 1546 V. PV Farm 3 • Little increase of high-side overvoltage spike.
	• Little increase of low-side overvoltage to 1579 V. We were unable to reduce the overvoltage at this event to due severe impact of reducing impedance ground for all farms to 0.5 ohms.

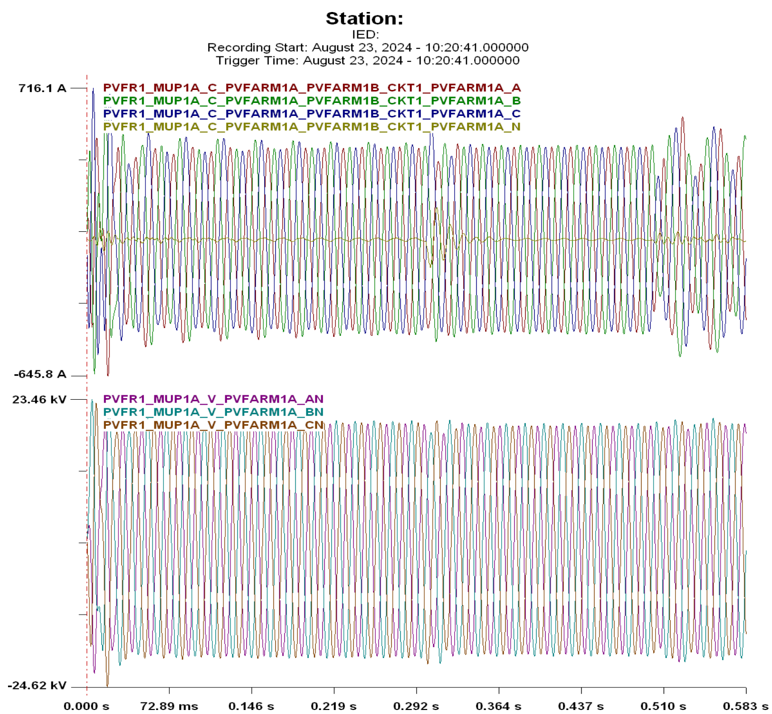

Figure 4.37: Transient current and voltage waveforms for PV farm 1 – module 1, 25 kV side (EVENT03_RA00)

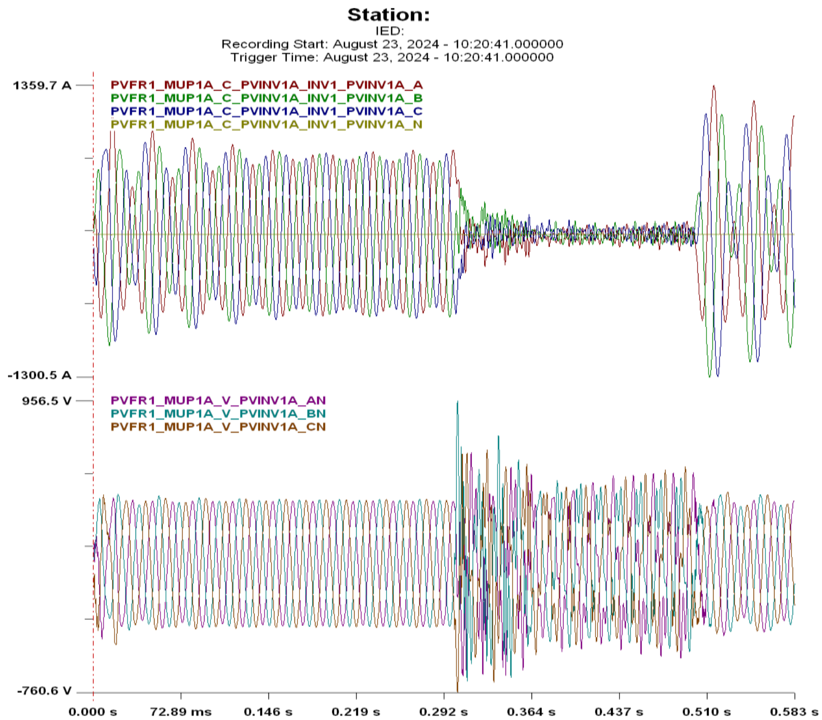

Figure 4.38: Transient current and voltage waveforms for PV farm 1 – module 1, 480 V side (EVENT03_RA00)

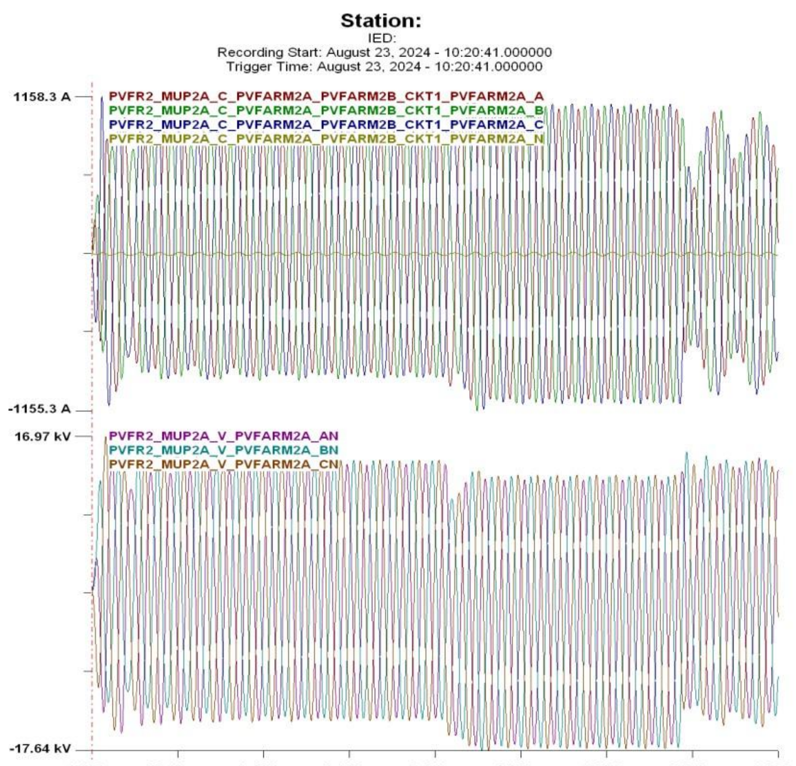

Figure 4.39: Transient current and voltage waveforms for PV farm 2 – module 1, 13.8 kV side (EVENT03_RA00)

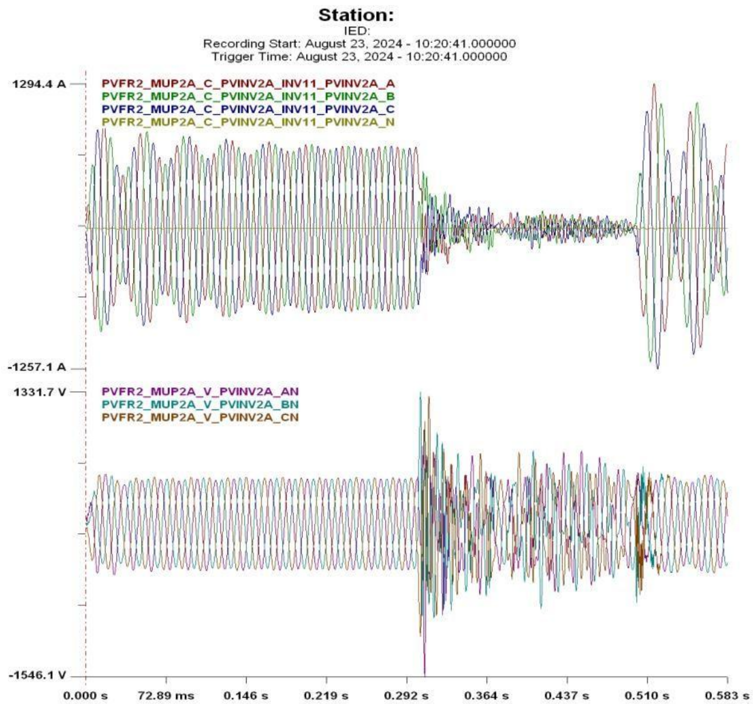

Figure 4.40: Transient current and voltage waveforms for PV farm 2 – module 1, 480 V side (EVENT03_RA00)

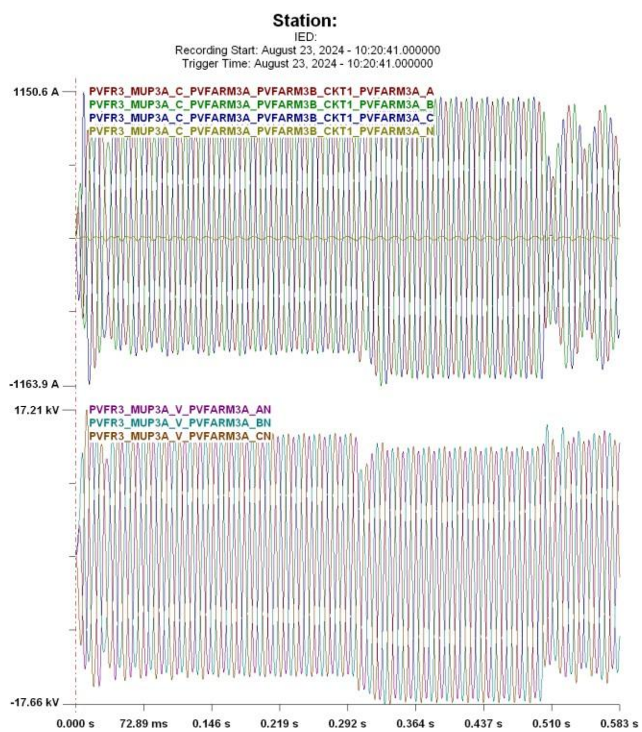

Figure 4.41: Transient current and voltage waveforms for PV farm 3 – module 1, 13.8 kV side (EVENT03_RA00)

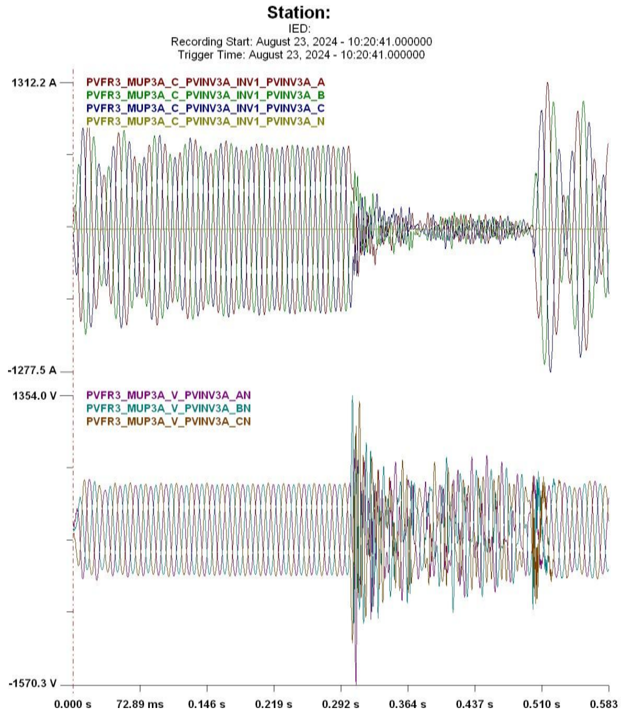

Figure 4.42: Transient current and voltage waveforms for PV farm 3 – module 1, 480 V side (EVENT03_RA00)

4.2.8 EVENT04

For EVENT04, we explore the change in temporary overvoltage when two changes are made on load locations and transformers connections. All PV Farms are Delta-connected to XRFMs, and loads are moved to high-side for PV Farms 1 and 3. Figure 4.43 through Figure 4.48 show the simulation results for EVENT04 at various PV farm locations.

The summary of the results for EVENT04 is provided below:

PV Farm 1

- Overvoltage at the high-side of 15.57% with a peak of 23,590 V.
- Overvoltage at the low-side of 74.37% with a

peak of 683.4 V. PV Farm 2

- Overvoltage of 109.09% for the high-side with peak overvoltage of 23,560 V
- Overvoltage of 114.02% for the low-side with peak

overvoltage of 838.8 V. PV Farm 3

- Overvoltage of 66.41% at the high-side with peak overvoltage of 18,750 V.
- Overvoltage of 115.48% at the low-side with peak overvoltage of 844.5 V.

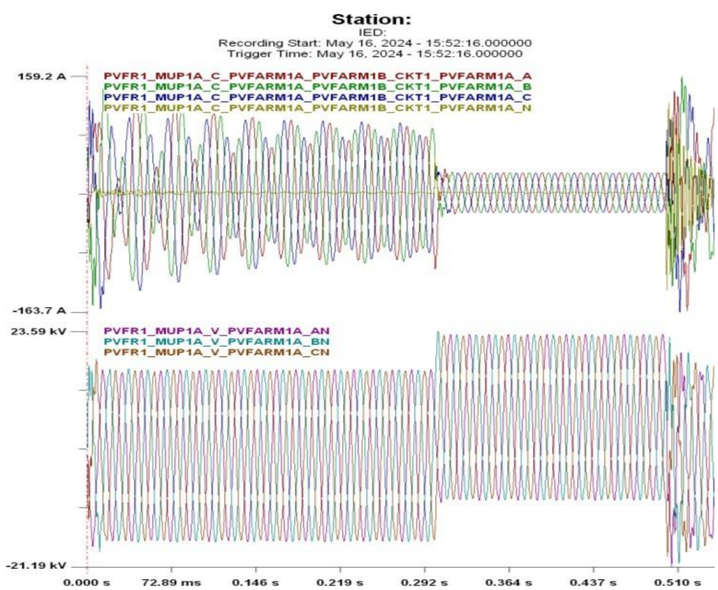

Figure 4.43: Transient current and voltage waveforms for PV farm 1 – module 1, 25 kV side (EVENT04)

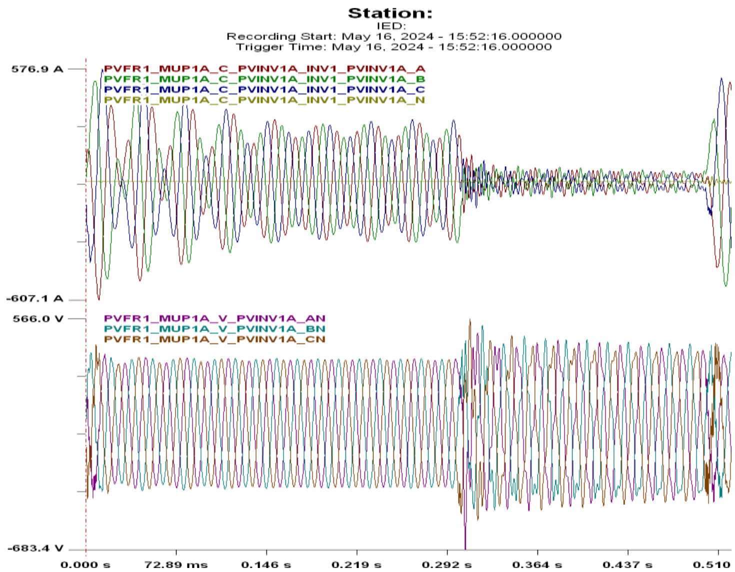

Figure 4.44: Transient current and voltage waveforms for PV farm 1 – module 1, 480 V side (EVENT04)

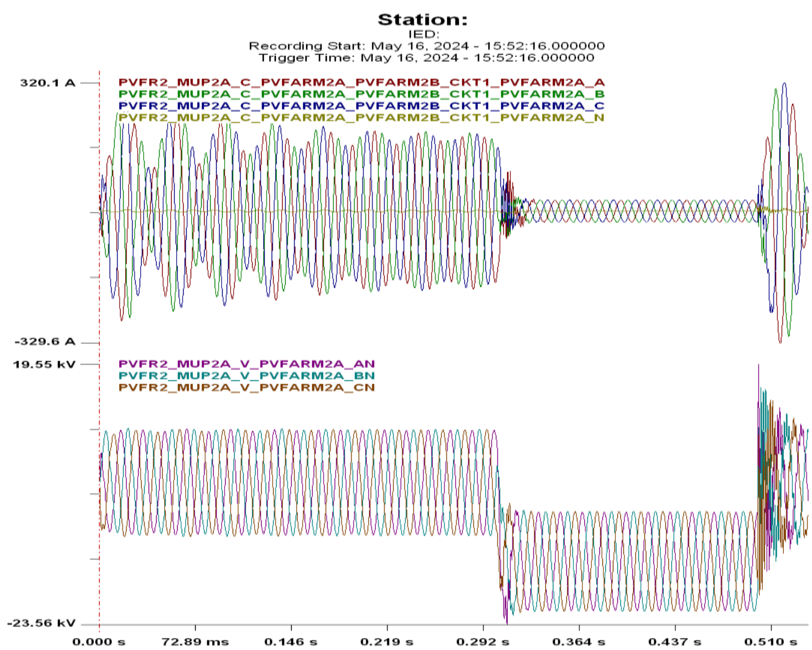

Figure 4.45: Transient current and voltage waveforms for PV farm 2 – module 1, 13.8 kV side (EVENT04)

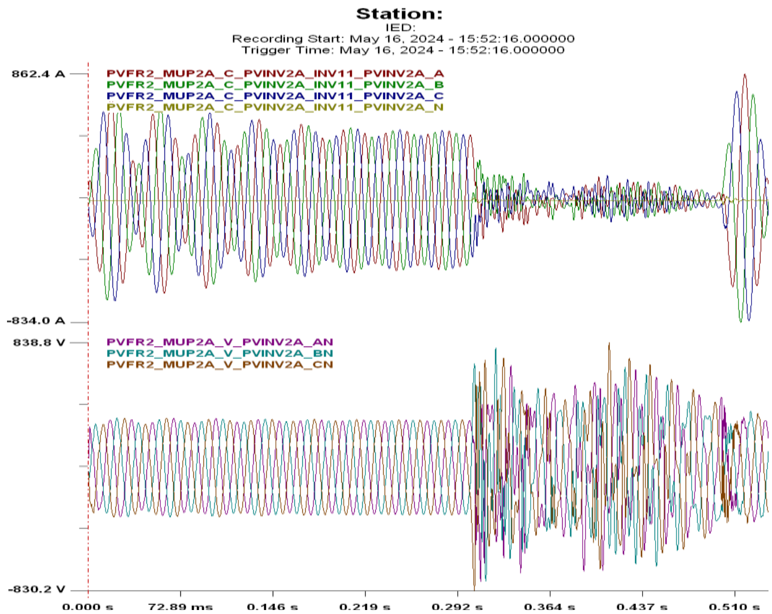

Figure 4.46: Transient current and voltage waveforms for PV farm 2 – module 1, 480 V side (EVENT04)

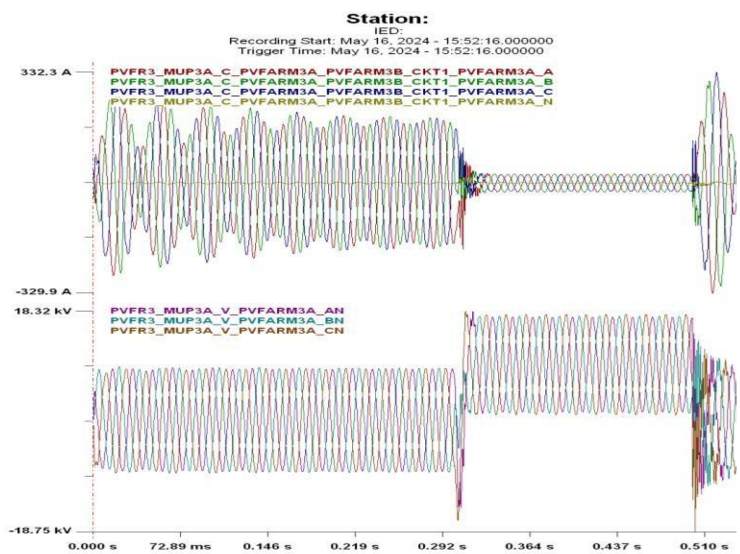

Figure 4.47: Transient current and voltage waveforms for PV farm 3 – module 1, 13.8 kV side (EVENT04)

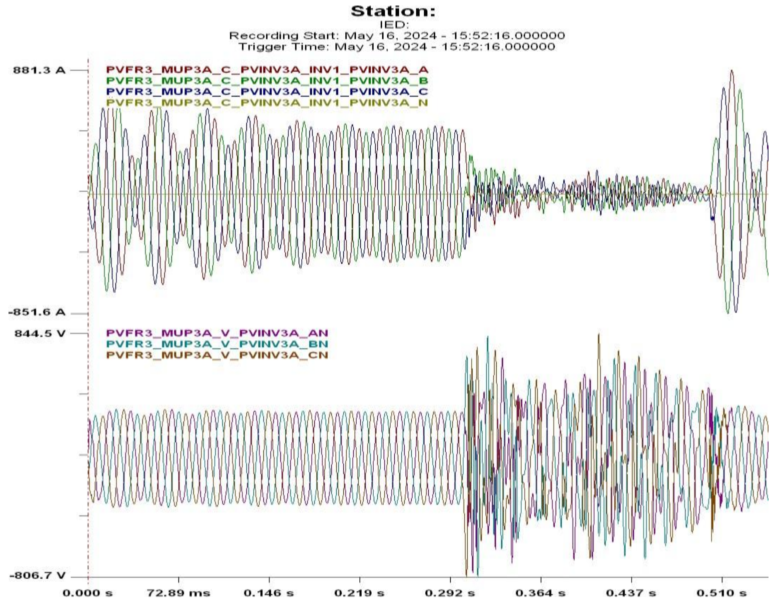

Figure 4.48: Transient current and voltage waveforms for PV farm 3 – module 1, 480 V side (EVENT04)

4.2.9 Remedial Actions EVENT04_RA00

Table 4.5: Remedial Actions for EVENT04_RA00

Item	Description
Event	All PV Farms are Delta-connected to XRFMs, and loads are moved to high-side for PV Farms 1 and 3.
Remedial Action	EVENT04_RA04: Make the PV Farms' (1, 2, and 3) transformers delta-delta connected.
Summary of results	Results of EVENT04_RA00 in Figure 4.49-Figure 4.54: PV Farm 1 • Similar high-side overvoltage spike. • Similar low-side overvoltage. PV Farm 2 • Reduction of overvoltages on the high-side from 109% to 50%. • Reduction of low-side overvoltages from 838.8 V to 649.3 V. PV Farm 3 • Reduction of overvoltages on the high-side from 66% to 53%. • Reduction of low-side overvoltages from 844.5 V to 672.2 V. We were able to reduce the overvoltage spikes at PV Farms 2 and 3.

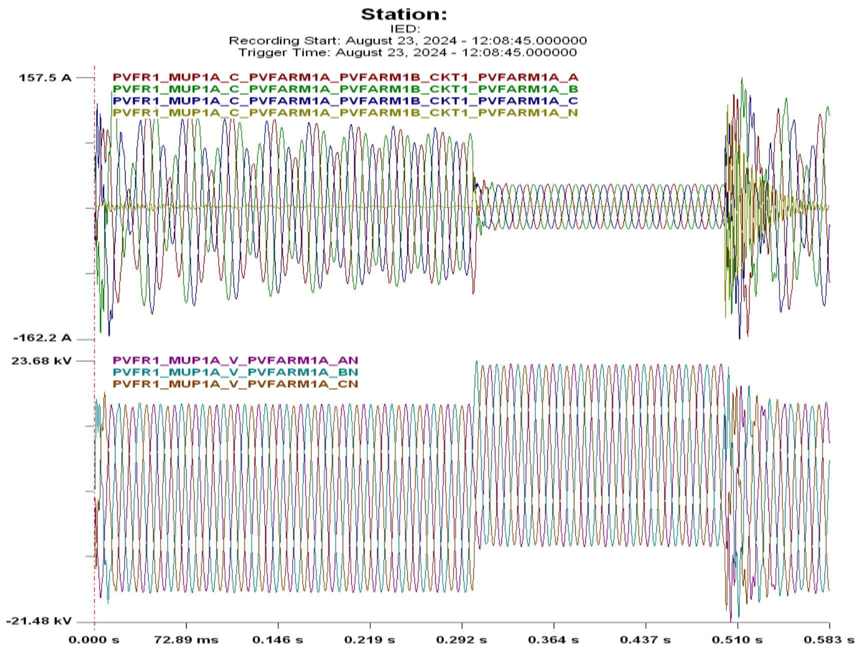

Figure 4.49: Transient current and voltage waveforms for PV farm 1 – module 1, 25 kV side (EVENT04_RA00)

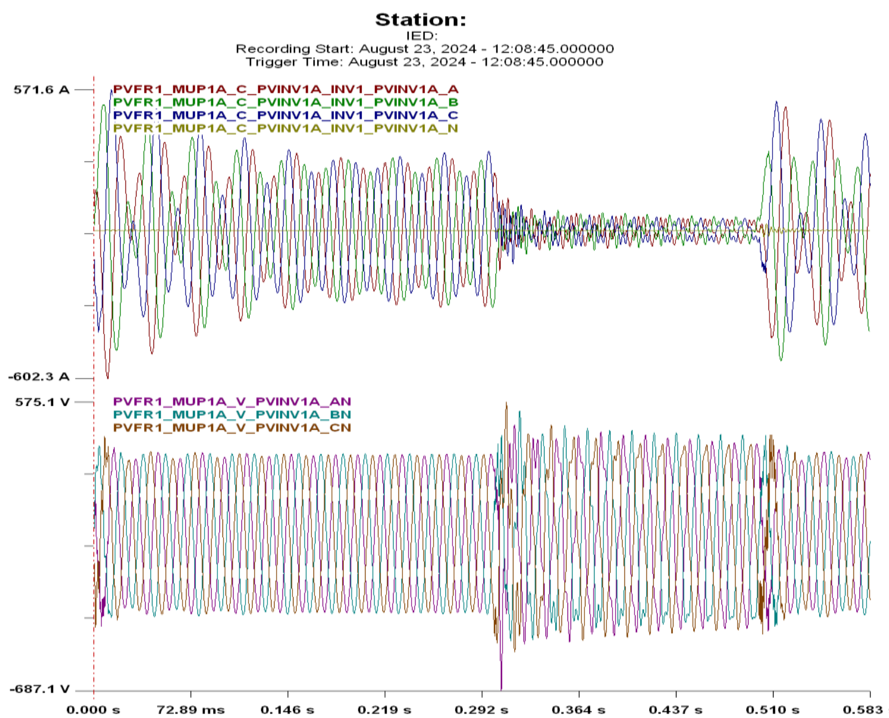

Figure 4.50: Transient current and voltage waveforms for PV farm 1 – module 1, 480 V side (EVENT04_RA00)

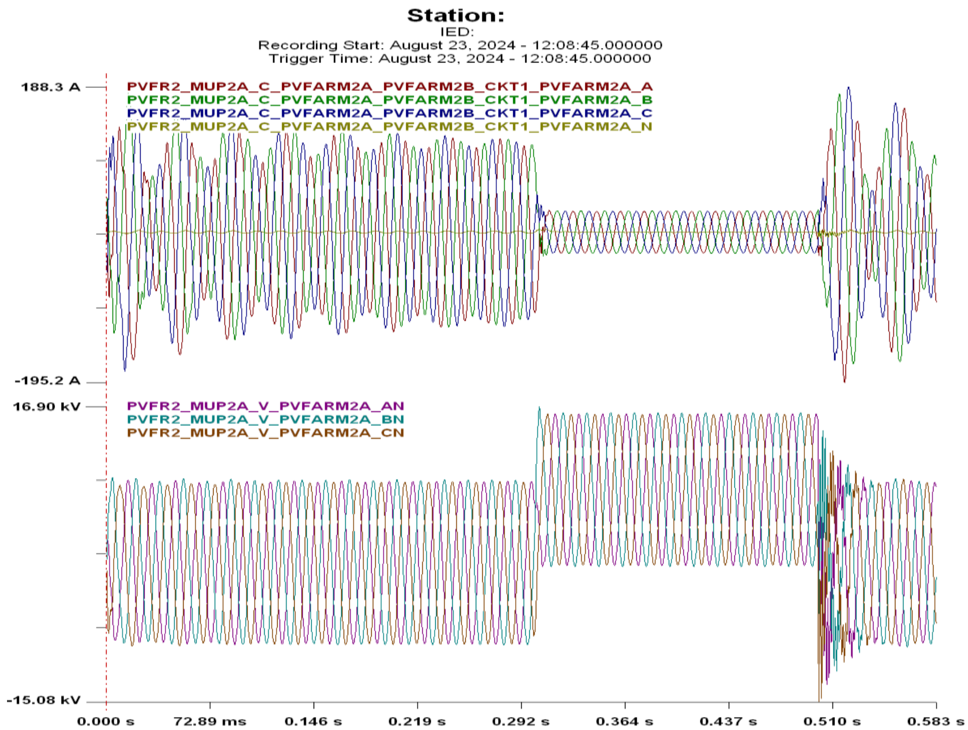

Figure 4.51: Transient current and voltage waveforms for PV farm 2 – module 1, 13.8 kV side (EVENT04_RA00)

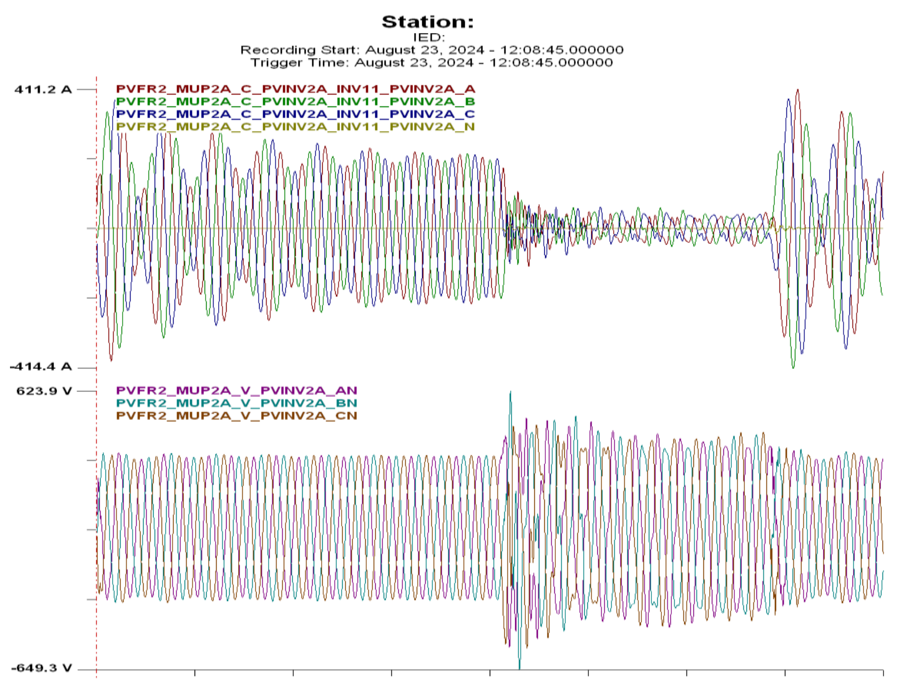

Figure 4.52: Transient current and voltage waveforms for PV farm 2 – module 1, 480 V side (EVENT04_RA00)

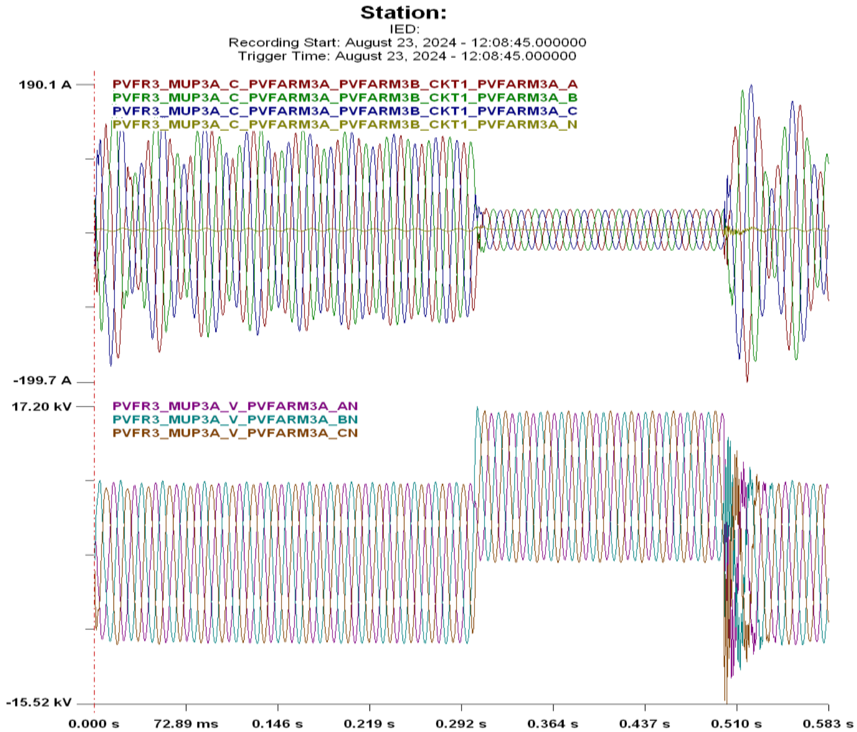

Figure 4.53: Transient current and voltage waveforms for PV farm 3 – module 1, 13.8 kV side (EVENT04_RA00)

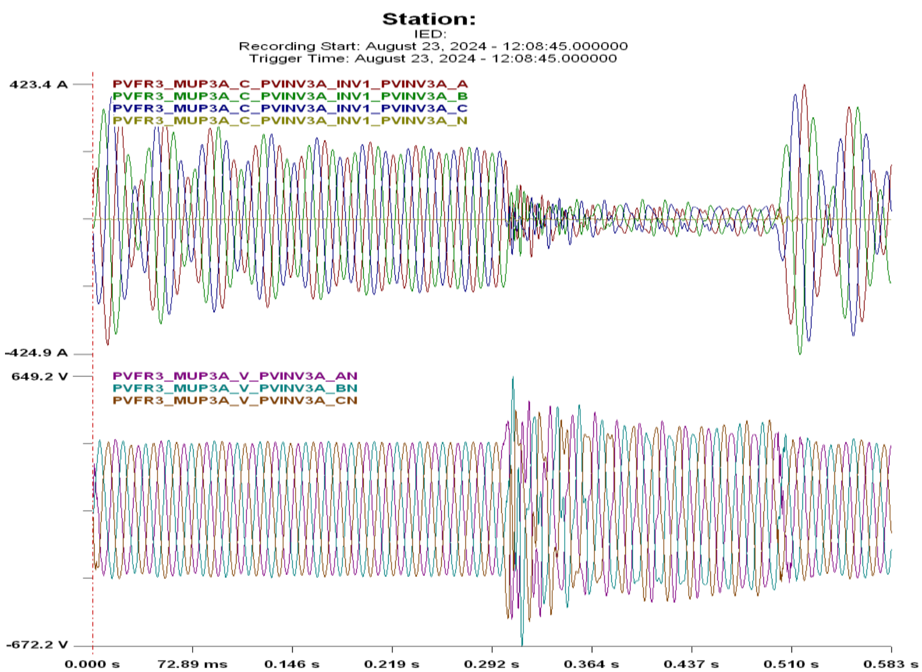

Figure 4.54: Transient current and voltage waveforms for PV farm 3 – module 1, 480 V side (EVENT04_RA00)

4.2.10 Summary

Table 4.6 provides a summary of the simulation results. The table also summarizes the effect of remedial actions.

Table 4.6: Summary of Simulation Results (Overvoltage Percentage of the Base High and Low Sides Voltage)

Event	PV Farm 1 (25 kV/480 V)	PV Farm 2 (13.8 kV/480 V)	PV Farm 3 (13.8 kV/480 V)	Severity
EVENT00	(small spike / 77.3%)	(50.52%/ 81.77%)	(21.23% / 85.47%)	
EVENT01	(small dip / 64.21%)	(small dip / 41.51%)	(no spike / 44.72%)	
EVENT01_RA00	(small dip / 62.48%)	(reduction in the dip/ 104.63%)	(no spike / 101.57%)	
EVENT02	(no spike / 107.59%)	(106.43% / 113.94%)	(70.84% / 114.96%)	
EVENT02_RA00	(reduction in spike / 143.93%)	(56.55% / 294.47%)	(56.73% / 300.59%)	
EVENT03	(no spike / 77.26%)	(50.52% / 81.77%)	(21.23% / 85.47%)	
EVENT03_RA00	(reduction in spike / 143.93%)	(56.55% / 294.47%)	56.73% / 300.59%)	
EVENT04	(15.57% / 74.37%)	(109.09 / 114.02%)	(66.41% / 115.48%)	
EVENT04_RA00	(16.00% / 75.29%)	(49.99 % / 65.67%)	(52.65% / 71.52%)	

5. Effects of Temporary Transients on the Performance of the System

Temporary transients resulting from inverter ON/OFF actions may affect the operation of the system, including protection and control reliability, damage of equipment, and failures of power and control equipment. Malfunctions of protection and control have been observed during these transients. We will discuss a mis-operation observed in the Greek Island of Rhodes due to the transients from the inverters. The aim of this section is to report possible malfunction of protection and control systems when IBRs temporarily get disconnected from a power grid.

5.1 Rhodes Island Historical Event

The incident described here occurred in 2016 in the island of Rhodes in Greece and was investigated in detail in [1]. The electrical system of Rhodes at that time is shown in Figure 5.1. It consisted of a single conventional power station, Soroni Thermal Power Plant (TPP), with 11 synchronous generating units of 207 MW capacity in total, and a HV transmission system with five HV/MV substations. Each generator of Soroni TPP is connected to the HV buses through a step-up transformer. The transmission system had recently been upgraded from 66 kV to 150 kV, to facilitate the connection of a second power station at the South of the island that was not yet connected at the time of the incident.

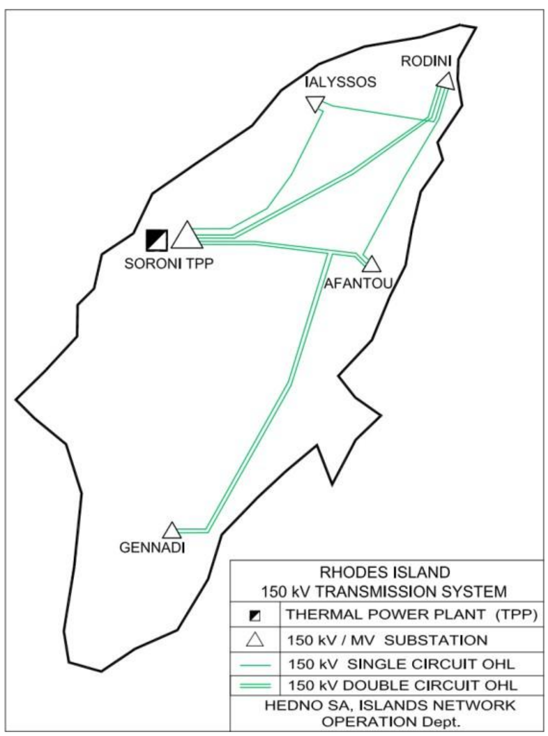

Figure 5.1: Electrical system of Rhodes in 2016 [1]

Apart from thermal generation there were also five wind power plants (WPPs) installed in Rhodes in 2016 with a total capacity of 49 MW. Several photovoltaic (PV) units were also installed at MV and LV level, with 18 MW total estimated capacity. Capacity wise, the system has a 32.37%

penetration of IBRs.
The upgrade of the HV system to 150 kV created an excess of capacitive charging current making the system prone to overvoltage. As the second power plant in the South of the island was not yet in operation, the reactive power generated during light load conditions had to be absorbed by the generating units at Soroni TPP. It is noted that the peak load of the system in 2016 was approximately 200 MW and occurred during summer. The light load periods are the months of March and November when the total system load can drop to 35 MW.

The process of absorbing the excessive reactive power during light load conditions is performed automatically by the synchronous generating units, which are controlling their terminal voltage through their automatic voltage regulator (AVR). In so doing, they have to decrease their excitation voltage and as noted in the Introduction, in island systems UELs are normally not used. Thus, sometimes the operators manually change the voltage setpoint to avoid excessive reactive absorption by the generators. As will be seen below, this practice can have adverse effects in extreme cases.

On March 19, 2016, the autonomous power system of Rhodes experienced an uncontrolled overvoltage phenomenon leading to a blackout. The event is analysed in [1] and is briefly described below. Wind power generation was very low during the event (approximately 2 MW) and there was no PV generation because of the time of day (05:00 to 05:22). Five synchronous units were in operation at that time, sharing a load of about 45 MW.

Shortly before 05:00, one of the gas turbine units (G3) was ramped down and eventually disconnected at 05:17. Of the remaining four synchronous units, one large diesel unit (D4) was found after the event to be in constant reactive power operation, thus not participating in voltage regulation. As a result, voltage regulation (and absorption of excessive reactive power) depended only on the remaining gas turbine unit G4 and two small diesel units D1 and D2.

Shortly after the disconnection of G3, oscillations occurred at the other gas turbine unit G4 resulting in an increase of its generation causing overfrequency and a subsequent unit trip just after 05:20. The trip of G3 caused a severe frequency drop that led to underfrequency load shedding. A total of 16 MW was rejected, which was excessive for the light load at the time.

As a result of these events, the only regulating units D1 and D2 experienced a severe under-excitation, in order to avoid transmission overvoltage. At the same time, load tap changers (LTCs) on distribution transformers were tapping to keep distribution voltages close to nominal, thus contributing to further rise of transmission voltages. Some LTCs were even found after the event to have exhausted their available tap range in the direction of increasing transmission voltage. It is noted that the increased transmission and distribution voltages also created an increase of reactive power generation by the transmission grid.

During these stressed conditions, an attempt to reduce the under-excitation of unit D2 by increasing its AVR voltage setpoint, resulted in an LOF relay trip of the other regulating unit D1. Following this, unit D2 was not able to regulate frequency and voltage by itself. Thus, the resulting overvoltage, which climbed above 170 kV (1.13 p.u.), finally caused a blackout of the whole system as depicted in Figure 5.2.

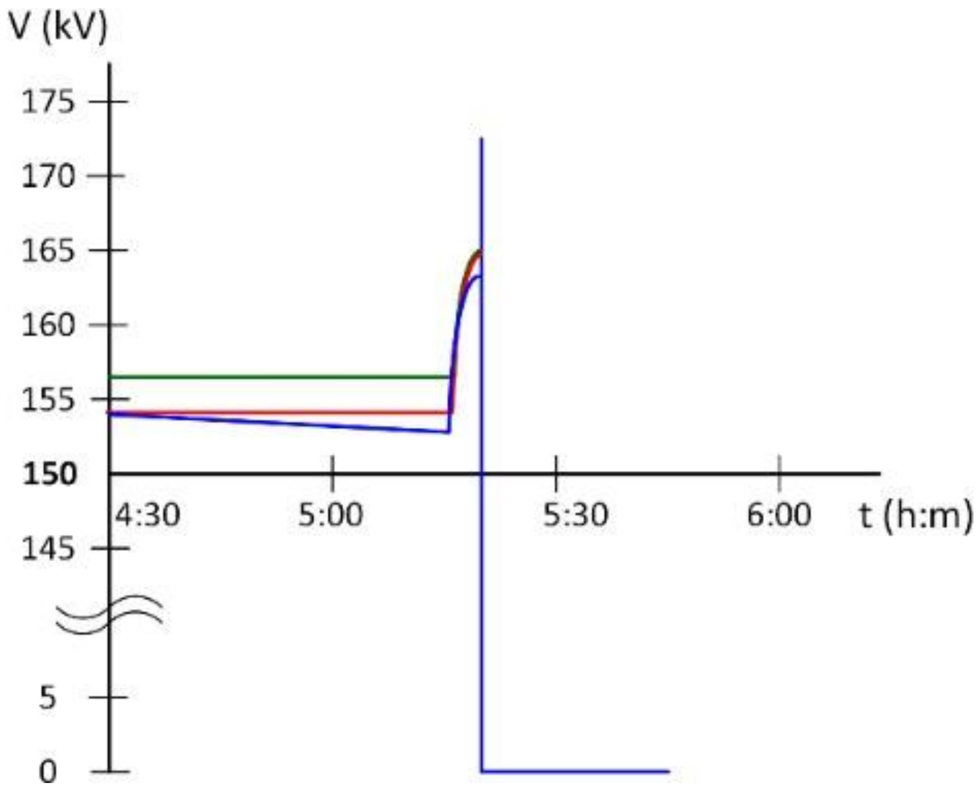

Figure 5.2: HV recording on March 16, 2016 [1]

5.2 Sequence of Events

The system described above was subjected to a similar sequence of events as the island system of Rhodes. Specifically, the simulation starts with an operating condition, where all PV farms operate normally, all loads are connected and absorb power and all synchronous generators operate normally with their usual controls. We refer to this period as period 1.

The next event is the dropout of one of the PV farms, specifically the 12 MWp PV farm. This is referred to as period 2.

The dropout of the PV farm affects the operation of a 15 MVA synchronous generator connected to the 25 kV circuit interconnecting the PV farm to the collector substation. The resulting generation-load imbalance causes frequency decrease and subsequent load shedding. The first load shedding occurs in a few seconds, and the second load shedding occurs another few seconds later. The time period of the first load shedding is period 3 and the time period after the second load shedding is period 4.

Later on, the PV farm is re-synchronized to the system. This is time period 5. Still later on, the first set of load shedding reconnects to the system. This is time period 6.

This sequence of events is summarized in Figure 5.3. The synchronous 15 MVA generator terminal voltage and terminal currents are also shown in Figure 5.3.

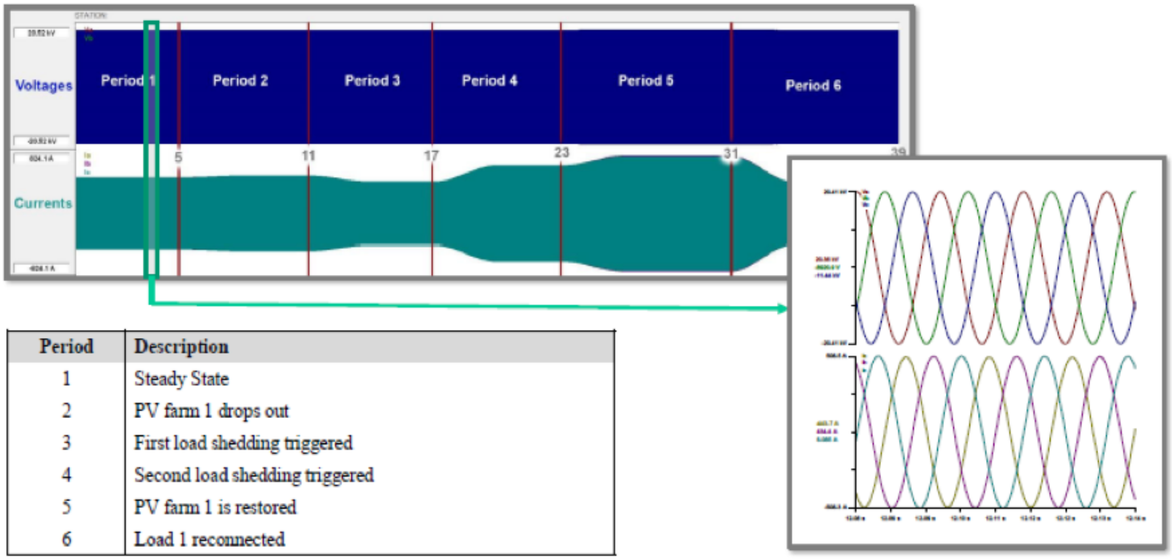

Period	Description
1	Steady State
2	PV farm 1 drops out
3	First load shedding triggered
4	Second load shedding triggered
5	PV farm 1 is restored
6	Load 1 reconnected

Figure 5.3: Sequence of Events and Generator Terminal Voltages and Currents

During simulation, we consider two relays: (a) the legacy LOF relay of the generator with settings determined by the parameters of the generator. We use the LOF relay with two circles determined by the synchronous impedance of the generator and offset by half of the transient direct axis impedance of the generator. The inner circle is that shown in Fig. 5.4 and considered in the long-term simulation of Section 2. (b) the estimation based protective relay; this relay estimates the full operating state of the generator; knowing the state of the generator, anything else can be computed for the generator; we selected to compute the internal generated voltage and the voltage drop along the impedances of the generator; knowledge of the state of the generator determines whether there is an internal fault in the generator, whether this is a loss of field or any other internal fault [5-8]. The results of the simulation are shown in Figure 5.4 through Figure 5.9 for the time periods 1 through 6 respectively. Note that during time periods 1, 2, 3, 5 and 6, the generator operates near normal conditions. During period 4, the generator operates at severe under-excitation condition.

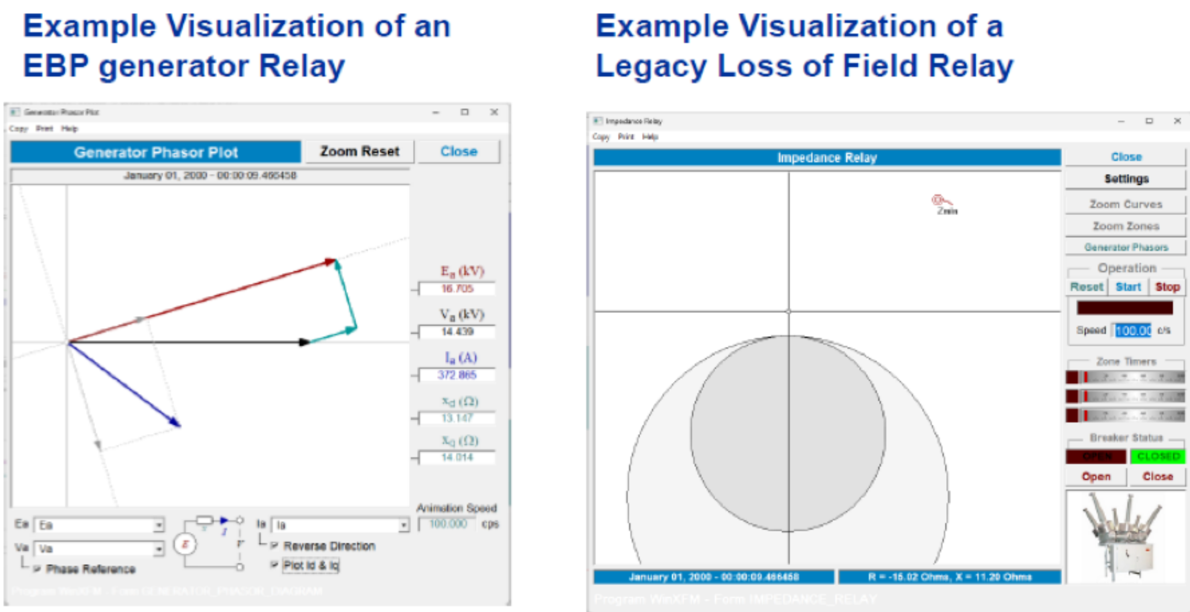

Figure 5.4: Operating Conditions During Time Period 1 – Right Figure: Legacy LOF Relay Response, Left figure: Estimation Based Protective Relay Visualization

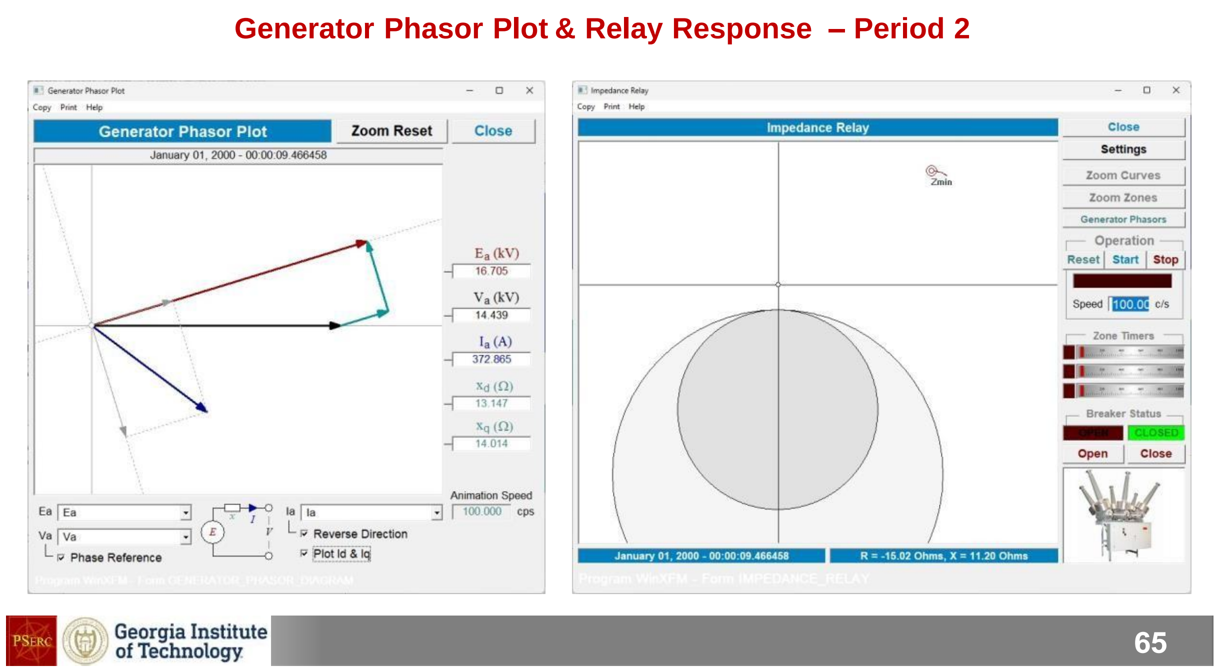

Figure 5.5: : Operating Conditions During Time Period 2 – Right Figure: Legacy LOF Relay Response, Left figure: Estimation Based Protective Relay Visualization

Generator Phasor Plot & Relay Response – Period 3

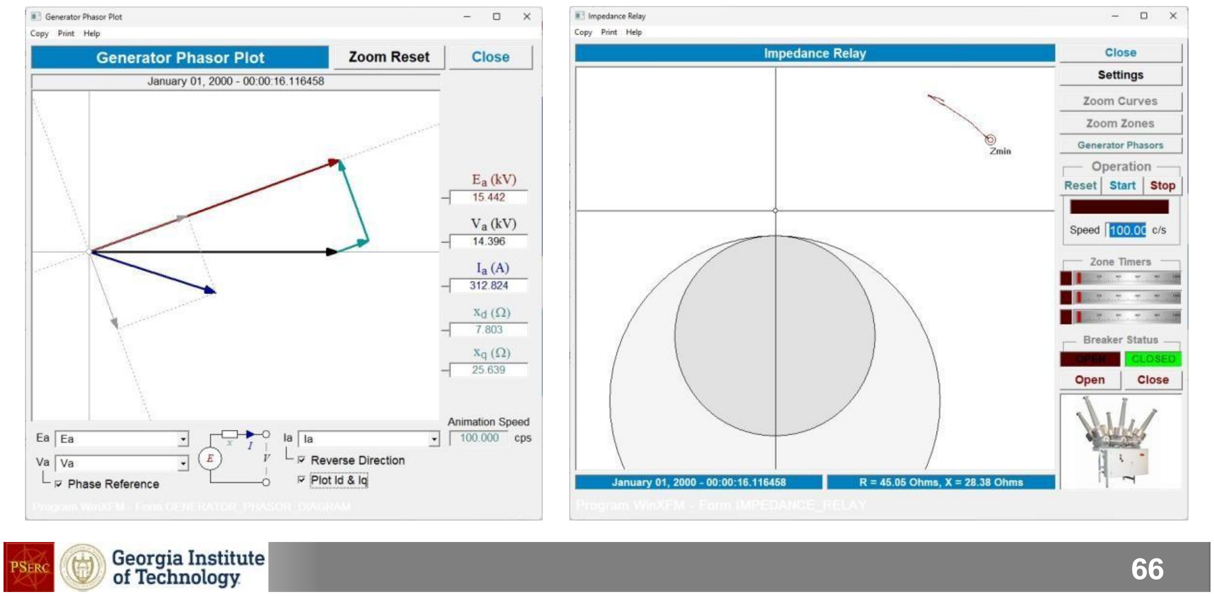

Figure 5.6: Operating Conditions During Time Period 3 – Right Figure: Legacy LOF Relay Response, Left figure: Estimation Based Protective Relay Visualization

Generator Phasor Plot & Relay Response – Period 4 – Breaker Opens

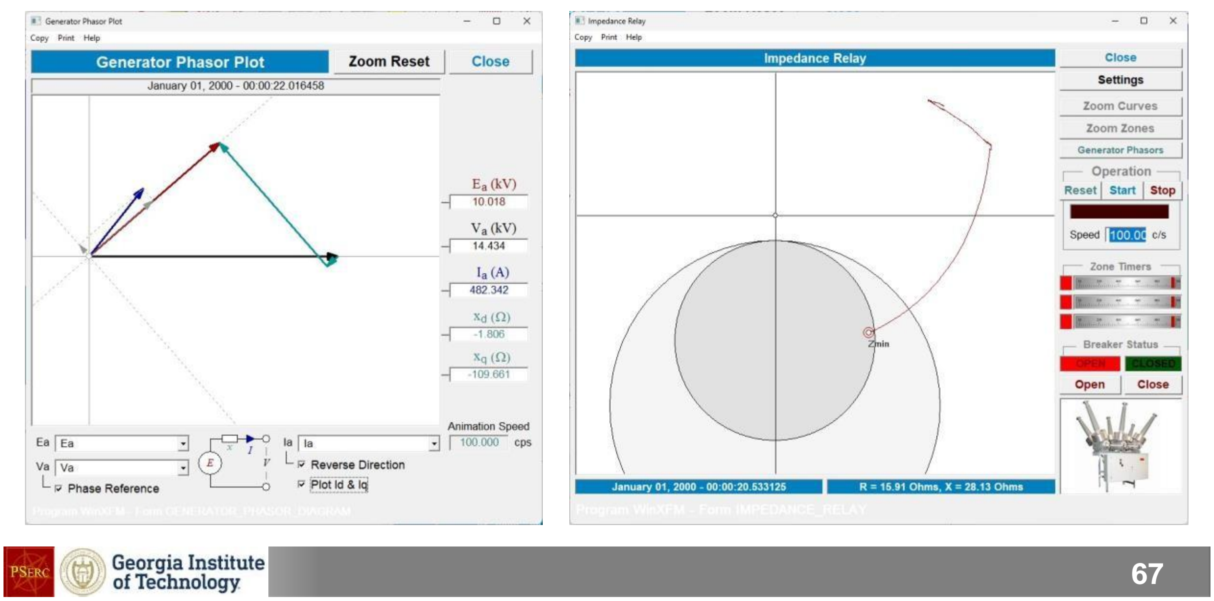

Figure 5.7: Operating Conditions During Time Period 4 – Right Figure: Legacy LOF Relay Response, Left figure: Estimation Based Protective Relay Visualization

During time period 4, the generator experiences a severe under-excitation. The generator current is leading the generator terminal voltage and the generated voltage is substantially lower than the generator terminal voltage. During this time period, the impedance seen by the LOF relay enters the smaller circle indicating generator tripping. In this case, this is a mis-operation.

The estimation based protective relay shows that the generator is fault-free, and no action is necessary. This is a case where the estimation-based protection is not affected from the transients of the system and all the different characteristics of the system with high level of inverter-based resources.

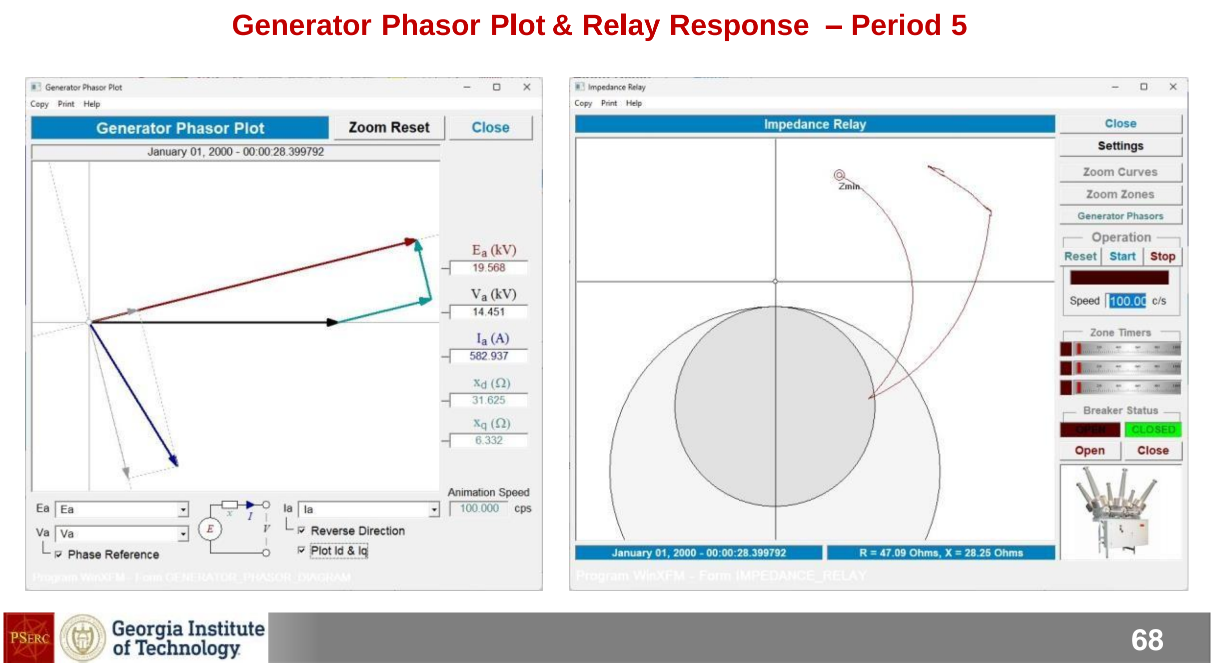

Figure 5.8: Operating Conditions During Time Period 5 – Right Figure: Legacy LOF Relay Response, Left figure: Estimation Based Protective Relay Visualization

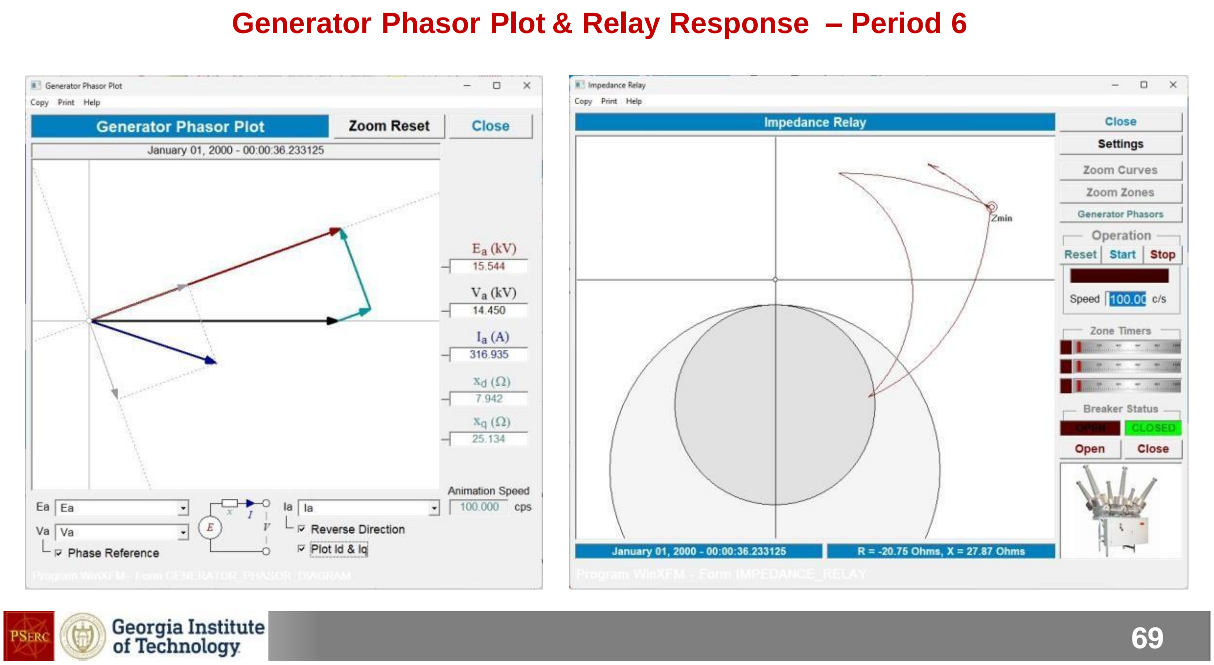

Figure 5.9: Operating Conditions During Time Period 6 – Right Figure: Legacy LOF Relay Response, Left figure: Estimation Based Protective Relay Visualization

The sequence of events has been captured in a visualization display to observe the operation of the generating unit and the operation of the legacy LOF relay as well as the estimation - based protection. The visualization display can be provided upon request.

6. Conclusions

This report aimed to understand the causes of overvoltages when Inverter-Based Resources (IBR) are suddenly disconnected from the grid. It explored how much an overvoltage is expected to occur and what are the implications on existing legacy protection schemes using real life test cases. Section one introduced the problem statement and some examples of real-life incidents that occurred in Germany and Greece due to overvoltages and why this work is important in deciding the positioning of new IBR projects in order to minimize the overvoltage on the grid.

Section two explored the proper way of representing an IBR to capture these phenomena. It justified the need to have proper reorientation along with previous work done in modeling IBRs. It emphasized the importance of having a well-established model that does not consume hardware resources and takes time in order to provide real-time data for field operation. This is critical when dealing with protection schemes that need to operate in few cycles. The report presented a mathematical model for developing a high-fidelity model that was used to represent the IBRs.

In section three, the report presented a real-life test system that is subject to the requirements presented first. A detailed test case system was provided including all the components starting from the generators, collector substation, and the distribution network which host the IBRs in a typical design of utility size PV Farms.

In section four, the report presented simulation results for selected events. It summarized the percentage of deviations of overvoltages for each of the three PV Farms. It also provided some remedial actions that can be utilized to reduce the overvoltage percentage which in turn can save the components from physical damage as well as reduce the probability of false tripping of legacy protection schemes.

In section five, the effects of temporary transients on the performance of a specific actual system are presented. The case study of the Greek island of Rhodes historical events was provided. The sequence of events were modeled and simulated using a high-fidelity model of the system. The simulation included detection schemes, enabled by the estimation-based protection, where unnecessary generator tripping was avoided when the IBR resources are suddenly disconnected.

References

[1] C. D. Vournas, Vassilis C. Nikolaidis, G. I. Tsourakis, “Coordinated Countermeasures against Overvoltage Instability in Autonomous Power Systems”, IEEE Trans. on PWRD-36, no.: 6, 2021.

[2] D. Reimert, Protective Relaying for Power Generation Systems. Boca Raton, FL: CRC Press, 2006.

[3] C. D. Vournas, Vassilis C. Nikolaidis, G. I. Tsourakis, “Coordinated Countermeasures against Overvoltage Instability in Autonomous Power Systems”, IEEE Trans. on PWRD-36, no.: 6, 2021.

[4] C. Vournas, N, Tagkoulis, “Investigation of Synchronous Generator Underexcited Operation in Isolated Systems”, International Conference on Electric Machines (ICEM), Alexandroupolis, Greece, Sept. 2018.

[5] Sakis Meliopoulos, George J. Cokkinides, Paul Myrda, Yu Liu, Rui Fan, Liangyi Sun, Renke Huang and Zhenyu Tan, “Dynamic State Estimation Based Protection: Status and Promise”, *IEEE Transactions on Power Delivery*, Vol. 32, No. 1, pp 320-328, February 2017.

[6] Evangelos Farantatos, Renke Huang, George J. Cokkinides, and A. P. Meliopoulos, ”A Predictive Generator Out- of-Step Protection and Transient Stability Monitoring Scheme Enabled by a Distributed Dynamic State Estimator”, *IEEE Transactions on Power Delivery*, Vol 31, Issue 4, pp 1826-1835, August 2016.

[7] Yu Liu, A. P. Meliopoulos, Rui Fan, Liangyi Sun, and Zhenyu Tan, “Dynamic State Estimation Based Protection on Series Compensated Transmission Lines”, *IEEE Transactions on Power Delivery*, Vol. 32, Issue: 5, pp 2199-2209, October 2017, DOI: 10.1109/TPWRD.2016.2633410.

[8] Yu Liu, A. P. Meliopoulos, Liangyi Sun, and Rui Fan, “Dynamic State Estimation Based Protection of Mutually Coupled Transmission Lines”, CSEE Journal of Power and Energy Systems, Vol. 2, Issue: 4, pp 6-14, December 2016, DOI: 10.17775/CSEEJPES.2016.00043.

[9] N. Hatziargyriou, J. V. Milanovic, C. Rahmann, V. Ajjarapu, C. Canizares, I. Erlich, D. Hill, I. Hiskens, I. Kamwa, B. Pal, P. Pourbeik, J. J. Sanchez-Gasca, A. M. Stankovic, T. Van Cutsem, V. Vittal, C. Vournas, “Definition and Classification of Power System Stability Revisited & Extended”, in press, IEEE Trans. on Power Systems, 2020.

[10] “Generic Positive Sequence Domain Model of Grid Forming Inverter Based Resource”, EPRI, https://www.epri.com/research/products/000000003002021403

[11] H. Satoh, K. Yamashita, K. Shirasaki and Y. Kitauchi, "Root-Mean Square Model of Three-Phase Photovoltaic Inverter for Unbalanced Fault," in *IEEE Open Access Journal of Power and Energy*, vol. 7, pp. 501-513, 2020, doi: 10.1109/OAJPE.2020.3025961

[12] WECC Wind Power Plant Dynamic Modeling Guide, WECC Renew. Energy Model. Task Force, Salt Lake City, UT, USA, Apr. 2014.

[13] WECCGuidelineCentralStationPhotovoltaicPowerPlantModelValida- tion Guideline, WECC Renew. Energy Model. Task Force, Salt Lake City, UT, USA, Mar. 2015.

[14] L. Qu, L. Zhu, L. Ge, and M. Sun, ‘‘Research on multi-time scale mod- elling of photovoltaic power plant,’’ in Proc. IET Renew. Power Gener., Oct. 2015, pp. 1–5.

[15] L.Qu,N.Chen,L.Ge,L.Zhao,S.Niu,andJ.Wang,‘‘Modelvalidationof PV power generation unit based on grid voltage disturbance test,’’ in Proc. IEEE PES Asia–Pacific Power Energy Eng. Conf., Oct. 2013, pp. 1–6.

[16] R. T. Elliott, A. Ellis, P. Pourbeik, J. J. Sanchez-Gasca, J. Senthil and J. Weber, "Generic photovoltaic system models for WECC - A status report," 2015 IEEE Power & Energy Society General Meeting, Denver, CO, USA, 2015, pp. 1-

[17] “NERC Reliability Guideline Template”, NERC, 2021, Report (nerc.com)